Science
AAAS

Supplementary Materials for

Engineering synthetic phosphorylation signaling networks in human cells

Xiaoyu Yang *et al*.

Corresponding authors: Nichole M. Daringer, daringer@rowan.edu; Caleb J. Bashor, caleb.bashor@rice.edu

Science **387**, 74 (2024)
DOI: 10.1126/science.adm8485

The PDF file includes:

Other Supplementary Material for this manuscript includes the following:

Materials and Methods

All plasmid constructs in this study are listed in **table S1** and their use in experiments is detailed in **table S2.** Constructs were generated using a custom hierarchical Golden Gate assembly cloning scheme (*51*) consisting of three layers (**fig. S1**). The first layer contains individual genetic parts; promoters, ORFs, and terminators that were PCR amplified from custom synthesized DNA fragments (IDT) to introduce BsaI cut sites or sourced as plasmids containing protein domains and cloned into a pUC19-derived 'Level 1' part vector (Ampicillin resistance) containing Esp3I sites (*52*). Promoters included CMV (*53*), EF1α (*54*), and RSV (*55*). The bGH225 terminator (*56*) was used in every construct. Transcriptional reporter constructs were built using parts from previous work (*10*) and are detailed in **table S3**. Part vectors were combined with a second pcDNA-based 'Level 2' destination vector (Kanamycin resistance) using Esp3I to generate expression unit vectors (promoter-ORF-terminator). Where indicated, up to 2 or 3 expression units were assembled into a 'Level 3' multi-gene vector (Amp resistance) via BbsI to enable multi-gene expression from a single plasmid (workflow illustrated in **fig. S1**). All PCR-amplified parts were sequence verified by Sanger sequencing (Genewiz) and plasmid assemblies were verified first by restriction digest and then nanopore sequencing (Oxford Nanopore Technologies).

Tissue culture and transfection

HEK 293T cells (ATCC® CRL-11268™) were cultured under humidity control at 37 °C with 5% CO_2 in media containing Dulbecco's modified Eagle medium with high glucose (Gibco, 12100061) supplemented with 10% Fetal Bovine Serum (FBS; GeminiBio, 900-108), 50 units/ml penicillin, 50 µg/ml streptomycin (Pen Strep; Gibco, 15070063), 2 mM L-Alanyl-L-Glutamine (Caisson labs, GLL02). ~$2x10^5$ cells at < 15 passage were plated in 24-well flat bottom tissue culture plates (GenClone, 25-108) in 0.5 mL of media. For flow cytometry experiments, after

growth for 24 h to 50–60% confluency, cells were transfected using polyethylenimine (PEI) (*57*). PEI stocks were made by dissolving linear polyethylenimine (Polysciences, 23966-2) at a concentration of 1mg/ml in milliQ H_2O, pH was adjusted to 7.0 with 1.0 N NaOH, and the solution was sterile filtered (0.22 μm) and stored at -20 °C until use. For time-lapse microscopy experiments, HEK293T cells were transfected with the appropriate plasmid set at 80% confluence in 24 well plates using jetPRIME (Polyplus, 101000046). We also showed that circuits transfected with jetPRIME showed similar quantitative behavior to those transfected with PEI (**fig. S5C**). Details of plasmid and reagent usage for all data panels in this study are listed in **table S2**. Unless otherwise indicated, all samples underwent co-transfection with pcDNA plasmid encoding BFP as a transfection control (see **table S1**). 4 h following the transfection the cell culture was replaced with 0.5 mL fresh complete DMEM medium. For circuit induction experiments involving ligand addition (**Figs. 3** and **4, figs. S20, S21, S23, S24, S25, S30**), 200 nM of the heterodimerizer AP21967 (Takara Bio USA, Inc., 635056) (*58*) or 20 ng/ml TNF-α (PeproTech, 300-01A) were added to culture media 12 h prior to flow cytometry analysis.

Human Umbilical Cord Mesenchymal Stem Cells (hUC-MSCs, gift from Olson lab, UTHealth Science Center at Houston) were cultured in αMEM (Sigma M4526-500mL) supplemented with 4.6% human platelet lysate (Sexton, PL-NH-100), 1% GlutaMax (Gibco, 3505-061), and 10 μg/mL gentamycin. Cells were plated for expansion at 1000-3000 cells/cm^2 in complete αMEM, incubating at 37°C and 5% CO_2 with humidity control, and changing media every 2-3 d. Cells were harvested at 80-90% confluency (~50,000 cells/cm^2) by aspirating media, washing with PBS, detaching with TrypLE™ Express (Gibco 12605-010) for 8 min at 37°C, then inactivating the TrypLE™ Express with an equal volume of complete αMEM. Cells were collected then centrifuged at 500xg for 8 min, resuspended in complete media, counted with a Countess II and corresponding cell counting slides (Invitrogen C10283), then frozen in complete αMEM with 5% DMSO (Fisher BioReagents BP231-100).

MSC nucleofection was performed on an Amaxa Nucleofector II with the 96-well Shuttle using the Lonza 96 well Nucleofector kit with P1 primary cell buffer (Lonza V4SP-1096). Cells were thawed and plated at a density of 10,000 cells per cm² and allowed to adhere overnight. Cells were then harvested and resuspended in 20 µL of P1 primary cell buffer containing appropriate plasmid sets. The cell-DNA mixture was transferred to nucleofection cuvettes, ensuring no air bubbles were introduced, and electroporated using the Amaxa Nucleofector II with FF104 program codes. After a 10-minute recovery period at 25°C, 100 µL of pre-warmed media was added to each cuvette. The cells were then incubated in 6-well plates at 50,000 cells per cm² to recover and expand for 48 hours before being harvested for flow cytometry analysis.

Human ARPE-19 cells (gift from Veiseh lab, Rice University) were cultured using HyClone DMEM (Cytiva, SH30023.01), with 10% FBS and 1% Pen Strep (Gibco, 15070063). To ensure optimal growth conditions, cells were passaged three times weekly to maintain a healthy confluence. For transient transfection experiments, cells were seeded in a 24-well plate at a density of $6x10^5$ cells per well 24 h prior to transfection. Cells were then transfected using jetPRIME (Polyplus, 101000046) or with a Neon NXT Electroporator (Thermo Fisher) according to the manufacturer's protocol, with cells receiving the designated plasmid set (**table S3**). For the Neon transfection, 8×10^5 cells were harvested by centrifugation at 300 g for 5 min, washed with DPBS and resuspended in 100 µL buffer R. 0.5 µg of plasmid DNA was added to the suspension and electroporation was performed using parameters 1350 V, 20 ms, 2 pulses, after which cells were grown in DMEM F12 medium. 6 h post-transfection, the culture medium was replaced with 0.5 mL of fresh complete DMEM/F-12 medium. Cells were detached using TrypLE™ Express 48 h following transfection for flow cytometry analysis.

Flow cytometry

36 h after transfection, cells were prepared for fluorescent antibody staining and flow cytometry analysis according to the methods of Krutzic and Nolan (*59*), with modifications. To

prepare cells for analysis, media was aspirated, and cells were washed once with PBS, then detached with TrypLE™ Express. Samples with between 1.5 and 2 x 10^6 cells/ml were collected for each well, and cells were then washed once with sample buffer (1x PBS, 1% BSA) and fixed with 1.6% paraformaldehyde (Alfa Aesar, 43368-9M). After incubation at room temperature for 12 mins in the dark, cells were washed once with sample buffer and then permeabilized with 90% ice-cold methanol for 40 mins at 4 °C in the dark. Cells were then blocked with human IgG (Sigma, I4506-50MG) for 30 mins. The following fluorophore-labeled monoclonal antibodies were used throughout the study: APC-labeled α-FLAG: (clone# REA216, Miltenyi Biotech, 130-119-683), Alexa Fluor 750-labeled α-MYC tag (clone# 90000000000, R&D Systems™, IC3696S100UG), Alexa Fluor 594-labeled α-HA tag (clone# 16B12, Invitrogen, A-21288), PE-labeled α-CD247 (pY142) (clone# K25-407.69, BD, 558448) for staining the phosphorylated form of the synSub harboring a $CD3Z_{131-164}$ pY motif (see below and **fig. S4**), Alexa Fluor 488-labeled α-SLP76 (pY128) (Clone# J141-668.36.58, BD, 558439) for staining the phosphorylated form of synSub harboring a $SLP76_{108-154}$ (see below and **fig. S4**), and Alexa Fluor 680-labeled α-V5 tag (clone# E10/V4RR, Invitrogen, MA5-15253-D680). Cells were incubated with experiment-specific antibody panels at 4°C for 45 mins in the dark and then analyzed using an SA3800 spectral cell analyzer (Sony Biotechnology). Typically, ~1.5 x 10^5 total events were collected per sample. Spectral unmixing was performed for all datasets using built-in software. To facilitate unmixing, single-color controls were run in parallel to each experiment by transfecting individual plasmids that expresses fluorescent proteins, epitope tagged proteins, or a kinase-fused substrate that provides high phosphorylation signal for pY-antibody tagging. Antibodies panels, fluorescent proteins, and color channels measured in experiments performed in this study are listed in **table S4**.

Western blot

36 h after transfection, cells were prepared for western blotting by aspirating media, washing cells twice with ice-cold PBS, and resuspended in 100 µL RIPA lysis buffer (Thermo Fisher, 89900) supplemented with Halt™ Protease and Phosphatase Inhibitor Cocktail (Thermo Fisher, 89900) and phosphatase inhibitor (Thermo Fisher, 78440) on ice for 30 min. Lysate was cleared by centrifugation at 4 °C, mixed with SDS-PAGE sample buffer (Bio-Rad, 1610747) supplemented with 10% b-mercaptoethanol, and run on 4–20% Mini-PROTEAN® TGX™ precast gels (Bio-Rad, 4561094) at 120V. Cellular phosphotyrosine was detected using mouse α-pY (Cell Signaling Technology, 96215); synSub was detected using Mouse α-Myc mAb (Invitrogen, MA1-21316); phosphorylated synSub was detected by Mouse α-pY-CD247 mAb primary (BD, K25-407.69). synKin was detected using Mouse α-Flag mAb (Sigma Aldrich, F1804). StarBright Blue 700 goat a-mouse was used as the 2° antibody, (Bio-Rad, 12004159). For tubulin loading controls, rhodamine direct-conjugated mouse a-Tubulin (Bio-Rad, 12004166) was used. Western blot fluorescence was visualized using a Chemidoc MP (BioRad), and Matlab was used to quantitate regions of interest intensities.

Cell viability

For cell viability and density measurements in phosphorylation circuit-containing cells (**fig. S7D**), 15 wells were transfected with each of the circuit compositions, then three wells were harvested for each composition at 12, 24, 36, 48, and 72 h following transfection. Cell count and viability were measured using the Countess II Cell Counter (Invitrogen) using 0.4% Trypan Blue staining (Invitrogen, C10283).

Flow cytometry data analysis

Unmixed flow cytometry data were analyzed and plotted using a combination of FlowJo (BD) and custom Python scripts using the Matplotlib library (https://ieeexplore.ieee.org/document/4160265) according to the approach illustrated in **fig. S5A**

(see fig_plot.py for scripts and code description in **table S5**). Data were initially processed in FlowJo, gating events for cell size and complexity (SSC-A vs. FFC-A) followed by gating for single cells (FSC-H vs. FSC-A) (**fig. S5A,** first and second panel). Events were further analyzed for positive transfectants by gating $\mu + 2\sigma$ of the BFP expression distribution (15-20% of the total population, **fig. S5A,** third panel). These gates were identically applied to all experimental datasets to ensure acquisition of similar cell counts throughout the paper ($1.2x10^4 \pm 240$ for BFP gated cells**)**. BFP-gated events were replotted in FlowJo to generate 2D scatter plots with protein expression levels plotted on the x and y axes (e.g., kinase vs. substrate), (**fig. S5A,** fourth panel), and events with negative values in any fluorescent channel were omitted (6.7% ± 0.53 of BFP gated cells across all datasets). Hexagonal hit (HH) maps (**fig. S5A,** fifth panel) were plotted using the hexbin function from Matplotlib to hexagonally bin the 2D scatters (100 bins per plot). Hexagons were plotted as size-proportional to the log normalized event count in each bin, and bins with less than 5% of the maximum events (typically <50 events) were not plotted. Using this approach, each bin contains a maximum of 901 ± 57 events, accounting for 7.5% ± 0.47 of the total events, bins with >80% of the maximum event count were plotted as hexagons with a maximum size, which contain ~4712 ± 423 events among all experiments. To create hexagonal hit and heat (HHH) maps (**fig. S5A,** sixth panel), mean fluorescence from phospho-specific antibodies (**Figs. 1-3**, **4A**, **4B**) or EGFP (**Fig. 4A**, right) was calculated for each bin and plotted as a colormap, in each panel, the maximum fluorophore intensity within the bins was chosen as the upper limit for the colormap, while the minimum value was chosen as the lower limit. For histogram plots (**figs. S5, S6, S7, S9, S15, S16, S17, S20, S23, S24, S25 and S30**), BFP-gated cells with negative fluorescence intensities were omitted, and fluorescence distribution from the α-CD3Z phospho-specific antibody for the remaining BFP-gated cells was plotted. To ensure our ability to quantitatively compare part and circuit behavior across different experiments, we used the same unmixing controls for each of the antibody-conjugated fluorophores across all the experiments. To check the spillovers between different channels in multi-color flow cytometry, we

ran each of the single-color controls with all the lasers on, and after unmixing, we verified that there was minimal fluorescence spillover between channels for all ab-conjugated fluorophores (**fig. S5B**).

Modelling

Non-equilibrium thermodynamic modeling, fitting, and data plotting functions for the single (**Fig. 1, figs. S12, S13** and **S14**) and two-step (**Fig. 2, figs. S18** and **S19**) phosphorylation circuits were implemented using custom Python code. The functions were then used in python notebook files to generate parameters, fitting, and prediction results. All .py and .ipynb files used in each experiment are listed in **table S5** and their uses are described below. For dynamic modeling of phospho-sensor and closed-loop therapeutic circuits (**figs. S22**, **S27**, **S28**) we used a custom MATLAB file, dynamic_model.m that incorporates all the equations, parameter fitting, and visualization tools. Utilization of dynamic_model.m is listed in **table S5**. Dose response curve fitting (**Fig. 3B, figs. S24B** and **S25B**) was performed using a custom MATLAB file dose_curve.m. Use of dose_curve.m is listed in **table S5**.

Imaging and time-lapse microscopy

For time-lapse imaging of ligand-inducible synSub-condensate colocalization, 12 h after cells were transfected using jetPRIME (see above), they were replated on 8-well chamber slides (Ibidi, 80806) coated with 10 µg/ml human fibronectin (Sigma, FC010) at 60,000 cells•well^{-1}. For each experiment, 2 wells were used for no ligand control, and 2 for sequential ligand induction and inhibition. Experiments were initiated 24 h after replating by adding AP21967 to the corresponding wells to a final concentration of 200 nM and images were taken every 10 min for 1.5 h. For experiments involving the use of the inhibitor imatinib mesylate (LC Laboratories, I-5508), a concentrated DMSO stock solution was diluted in media (~1:1000) in wells 1.5 h after AP21967 addition to reach a final concentration of 10 µM. The cells were imaged with a Nikon

A1-Rsi confocal system mounted on a wide-field Ti-E fluorescence microscope. Imaging was performed using a 60x oil-immersion objective (numerical aperture, 1.27; working distance, 0.17 mm). Green fluorophores (EGFP) were excited with a 488 nm photodiode laser. The red fluorophores (mCherry) were excited with a 561 nm photodiode laser. The microscope was equipped with an environmental chamber to ensure cells are maintained at 37 °C and 5% CO_2 during imaging. The images were collected using a Galvano scanner operating at 0.94 fps.

Image analysis

Analysis of timelapse microscopy data was performed using a custom image processing pipeline. Cells analyzed in the time course were chosen that: **i**) expressed detectable levels of EGFP-tagged synSub; **ii**) contained visible PopZ (mCherry) condensates (>2x2 pixels) prior to AP21967 addition; and **iii**) remained visible in the imaging field of view for the duration of the time course. These criteria yielded ~10 cells per experiment, which accounted for ~10-20% of all cells in the initial field of view. For images taken at each time point, cytoplasmic regions of the cells were segmented based on EGFP fluorescence using the pixel classification function from Ilastik (*60*) trained on manually drawn masks (**fig. S21A**). Quantification of EGFP/mCherry condensate colocalization was performed using custom MATLAB code (condensate_analysis.m, code description in **table S6**). For images at each time point, mCherry and EGFP pixel intensity distributions within the single-cell masks were fitted to a normal distribution to quantify mean pixel intensity within the cytosol. We then set an intensity threshold of 99 quantiles for both color distributions ($T_{mCherry}$ and T_{EGFP}). Red pixels with intensities $>T_{mCherry}$ were designated as part of the condensates. To measure synSub colocalization with the condensates, we quantified EGFP pixel intensities that were within the mCherry condensate pixels and were also $>T_{EGFP}$. Mean EGFP cytoplasmic intensity was calculated using non-condensate colocalized pixels within the cell mask. The ratio of colocalized:total EGFP was calculated by dividing the pixel intensity sum for colocalized EGFP by that of cytoplasmic EGFP, similar to Zhang et al (*61*). To create histogram

plots in **Fig. 3C**, a single representative cell was chosen, and an 80-pixel line was drawn from the outside of the cell, through the cytoplasm, and through preformed mCherry condensates for each of the indicated time points. mCherry and EGFP intensities along the line were plotted and normalized to the maximum pixel intensity within the accompanying cytoplasmic mask. The normalized intensities for mCherry and EGFP were then plotted on the same plot (see intensity_along_line.m for script, code description in **table S6**).

Transwell immunosuppression experiments

Fresh peripheral blood mononuclear cells (PBMCs) were obtained from a healthy anonymous donor via the Gulf Coast Blood Center. To isolate PBMCs from whole blood, SepMate™ PBMC isolation tubes (StemCell, 85450) and Ficoll-Paque PLUS medium (Cytiva, 17144002) were utilized per the manufacturer's instructions. Following isolation, PBMCs were cultured in RPMI-1640 medium (Sigma-Aldrich, R4130-10L), supplemented with 10% FBS, 50 units/ml penicillin, 50 µg/ml streptomycin, and 2 mM L-Alanyl-L-Glutamine. On day 0, 1 million PBMCs were plated in 1 mL RPMI medium per well of 24-well flat-bottom tissue culture plates and stimulated using Dynabeads™ Human T-Activator CD3/CD28 (Gibco, 11131D) at a 2:1 cell:bead ratio.

For transwell co-culture assays, HEK293T cells were transfected with circuit-encoding plasmids using jetPRIME 1 d before PBMC activation (day -1). 12h following PBMC activation, HEK cells were lifted using TrypLE and resuspended in 500 µL of RPMI medium from the PBMC culture. The HEK cells were then placed in the 1.0 µm transwell insert (CORNING, 354569), while PBMCs remained at the bottom of the well. Supernatant was collected at 12h intervals from the co-culture's start and continued for a total of 60 hours. 60 hours following the coculture, PBMC proliferation was assayed using iClick™ EdU Andy Fluor™ 488 Flow Cytometry Assay Kit (ABP Biosciences, A007) according to the manufacturer’s protocol with the following modifications. Briefly, 2 µM EdU (5-ethynyl-2´-deoxyuridine) was added to the culture media for 30 mins, then

cells were harvested, transferred to a 96 well plate, washed with 200 µL PBS with 1% BSA, and fixed with 100 µL iClick fixative, washed, then permeabilized by using 100 µL 1X iClick permeabilization and wash reagent. EdU detection using an Andy Fluor 488 azide was accomplished by click chemistry using a reaction scaled down to 40% of the manufacturer's protocol, adding 200 µL Click-iT reaction cocktail to cells resuspended in 40 uL 1x iClick permeabilization and wash buffer. To analyze the proliferation rate for different subsets of T cells, PBMCs were surface-labeled with fluorophore-conjugated α-CD4, α-CD8, and α-CD3 monoclonal antibodies (BUV737 Mouse α-Human CD3; clone# UCHT-1, BD, 612750. PE α-human CD4; clone# RPA-T4, Biolegend, 300539. APC α-human CD8; clone# SK1, Biolegend, 344722). Unmixed flow data were imported into FlowJo to analyze the proliferation rate under different T cell subgroups. Supernatant collected during the co-culture was further analyzed by ELISA to determine TNF-α and IL-10 secretion dynamics and endpoint IFN-γ levels (ELISA MAX™ Deluxe Set Human TNF-α; Biolegend, 430204, ELISA MAX™ Deluxe Set Human IL-10; Biolegend, 430604, ELISA MAX™ Deluxe Set Human IFN-γ; Biolegend, 430104).

Computational prediction of immunogenicity

Immunogenicity analysis was performed using the T Cell Class I pMHC Immunogenicity Tool, an open-source tool from the Immune Epitope Database used to predict the relative chance a peptide/MHC complex will elicit an immune response (*62*). Sequences were processed using IEDB-recommended default settings. Sequences of synthetic receptors, proteases and three monoclonal antibodies DNA-binding domains for commonly-used regulators were obtained from the literature.

Supplementary Text

Goal: Develop a scalable framework for engineering synthetic signaling networks

In this study our overall objective was to develop a synthetic biology framework for engineering artificial phospho-signaling pathways in mammalian cells using natural design principles as inspiration. In native eukaryotic settings, signaling networks play a central role in cellular decision making, development, growth, and migration (*1, 24, 63*). Pathways such as Ras-Erk (*64*), Wnt/β-Catenin (*65*), and TGF-β (*66*) regulate homeostatic functions (e.g., proliferation, differentiation, and cell fate determination), and their disruption can lead to tumorigenesis and metastasis (*67*). Because of their important role in health and disease, signaling pathways have been the object of intensive experimental work for decades, and significant progress has been made in identifying and characterizing interactions between their constituent molecular components, including cell surface receptors that act as network inputs (*68, 69*), freely diffusing cytoplasmic singling proteins that act as network wiring (*70, 71*), and downstream transcription factors that regulate gene expression in response to signal propagation (*72, 73*).

An important organizational principle that has emerged over the last several decades is that signaling networks are composed of sets of futile cycles (*23, 24, 39*) in which the reciprocal "writing" and "erasing" of phosphorylation "marks" on a substrate protein are respectively catalyzed by enzymes with kinase and phosphatase activities. Signal propagation occurs when the ratio of these opposing activities is altered by an upstream input (e.g., ligand binding to a receptor). The substrate protein and the kinase/phosphatase pair that act on it comprise phosphorylation cycle—a motif that can be considered as the fundamental unit of phosphorylation-based signaling networks (**Fig. 1A**) (*23*). A signaling pathway may feature multiple phosphorylation cycles connected in series (a cascade) (*74*). Generally speaking, the quantitative properties of circuit components—their intracellular concentrations, activities, and interaction affinities—confer phosphorylation networks with their signal processing capabilities (*39*).

Another breakthrough in the understanding of signaling network organization came with the discovery that signaling proteins are composed of interconnected sets of discreetly folding domains (*75*). While many catalytic domains "write" and "erase" phosphorylation marks, the majority mediate protein-protein interactions with other signaling components, forming the wiring that links networks together (*37*). One important class of interaction domains that was identified that specifically binds to PTM-modified substrates and thus act as "readers" to decode the PTM state of a substrate (*76*). Two of the best-known examples of such PTM-binding domains are the Src homology 2 (SH2) (*38*) domain and pY-binding (PTB) domains (*77*), both of which are specifically recruited to motifs containing pY (*78*). The prevalence of these domains in signaling pathways suggests a design logic for signaling network connectivity whereby PTM-dependent binding interactions couple phosphorylation cycle equilibrium to downstream targets (*79*).

As described in the sections below, we used these two natural design principles—phosphorylation cycle network composition and modular domain encoded function—as guides for developing a framework for our synthetic signaling circuits. By analogy to natural systems, we engineered synthetic phosphorylation cycles as the elementary building block in our framework. We also describe developing a collection of protein domain parts—kinases, phosphatases, substrates and obligate and phosphorylation-dependent interaction domains—to support synthetic cycle construction, tuning, and interconnection into networks. We use this set of parts to compose synthetic kinases, phosphatase, and substrates, which we respectively refer to as synKin, synPhos, and synSub. Each of these components comprises a catalytic activity or substrate domain module that is involved in signal transmission, as well as an interaction module that directs its specificity.

Identification and validation of protein domain parts

Interaction domains have been demonstrated to be essential for intracellular targeting to substrates for many pY kinases (*80*). In *in vitro* activity assays, pY kinases generally demonstrate

lower specific activity toward peptide substrates compared with pS/pT kinases (**fig. S2A**) (*81-89*). Together, these observations suggest that catalytic specificity between pY kinases or phosphatases and their substrates is determined to a great extent by interaction domain-mediated co-localization rather than active site steric recognition of the phosphorylated amino acid sequence (*90, 91*). Non-receptor Y kinases and Y phosphatases expressed in human immune cells offer excellent examples of both domain-mediated functional modularity (*92*) and recruitment-based specificity. For example, T cell receptor (TCR) signaling activation consists of a series of co-localization events that include initial phosphorylation of the TCR chains by LCK, followed by phosphorylation of adjacent downstream pathway members (e.g., SLP76) via SH2-mediated recruitment of ZAP70 to Y-phosphorylated ITAMs (immune tyrosine activation motifs) located within the TCR complex (*93*) (**fig. S2B**).

Because our design goal was to develop a part set that enabled phosphorylation specificity to be programmed through interaction domain-mediated recruitment, we elected to use immune pY signaling pathways as a source of protein domain parts for constructing synthetic signaling pathways. This is not only because of their strong dependence on recruitment and co-localization, but because their components are predominantly expressed in immune cell linages (e.g., T cells and B cells) and therefore are less likely to exhibit crosstalk in non-immune cells or cell lines (*94*) (e.g., HEK293T). We hypothesized that the activity of pY kinase and phosphatase domains drawn from these pathways could be abstracted from their native context and artificially directed to phosphorylate and dephosphorylate engineered substrate proteins by appending nonnative protein-protein interaction domains (**fig. S2C**). To test this hypothesis, we chose five pY kinases (**fig. S3**): ZAP70 and Syk, which are respectively involved in activation of TCR and B cell receptor signaling (*95, 96*), and Src family members Lyn and Lck, which serve as upstream regulators of TCR and B cell receptor signaling (*30*). Finally, we tested ABL kinase, another Src kinase family member that is well-characterized, but not immune-specific (*97*).

Our domain part validation approach involved testing different length truncations for each kinase to identify optimal domain boundaries and assess the functional importance of nearby 2° protein structure elements (**fig. S3**). For substrate sequences, we selected motifs that the kinases natively phosphorylate, ITAMs (immune tyrosine activation motifs) and ITIMs (immune tyrosine inhibition motifs), which are found primarily on cytoplasmic receptor domains that are expressed in human immune cells (**fig. S2B**) (*32, 98*). Most ITAMs and ITIMs are processively phosphorylated at two adjacent Ys (typically 11 residues apart) that recruit members of a specialized family of tandem SH2 (tSH2) domains that simultaneously bind both pY motifs with affinities of between 0.5 - 50 nM (*99*). To mediate orthogonal recruitment between kinase truncations and the substrate motif, both species were appended to leucine zippers (LZs), which are short domains that form heterospecific coiled-coil interactions between cognate binding partners (*31*). The amino acid sequences for a representative set of these engineered proteins, —a synKin and a synSub—are shown in **fig. S4**. In this example a kinase domain variant derived from ZAP70 is appended to an acidic LZ (LZ-E) and a substrate sequence from the ITAM3 motif of CD3Z (residues 131-164) is appended to a basic LZ (LZ-R), with flexible GS linkers placed between the LZ and the domain or motif. The ITAMs depicted in **fig. S4** were chosen for many of the experiments in this study due to the availability of antibodies against their phosphorylated forms (see **Materials and Methods**). A glutathione S-transferase (GST) is appended to the substrate to stabilize its intracellular expression. Additionally, the synKin has a FLAG epitope tag fused to its N terminus, while the synSub has a 3x MYC tag (**fig. S4**).

We used transient co-expression of the synKin/synSub pair in HEK293T cells to screen for optimized kinase domain part function using phospho-flow cytometry (see **Materials and Methods**) (**fig. S6A**). We tested both WT and truncated versions of the kinases shown in **fig. S3**, measuring component expression using α-FLAG and α-MYC antibodies, as well as phosphorylation of the synSub $CD3Z_{131\text{-}164}$ motif (**fig. S6A**) (see **Materials and Methods**). Flow cytometry histograms and mean values for empty cells and cells expressing synSub alone are

shown in **fig. S6B**. Kinase domain truncations were tested against a synSub version with a non-cognate LZ, as well as a non-phosphorylatable version (Y to F mutation). This allowed our screen to identify truncation variants that met the following criteria: **i)** they maximized phosphorylation of recruited (cognate LZ) synSub; **ii)** they minimized phosphorylation of the unrecruited (non-cognate LZ) synSub; **iii)** they demonstrated low non-specific background phosphorylation signal as a result of their expression; and **iv)** they showed a strong, monotonic expression profile (α-FLAG stain) (**fig. S6C**). Our results revealed that while several of the kinase variants show strong phosphorylation, many also show recruitment-independent phosphorylation or weak/non-monotonic expression profiles. We selected $ZAP70_{326-619}$ as our domain part for further synKin engineering due to its ability to balance the above criteria. Based on our results from Lyn and Lck truncation experiments, we elected to use a corresponding truncation of ABL kinase (228-540) for subsequent engineering.

To further optimize synKin, we mutated several Y residues (Y492 and Y493 in ZAP70, Y226 and Y393 in ABL) that are known to regulate kinase activity. Mutating Y492 has been shown to enhance ZAP70 catalytic activity, whereas mutation of Y493 to F abolishes activation of WT ZAP70 by Lck (*100, 101*), while mutating ABL Y226 and Y393 to F abolishes autophosphorylation and activation by Src, but does not alter catalytic activity (*102*). By mutating these residues in our synKin, we hoped to avoid the possibility of them being phosphorylated by other kinases in our circuits, by native signaling pathways, or through autophosphorylation, resulting in unpredictable or variable activity (**fig. S6D**). We found that F to E mutations had marginal effects on synKin activity but variable effects on expression, while mutating to F had little effect on expression but enhanced synKin activity. Double Y-to-F mutations in both $ZAP70_{326-619}$ (Y492F, Y493F) and $ABL_{228-540}$ (Y226F, Y393F) demonstrated the highest phosphorylation activity.

We next validated that our synKins and synSubs function in recruitment- and kinase activity-dependent fashion (**Fig. 1B** and **fig. S7A**) by comparing their ability to phosphorylate synSub against several negative controls: a synKin with a non-cognate LZ, one harboring a kinase-dead

mutation (K369R in ZAP70, K271R in ABL) (*103, 104*), and a non-phosphorylatable (Y to F) synSub. We used this approach to test both synKins against the $CD3Z_{131-164}$ synSub, as well as one harboring phosphorylation sites from $SLP76_{108-154}$ (see **fig. S4**), which is a native substrate for ZAP70 (*86*). We found that the ZAP70-derived synKin showed recruitment- and kinase-dependent activity toward both synSubs, while the ABL-derived synKin was only able to phosphorylate the CD3Z synSub (**Fig. 1B** and **fig. S7A**). This active site-level specificity is likely due to the presence of multiple negatively-charged residues in SLP76 that facilitate its recognition by ZAP70 (*105*), with ABL showing higher preference for neutral AAs, particularly at positions -1 and +3 relative to the phosphorylated Y (*106*).

We conducted several tests to further assess phosphorylation specificity of our synthetic components and their potential for host cell crosstalk. We first performed western blots **(fig. S7B)**, probing lysates generated from synKin/synSub groups shown in **Fig. 1B,** along with a synKin-only composition. Here, our goal was threefold: 1) to assess the degree of background pY phosphorylation by synKin when expressed in HEK293T cells; 2) determine if endogenous HEK293T Y kinases have any activity for synKin; 3) demonstrate that the synKin pY signal detected by antibodies is primarily due to synSubs phosphorylation. Using a general α-pY antibody, we probed HEK293T lysates and quantified levels of pY phosphorylation (**fig. S7B, upper left)** in each lane. While we found small differences in pY phosphorylation patterns between samples with and without active synKin, overall phosphorylation levels were comparable between each sample. When we probed the same lysates with α-Myc and α-Flag, we observed discreet bands corresponding to approximate MWs for synKin and synSub (~44 and ~43 kDa) (**fig. S7B, bottom left and right)**. Probing with α-CD247-pY142 antibody showed a band at ~50 kDa corresponding to phosphorylated synSub that was dependent upon co-expression with active synKin (**fig. S7B, upper right)**, and showed 8.4x difference between samples containing recruited and unrecruited synKin, similar to what was observed in the HHH plots in **Figure 1B** (10.2x). There were no significant differences in phosphorylation detected by the α-CD247-pY142

antibody at higher or lower molecular weights than the ~50 kDa band, suggesting that any changes in signal observed upon addition of synKin are exclusively the result of synSub phosphorylation. We next conducted experiments using several Y kinase inhibitors to determine if synSub is subject to significant phosphorylation by endogenous Y kinases (**fig. S7C**). We selected well-characterized inhibitors that target highly expressed protein kinases, including dasatinib for the Src family kinases, lapatinib for EGFR family RTKs, and imatinib mesylate which targets Bcl/ABL and was used to inhibit our phospho-sensor circuit in **fig. S22**. As also observed in **fig. 6B**, we found that the level of apparent synSub phosphorylation detected by staining cells expressing only synSub with α-CD247-pY142 was similar to that of empty cells. Addition of the inhibitors showed little effect on phosphorylation signal as measured by phospho-flow. Interestingly, when we added the general phosphatase inhibitor Na_3VO_4, we saw a modest rise in synSub phosphorylation that was still much lower than that the signal induced by either recruited or unrecruited synKin. Finally, we demonstrated that expression of the $ZAP70_{326\text{-}619\ FF}$/$CD3Z_{131\text{-}164}$ synKin/synSub pair does not impair cell viability or cell growth by comparing proliferation and density over a 72 h time course with blank cells or cells only transfected with synSub (**fig. S7D**). Taken together, these results offer evidence of minor interactions between our circuits and the host cell machinery. While we observed a small degree of off-target pY phosphorylation, it was apparently non-toxic based on our growth/viability results. Further, while we observed little evidence for synSubs being phosphorylated by background kinase activities, our Na_3VO_4 result argues that there may be weak background kinase activity acting on synSub that is overridden by background Y phosphatase activity, thereby maintaining synSub in an unphosphorylated state under basal conditions.

After functionally validating the protein domain parts comprising the $ZAP70_{326\text{-}619\ FF}$/$CD3Z_{131\text{-}164}$ synKin/synSub pair, we attempted to tune phosphorylation levels by substituting parts with different biophysical properties (**Fig. 1C**). The binding interaction between synKin and synSub was tuned by mutating a residue in LZ-E from L to S or E (*31*). The catalytic activity of the synKin

was adjusted by mutating the conservative HRD motif of the kinase catalytic pocket into HKD and HSD, each of which has diminished phosphorylation rates (*33*). SynKin expression level was tuned by inserting Kozak sequence variants into the expression construct, resulting in differential rates of protein translation (*34*).

To engineer a complete phosphorylation cycle, we explored the use of phosphatase domains from three well-studied Y phosphatases as the basis for synPhos engineering: PTPN1 and PTPN3, which are broadly involved in Y signaling that regulates processes ranging from metabolism to cell proliferation (*107, 108*), while PTPN6 (SHP1), plays key roles in T and B cell signaling (*109*). We tested a truncation series for each phosphatase in a similar manner to the kinases, according to their predicted secondary structures (**fig. S8**). The AA sequence for a representative synPhos is shown in **fig. S9A** and features residues 1-319 from PTPN1 appended to LZ-E and a 3x HA epitope tag. Phosphatase truncation variants were tested using the $ZAP70_{326\text{-}619\ FF}$/$CD3Z_{131\text{-}164}$ pair shown in **Fig. 1B**. $PTPN1_{1\text{-}319}$ was chosen as the default synPhos due to its high, monotonic expression profile and apparent dephosphorylation of the $CD3Z_{131\text{-}164}$ synSub (**fig. S9B**). The default synPhos was further validated in **Fig. 1D**, where it was demonstrated that only recruited, catalytically active phosphatase was able to dephosphorylate synSub, while a synPhos without a cognate LZ, or a catalytically dead synPhos allele (D181A, R221M) (*110*) was unable to dephosphorylate synSub.

Quantitative modeling: background and motivation

Our ability to build, measure, and tune synthetic phosphorylation cycles motivated us to develop a modeling framework that could directly relate theory to our engineering framework. Historically, a great deal of work has gone into developing chemical kinetic models that describe activity of kinases and phosphatases using concepts from control theory (e.g., feedback, amplification, adaptation) and in this way, relate the form and function in networks constructed from phosphorylation cycles (*24*). However, these models seldom account for the modular nature

of signaling proteins and the distinct roles that catalytic and interaction domains play in specifying network behavior. To model phosphorylation cycles constructed with our toolkit, we established a new “nonequilibrium thermodynamics” approach that emphasizes the central role played by PPIDs and the biophysics of binding. Our approach reformulates nonequilibrium steady-state behavior of cycles using generalized thermodynamic models, combining classical partition functions to describe protein-protein interaction equilibrium with steady-state kinetic equations to encode kinase and phosphatase activity. As such, the model directly relates our domain parts to their functional properties. In this study, we used this modelling framework as a tool to predict phosphorylation circuit behavior, and also to validate the modularity of our parts and design scheme. We first fit training data corresponding to a limited phosphorylation circuit design space to extract parameters for the behavior of individual parts, and then use the parameterized model to predict phosphorylation across design space for different circuit compositions.

Model description

In this section, we describe a family of increasingly sophisticated models used to quantitatively model synthetic phosphorylation cycle behavior: **(i)** a simple circuit composed of a kinase-substrate pair (**Fig. 1B**) **(ii)** a complete cycle (**Fig. 1D**), and **(iii)** a circuit composed of two interconnected cycles (**Fig. 2A**).

synKin-synSub phosphorylation. We begin by writing a mathematical model for the synKin/synSub pair shown in **Fig. 1B**. The components are the synKin which, for clarity, we denote with a W (for “writer”), and the synSub is denoted by S (for “substrate”) which can exist in two forms: unphosphorylated S^u and phosphorylated S^p. In our model, the synKin binds to the synSub at a rate set by the kinetic parameter k_{WS}^{+} and unbinds at a rate governed by the kinetic parameter k_{WS}^{-}, an equilibrium process that occurs independently of synSub phosphorylation

state. The ratio of these parameters defines the equilibrium disassociation constant K_{WS} and can be related to the binding energy $\Delta\epsilon_{WS}$ through the expressions:

$$K_{WS} = \frac{k_{WS}^{-}}{k_{WS}^{+}} = e^{\beta\Delta\epsilon_{WS}} \tag{1}$$

where $\beta = 1/(k_B T)$ is one over Boltzmann's constant times the temperature. When a synKin W binds an unphosphorylated synSub S^u and forms a complex WS^u, it can phosphorylate the synSub at a rate governed by the kinetic parameter k_{WS}^{p} resulting in the synKin/phosphorylated synSub complex WS^p. In addition, we assume a background synSub phosphorylation rate k_{bg}^{p} and background dephosphorylation rate k_{bg}^{u}. We assume these background rates are insensitive to whether synSub is bound to the synKin. Collectively, this model can be summarized by the reactions:

$$W + S^u \leftrightarrows WS^u \rightarrow WS^p \leftrightarrows W + S^p \tag{2}$$

$$S^p \leftrightarrows S^u \tag{3}$$

$$WS^p \leftrightarrows WS^u \tag{4}$$

The first line includes all synKin-dependent reactions (binding, dissociation, phosphorylation) while the second and third lines denote background phosphorylation/dephosphorylation for unbound and bound synSub, respectively. This can be summarized with the corresponding kinetic equations:

$$\frac{d[S^p]}{dt} = k_{WS}^{-}[WS^p] - k_{WS}^{+}[W][S^p] + k_{bg}^{p}[S^u] - k_{bg}^{u}[S^p] \tag{5}$$

$$\frac{d[WS^p]}{dt} = k_{WS}^{+}[W][S^p] - k_{WS}^{-}[WS^p] + k_{WS}^{p}[WS^u] + k_{bg}^{p}[WS^u] - k_{bg}^{u}[WS^p] \tag{6}$$

$$\frac{d[S^u]}{dt} = k_{WS}^{-}[WS^u] - k_{WS}^{+}[W][S^u] + k_{bg}^{u}[S^p] - k_{bg}^{p}[S^u] \quad (7)$$

$$\frac{d[WS^u]}{dt} = k_{WS}^{+}[W][S^u] - k_{WS}^{-}[WS^u] - k_{WS}^{p}[WS^u] + k_{bg}^{u}[WS^p] - k_{bg}^{p}[WS^u] \quad (8)$$

where $[X]$ denotes the intracellular concentration of a protein X. To proceed, it is helpful to define the total concentrations of various components:

- Total unphosphorylated synSub: $[S_T^u] = [S^u] + [WS^u]$
- Total phosphorylated synSub: $[S_T^p] = [S^p] + [WS^p]$
- Total free synSub $[S_f] = [S^p] + [S^u]$
- Total bound synSub $[S_b] = [WS^p] + [WS^u]$
- Total synKin: $[W_T] = [W] + [WS^u] + [WS^p]$
- Total synSub: $[S_T] = [S_T^u] + [S_T^p] = [S^u] + [S^p] + [WS^p] + [WS^u]$

We assume for each individual cell that the total synKin and synSub concentrations, $[W_T]$ and $[S_T]$ respectively, are fixed, conserved quantities and that synKin and synSub proteins are neither created nor destroyed but instead are interconverted between various forms.

Using these conservation laws, at steady state we can rearrange the kinetic equations to yield expressions for "conditional probabilities" for whether an individual synKin will be free, bound to an unphosphorylated synSub, or bound to a phosphorylated synSub:

$$p(W|S^u, S^p) = \frac{[W]}{[W_T]} = \frac{1}{1+\frac{[S^u]+[S^p]}{K_{WS}}} = \frac{1}{Z_W} \quad (9)$$

$$p(WS^u|S^u, S^p) = \frac{[WS^u]}{[W_T]} = \frac{\frac{[S^u]}{K_{WS}}}{1+\frac{[S^u]+[S^p]}{K_{WS}}} = \frac{e^{-\beta(\Delta\epsilon_{WS}-k_BT\log[S^u])}}{Z_W} \quad (10)$$

$$p(WS^p|S^u,S^p)=\frac{[WS^p]}{[W_T]}=\frac{\frac{[S^p]}{K_{WS}}}{1+\frac{[S^u]+[S^p]}{K_{WS}}}=\frac{e^{-\beta(\Delta\epsilon_{WS}-k_BT\log[S^p])}}{Z_W}, \tag{11}$$

With the following serving as the partition function for the synKin:

$$Z_W=1+\frac{[S^u]}{K_{WS}}+\frac{[S^p]}{K_{WS}}=1+e^{-\beta(\Delta\epsilon_{WS}-k_BT\log[S^u])}+e^{-\beta(\Delta\epsilon_{WS}-k_BT\log[S^p])} \tag{12}$$

Similarly, we can solve for the "conditional probabilities" for unphosphorylated synSub to be free or bound to a synKin:

$$p(S^u|W)=\frac{[S^u]}{[S_T^u]}=\frac{1}{1+\frac{[W]}{K_{WS}}}=\frac{1}{Z_{S^u}} \tag{13}$$

$$p(WS^u|W)=\frac{[WS^u]}{[S_T^u]}=\frac{\frac{[W]}{K_{WS}}}{1+\frac{[W]}{K_{WS}}}=\frac{e^{-\beta(\Delta\epsilon_{WS}-k_BT\log[W])}}{Z_{S^u}}, \tag{14}$$

with the following partition function for unphosphorylated synSub:

$$Z_{S^u}=1+\frac{[W]}{K_{WS}}=1+e^{-\beta(\Delta\epsilon_{WS}-k_BT\log[W])} \tag{15}$$

An analogous calculation yields "conditional probabilities" for the state of phosphorylated synSub (free or bound to synKin) of the form:

$$p(S^p|W)=\frac{[S^p]}{[S_T^p]}=\frac{1}{1+\frac{[W]}{K_{WS}}}=\frac{1}{Z_{S^p}} \tag{16}$$

$$p(WS^p|W)=\frac{[WS^p]}{[S_T^p]}=\frac{\frac{[W]}{K_{WS}}}{1+\frac{[W]}{K_{WS}}}=\frac{e^{-\beta(\Delta\epsilon_{WS}-k_BT\log[W])}}{Z_{S^p}} \tag{17}$$

with the following as the partition function for phosphorylated synSub:

$$Z_{S^p} = 1 + \frac{[W]}{K_{WS}} = 1 + e^{-\beta(\Delta\epsilon_{WS} - k_B T \log[W])} \tag{18}$$

Finally, we can solve for the "conditional probabilities" that a synSub protein, independent of phosphorylation state, will be free or bound to a synKin:

$$p(S_f|W) = \frac{[S_f]}{[S_T]} = \frac{1}{1+\frac{[W]}{K_{WS}}} = \frac{1}{Z_f} \tag{19}$$

$$p(S_f|W) = \frac{[S_b]}{[S_T]} = \frac{\frac{[W]}{K_{WS}}}{1+\frac{[W]}{K_{WS}}} = \frac{e^{-\beta(\Delta\epsilon_{WS} - k_B T \log[W])}}{Z_f} \tag{20}$$

with the following partition function for synSub independent of phosphorylation status:

$$Z_f = 1 + \frac{[W]}{K_{WS}} = 1 + e^{-\beta(\Delta\epsilon_{WS} - k_B T \log[W])} \tag{21}$$

To proceed, we sum together Eqs. 5 and 6 to derive a kinetic equation for the total concentration of phosphorylated synSub and combine this with the conditional probability in Eq. 14:

$$\frac{d[S_T^p]}{dt} = k_{WS}^p[WS^u] + k_{bg}^p[S_T^u] - k_{bg}^u[S_T^p] \tag{22}$$

$$= k_{WS}^p[S_T^u]p(WS^u|W) + k_{bg}^p[S_T^u] - k_{bg}^u[S_T^p] \tag{23}$$

$$= k_{WS}^p([S_T] - [S_T^p])p(WS^u|W) + k_{bg}^p([S_T] - [S_T^p]) - k_{bg}^u[S_T^p] \tag{24}$$

Setting this equation to zero, we get an equation for the fraction of synSub that is phosphorylated in terms of the conditional probabilities defined above:

$$\frac{[S_T^p]}{[S_T]} = \frac{k_{WS}^p p(WS^u|W) + k_{bg}^p}{k_{WS}^p p(WS^u|W) + k_{bg}^p + k_{bg}^u} \tag{25}$$

$$= \frac{\tilde{k}_{WS}^{p} p(WS^{u}|W) + \tilde{k}_{bg}^{p}}{\tilde{k}_{WS}^{p} p(WS^{u}|W) + \tilde{k}_{bg}^{p} + 1} \tag{26}$$

where we have defined the reaction velocities relative to the background dephosphorylation rate:

$$\tilde{k}_{WS}^{p} = \frac{k_{WS}^{p}}{k_{bg}^{u}} \tag{27}$$

$$\tilde{k}_{bg}^{p} = \frac{k_{bg}^{p}}{k_{bg}^{u}} \tag{28}$$

These conditional probabilities collectively allow us to numerically solve for the amount of phosphorylated synSub as a function of the kinetic parameters (i.e., dissociation constants and reaction velocities) and total concentration of synKin [W_T] and synSub [S_T] in a cell. Numerically, this can be done as follows. We assume that [W_T] and [S_T] are known. This allows us to find a pair of equations that can be solved for [W] and [S_f]:

$$\frac{[W]}{[W_T]} = \frac{1}{1 + \frac{[S_f]}{K_{WS}}} \tag{29}$$

$$\frac{[S_f]}{[S_T]} = \frac{1}{1 + \frac{[W]}{K_{WS}}} \tag{30}$$

Combining these equations yields a quadratic in terms of S_f:

$$0 = \left(\frac{[S_f]}{K_{WS}}\right)^2 + \left(1 + \frac{[W_T] - [S_T]}{K_{WS}}\right)\frac{[S_f]}{K_{WS}} - \frac{[S_T]}{K_{WS}} \tag{31}$$

Generally, we find that this has one positive solution for [S_f]. Using this solution, we solve for [S_f] and [W] and then use Eq. 26 so solve for $\left[S_T^p\right]$. The remaining concentrations are then straightforward to calculate.

Single phosphorylation cycle. The procedure described above can be generalized to a complete cycle, which is composed of synKin W (“writer"), synSub S (“substrate”), and now a synPhos E (“eraser”) (**Fig. 1D**). Using the notation from the previous section, we divide the possible reactions into two groups, those involving the synKin and synPhos:

$$W + S^u \leftrightarrows WS^u \rightarrow WS^p \leftrightarrows W + S^p \tag{32}$$

$$E + S^p \leftrightarrows ES^p \rightarrow ES^u \leftrightarrows E + S^u \tag{33}$$

and those involving background phosphorylation/dephosphorylation reactions:

$$S^p \leftrightarrows S^u \tag{34}$$

$$WS^p \leftrightarrows WS^u \tag{35}$$

$$ES^p \leftrightarrows ES^u \tag{36}$$

Here, we represent the kinetic parameters at which synSub binds and unbinds synKin and synPhos molecules by k_{WS}^+, k_{WS}^-, k_{ES}^+, k_{ES}^-, respectively. In terms of these constants, we can define the equilibrium disassociation constants K_{WS} and K_{ES} for synKin-synSub and synPhos-synSub complexes and their corresponding binding energies as:

$$K_{WS} = \frac{k_{WS}^-}{k_{WS}^+} = e^{\beta \Delta \epsilon_{WS}} \tag{37}$$

$$K_{ES} = \frac{k_{ES}^-}{k_{ES}^+} = e^{\beta \Delta \epsilon_{ES}} \tag{38}$$

In addition, we denote the phosphorylation rate of synSub by synKin k_{WS}^p, the dephosphorylation rate of synSub by synPhos, k_{ES}^u, the background phosphorylation of synSub (independent of

binding state) by k_{bg}^{p}, and the background dephosphorylation of synSub (also independent of binding state) by k_{bg}^{u}. We can write the kinetic equations for the phosphorylation cycles in terms of these parameters:

$$\frac{d[S^p]}{dt} = k_{WS}^{-}[WS^p] - k_{WS}^{+}[W][S^p] + k_{bg}^{p}[S^u] - k_{bg}^{u}[S^p] \quad (39)$$

$$\frac{d[WS^p]}{dt} = k_{WS}^{+}[W][S^p] - k_{WS}^{-}[WS^p] + k_{WS}^{p}[WS^u] + k_{bg}^{p}[WS^u] - k_{bg}^{u}[WS^p] \quad (40)$$

$$\frac{d[ES^p]}{dt} = k_{ES}^{+}[E][S^p] - k_{ES}^{-}[ES^p] - k_{ES}^{u}[ES^p] + k_{bg}^{p}[ES^u] - k_{bg}^{u}[ES^p] \quad (41)$$

$$\frac{d[S^u]}{dt} = k_{WS}^{-}[WS^u] - k_{WS}^{+}[W][S^u] + k_{bg}^{u}[S^p] - k_{bg}^{p}[S^u] \quad (42)$$

$$\frac{d[WS^u]}{dt} = k_{WS}^{+}[W][S^u] - k_{WS}^{-}[WS^u] - k_{WS}^{p}[WS^u] + k_{bg}^{u}[WS^p] - k_{bg}^{p}[WS^u] \quad (43)$$

$$\frac{d[ES^u]}{dt} = k_{ES}^{+}[E][S^u] - k_{ES}^{-}[ES^u] + k_{ES}^{u}[ES^p] + k_{bg}^{u}[ES^p] - k_{bg}^{p}[ES^u] \quad (44)$$

As before, we denote the total concentrations of various components as:

- Total synKin: $[W_T] = [W] + [WS^p] + [WS^u]$
- Total synPhos: $[E_T] = [E] + [ES^p] + [ES^u]$
- Total synSub: $[S_T] = [S_T^u] + [S_T^p]$
- Total unphosphorylated synSub: $[S_T^u] = [S^u] + [WS^u] + [ES^u]$
- Total phosphorylated synSub: $[S_T^p] = [S^p] + [WS^p] + [ES^p]$
- Total free synSub: $[S_f] = [S^p] + [S^u]$

As with the synKin-synSub pair, at steady-state we can reformulate these equations into “partition functions” to calculate the probability for a single protein to be in a given state. We focus on four

partition functions corresponding to W, E, S^u, and S^p, A synKin W can be in three states: free, bound to S^p, or bound to S^u, with the corresponding partition function:

$$Z_W = 1 + \frac{[S^p]}{K_{WS}} + \frac{[S^u]}{K_{WS}} = 1 + e^{-\beta(\Delta\epsilon_{WS} - k_B T \log[S^p])} + e^{-\beta(\Delta\epsilon_{WS} - k_B T \log[S^u])} \tag{45}$$

Similarly, a synPhos E can also be free, bound to S^u, or bound to S^p resulting in the partition function:

$$Z_E = 1 + \frac{[S^p]}{K_{ES}} + \frac{[S^u]}{K_{ES}} = 1 + e^{-\beta(\Delta\epsilon_{ES} - k_B T \log[S^p])} + e^{-\beta(\Delta\epsilon_{ES} - k_B T \log[S^u])} \tag{46}$$

These two partitions are identical since the binding of synSub to a synKin/synPhos does not depend on the phosphorylation state of the synSub. In terms of these partition functions, we denote the following conditional probabilities:

$$p(W|S^u, S^p, E) = \frac{[W]}{[W_T]} = \frac{1}{Z_W} = \frac{1}{1 + \frac{[S^p] + [S^u]}{K_{WS}}} \tag{47}$$

$$p(WS^u|S^u, S^p, E) = \frac{[WS^u]}{[W_T]} = \frac{e^{-\beta(\Delta\epsilon_{WS} - k_B T \log[S^u])}}{Z_W} = \frac{\frac{[S^u]}{K_{WS}}}{1 + \frac{[S^p] + [S^u]}{K_{WS}}} \tag{48}$$

$$p(WS^p|S^u, S^p, E) = \frac{[WS^p]}{[W_T]} = \frac{e^{-\beta(\Delta\epsilon_{WS} - k_B T \log[S^p])}}{Z_W} = \frac{\frac{[S^p]}{K_{WS}}}{1 + \frac{[S^p] + [S^u]}{K_{WS}}} \tag{49}$$

$$p(E|S^u, S^p, W) = \frac{[E]}{[E_T]} = \frac{1}{Z_E} = \frac{1}{1 + \frac{[S^p] + [S^u]}{K_{ES}}} \tag{50}$$

$$p(ES^u|S^u, S^p, W) = \frac{[ES^u]}{[E_T]} = \frac{e^{-\beta(\Delta\epsilon_{ES} - k_B T \log[S^u])}}{Z_E} = \frac{\frac{[S^u]}{K_{ES}}}{1 + \frac{[S^p] + [S^u]}{K_{ES}}} \tag{51}$$

$$p(ES^p|S^u,S^p,W)=\frac{[ES^p]}{[E_T]}=\frac{e^{-\beta(\Delta\epsilon_{ES}-k_BT\log[S^p])}}{Z_E}=\frac{\frac{[S^p]}{K_{ES}}}{1+\frac{[S^p]+[S^u]}{K_{ES}}} \quad (52)$$

$$p(S^u|E,W)=\frac{[S^u]}{[S_T^u]}=\frac{1}{Z_{S^u}}=\frac{1}{1+\frac{[W]}{K_{WS}}+\frac{[E]}{K_{ES}}} \quad (53)$$

$$p(WS^u|E,W)=\frac{[WS^u]}{[S_T^u]}=\frac{e^{-\beta(\Delta\epsilon_{WS}-k_BT\log[W])}}{Z_{S^u}}=\frac{\frac{[W]}{K_{WS}}}{1+\frac{[W]}{K_{WS}}+\frac{[E]}{K_{ES}}} \quad (54)$$

$$p(ES^u|E,W)=\frac{[ES^u]}{[S_T^u]}=\frac{e^{-\beta(\Delta\epsilon_{ES}-k_BT\log[E])}}{Z_{S^u}}=\frac{\frac{[E]}{K_{ES}}}{1+\frac{[W]}{K_{WS}}+\frac{[E]}{K_{ES}}} \quad (55)$$

$$p(S^p|E,W)=\frac{[S^p]}{[S_T^p]}=\frac{1}{Z_{S^p}}=\frac{1}{1+\frac{[W]}{K_{WS}}+\frac{[E]}{K_{ES}}} \quad (56)$$

$$p(WS^p|E,W)=\frac{[WS^p]}{[S_T^p]}=\frac{e^{-\beta(\Delta\epsilon_{WS}-k_BT\log[W])}}{Z_{S^p}}=\frac{\frac{[W]}{K_{WS}}}{1+\frac{[W]}{K_{WS}}+\frac{[E]}{K_{ES}}} \quad (57)$$

$$p(ES^p|E,W)=\frac{[ES^p]}{[S_T^p]}=\frac{e^{-\beta(\Delta\epsilon_{ES}-k_BT\log[E])}}{Z_{S^p}}=\frac{\frac{[E]}{K_{ES}}}{1+\frac{[W]}{K_{WS}}+\frac{[E]}{K_{ES}}} \quad (58)$$

Finally, we can sum Eqs. 39-41 to derive a kinetic equation for the total phosphorylated synSub and solve this equation at steady state to find:

$$\frac{[S_T^p]}{[S_T]}=\frac{k_{WS}^p p(WS^u|E,W)+k_{bg}^p}{k_{WS}^p p(WS^u|E,W)+k_{ES}^u p(ES^p|E,W)+k_{bg}^p+k_{bg}^u} \quad (59)$$

$$=\frac{\tilde{k}_{WS}^p p(WS^u|E,W)+\tilde{k}_{bg}^p}{\tilde{k}_{WS}^p p(WS^u|E,W)+\tilde{k}_{ES}^u p(ES^p|E,W)+\tilde{k}_{bg}^p+1} \quad (60)$$

where we have defined the reaction velocities as:

$$\tilde{k}_{WS}^{p} = \frac{k_{WS}^{p}}{k_{bg}^{u}} \tag{61}$$

$$\tilde{k}_{ES}^{u} = \frac{k_{ES}^{u}}{k_{bg}^{u}} \tag{62}$$

$$\tilde{k}_{bg}^{p} = \frac{k_{bg}^{p}}{k_{bg}^{u}} \tag{63}$$

Numerical Strategy. These equations allow us to solve for the amount of phosphorylated synSub as a function of $[W_T]$, $[E_T]$, and $[S_T]$ and the kinetic parameters. First, we use the conditional probabilities to solve for $[W]$, $[E]$, and $[S_f]$, yielding:

$$\frac{[W]}{[W_T]} = \frac{1}{1+\frac{[S_f]}{K_{WS}}} \tag{64}$$

$$\frac{[E]}{[E_T]} = \frac{1}{1+\frac{[S_f]}{K_{ES}}} \tag{65}$$

$$\frac{[S_f]}{[S_T]} = \frac{1}{1+\frac{[W]}{K_{WS}}+\frac{[E]}{K_{ES}}} \tag{66}$$

Combining these equations yields the following cubic equation expressed in terms of S_f:

$$0 = \left(\frac{[S_f]}{\sqrt{K_{WS}K_{ES}}}\right)^3 + \left(\frac{K_{WS}+K_{ES}}{\sqrt{K_{WS}K_{ES}}} + \frac{[W_T]+[E_T]-[S_T]}{\sqrt{K_{WS}K_{ES}}}\right)\left(\frac{[S_f]}{\sqrt{K_{WS}K_{ES}}}\right)^2 \tag{67}$$

$$+\left(1 + \frac{[W_T]-[S_T]}{K_{WS}} + \frac{[E_T]-[S_T]}{K_{ES}}\right)\left(\frac{[S_f]}{\sqrt{K_{WS}K_{ES}}}\right) - \frac{[S_T]}{\sqrt{K_{WS}K_{ES}}}.$$

Generally, we find that this has one positive solution for $[S_f]$. Using this solution, we solve for $[W]$ and $[E]$ and then use Eq. 60 to solve for $[S_T^p]$, followed by the calculation of the other concentrations.

Two-step phosphorylation circuit. In this section, we give a summary of the mathematical model used to model the two-step phosphorylation circuit depicted in **Fig. 2A**. The cascade consists of a first phosphorylation cycle: an upstream synKin W, a synPhos E, and the PC protein, which functions as the first cycle's substrate S_1. When the first PC is phosphorylated S_1^p, it can bind a second synSub S_2 and act as a kinase to phosphorylate it. Thus, our model assumes that S_1 cannot bind S_2 unless the former is phosphorylated. In addition, we assume that the first substrate PC can simultaneously bind the second synSub at the same time as the synKin W or synPhos E, but synPhos cannot dephosphorylate S_2^p within the ternary complex. Additionally, we didn't account for synPhos dephosphorylation of S_2^p since it is assumed that interactions between the two proteins are negligible. Since the logic of the derivation and notation is identical to the simpler instances discussed in the single phosphorylation cycle, for brevity we will simply state the main results.

Here we summarize all the reactions in the circuit ($*$ denotes either a p for phosphorylated or an u for unphosphorylated):

$$W + S_1^* \leftrightarrows WS_1^* \tag{68}$$

$$E + S_1^* \leftrightarrows ES_1^* \tag{69}$$

$$S_1^p + S_2^* \leftrightarrows S_1^p S_2^* \tag{70}$$

$$WS_1^p + S_2^* \leftrightarrows WS_1^p S_2^* \leftrightarrows W + S_1^p S_2^* \tag{71}$$

$$ES_1^p + S_2^* \leftrightarrows ES_1^p S_2^* \leftrightarrows E + S_1^p S_2^* \quad (72)$$

First layer (de)phosphorylation:

$$WS_1^u \rightarrow WS_1^p \quad (73)$$

$$ES_1^p \rightarrow ES_1^u \quad (74)$$

$$ES_1^p S_2^* \rightarrow ES_1^u + S_2^* \quad (75)$$

First layer background (de)phosphorylation:

$$S_1^p \leftrightarrows S_1^u \quad (76)$$

$$WS_1^p \leftrightarrows WS_1^u \quad (77)$$

$$ES_1^p \leftrightarrows ES_1^u \quad (78)$$

$$S_1^p S_2^* \rightarrow S_1^u + S_2^* \quad (79)$$

$$WS_1^p S_2^* \rightarrow WS_1^u + S_2^* \quad (80)$$

$$ES_1^p S_2^* \rightarrow ES_1^u + S_2^* \quad (81)$$

Second layer phosphorylation:

$$S_1^p S_2^u \rightarrow S_1^p S_2^p \quad (82)$$

$$WS_1^p S_2^u \rightarrow WS_1^p S_2^p \quad (83)$$

$$ES_1^pS_2^u \rightarrow ES_1^pS_2^p \tag{84}$$

Second layer background dephosphorylation:

$$S_2^p \leftrightarrows S_2^u \tag{85}$$

$$S_1^pS_2^p \leftrightarrows S_1^pS_2^u \tag{86}$$

$$WS_1^pS_2^p \leftrightarrows WS_1^pS_2^u \tag{87}$$

$$ES_1^pS_2^p \leftrightarrows ES_1^pS_2^u \tag{88}$$

Here we summarize conservation laws relating concentrations of various species:

- Total synKin: $[W_T] = [W] + \left[WS_1^p\right] + [WS_1^u] + \left[WS_1^pS_2^u\right] + \left[WS_1^pS_2^p\right]$
- Total synPhos: $[E_T] = [E] + \left[ES_1^p\right] + [ES_1^u] + \left[ES_1^pS_2^u\right] + \left[ES_1^pS_2^p\right]$
- Total PC: $[S_{1T}] = [S_{1T}^u] + \left[S_{1T}^p\right]$
- Total unphosphorylated PC: $[S_{1T}^u] = [S_1^u] + [WS_1^u] + [ES_1^u]$
- Total phosphorylated PC: $\left[S_{1T}^p\right] = \left[S_1^p\right] + \left[WS_1^p\right] + \left[ES_1^p\right] + \left[S_1^pS_2^u\right] + \left[S_1^pS_2^p\right] + \left[WS_1^pS_2^u\right] + \left[WS_1^pS_2^p\right] + \left[ES_1^pS_2^u\right] + \left[ES_1^pS_2^p\right]$
- Total free PC: $\left[S_{1f}\right] = \left[S_1^p\right] + [S_1^u]$
- Total synSub: $[S_{2T}] = [S_{2T}^u] + \left[S_{2T}^p\right]$
- Total unphosphorylated synSub: $[S_{2T}^u] = [S_2^u] + \left[S_1^pS_2^u\right] + \left[WS_1^pS_2^u\right] + \left[ES_1^pS_2^u\right]$
- Total phosphorylated synSub: $\left[S_{2T}^p\right] = \left[S_2^p\right] + \left[S_1^pS_2^p\right] + \left[WS_1^pS_2^p\right] + \left[ES_1^pS_2^p\right]$
- Total free synSub: $\left[S_{2f}\right] = \left[S_2^p\right] + [S_2^u]$

The kinetic parameters in the model are:

- Phosphorylation of PC by synKin: $k^p_{WS_1}$
- Dephosphorylation of PC by synPhos: $k^u_{ES_1}$
- Phosphorylation of synSub by PC: $k^p_{S_1,S_2}$
- Background (de)phosphorylation of PC (independent of binding state): $k^p_{S_1,bg}, k^u_{S_1,bg}$
- Background (de)phosphorylation of synSub (independent of binding state): $k^p_{S_2,bg}, k^u_{S_2,bg}$

The equilibrium binding energies and corresponding disassociation constants can be written in terms of the kinetic constants as follows:

synKin + PC:

$$K_{WS} = \frac{k^-_{WS}}{k^+_{WS}} = e^{\beta \Delta \epsilon_{WS}} \tag{89}$$

synPhos + PC:

$$K_{ES} = \frac{k^-_{ES}}{k^+_{ES}} = e^{\beta \Delta \epsilon_{ES}} \tag{90}$$

Phosphorylated PC + synSub:

$$K_{S_1S_2} = \frac{k^-_{S_1S_2}}{k^+_{S_1S_2}} = e^{\beta \Delta \epsilon_{S_1S_2}} \tag{91}$$

These constants yield the following kinetic equations:

$$\frac{d[S_1^u]}{dt} = k_{WS}^-[WS_1^u] - k_{WS}^+[W][S_1^u] + k_{ES}^-[ES_1^u] - k_{ES}^+[E][S_1^u] + k_{S_1,bg}^u\left(\left[S_1^p\right] + \left[S_1^p S_2^u\right]\right) - k_{S_1,bg}^p[S_1^u] \tag{92}$$

$$\frac{d[S_1^p]}{dt} = k_{WS}^-\left[WS_1^p\right] - k_{WS}^+[W]\left[S_1^p\right] + k_{ES}^-\left[ES_1^p\right] - k_{ES}^+[E]\left[S_1^p\right] + k_{S_1S_2}^-\left[S_1^p S_2^u\right] - k_{S_1S_2}^+\left[S_1^p\right][S_2^u] + k_{S_1S_2}^-\left[S_1^p S_2^p\right] - k_{S_1S_2}^+\left[S_1^p\right]\left[S_2^p\right] + k_{S_1,bg}^p[S_1^u] - k_{S_1,bg}^u\left[S_1^p\right] \tag{93}$$

$$\frac{d[S_2^u]}{dt} = k_{S_1S_2}^-\left[S_1^p S_2^u\right] - k_{S_1S_2}^+\left[S_1^p\right][S_2^u] + k_{S_1S_2}^-\left[WS_1^p S_2^u\right] - k_{S_1S_2}^+\left[WS_1^p\right][S_2^u] + k_{S_1S_2}^-\left[ES_1^p S_2^u\right] - k_{S_1S_2}^+\left[ES_1^p\right][S_2^u] + k_{ES_1}^u\left[ES_1^p S_2^u\right] + k_{S_1,bg}^u\left(\left[S_1^p S_2^u\right] + \left[WS_1^p S_2^u\right] + \left[ES_1^p S_2^u\right]\right) + k_{S_2,bg}^u\left[S_2^p\right] - k_{S_2,bg}^p[S_2^u] \tag{94}$$

$$\frac{d[S_2^p]}{dt} = k_{S_1S_2}^-\left[S_1^p S_2^p\right] - k_{S_1S_2}^+\left[S_1^p\right]\left[S_2^p\right] + k_{S_1S_2}^-\left[WS_1^p S_2^p\right] - k_{S_1S_2}^+\left[WS_1^p\right]\left[S_2^p\right] + k_{S_1S_2}^-\left[ES_1^p S_2^p\right] - k_{S_1S_2}^+\left[ES_1^p\right]\left[S_2^p\right] + k_{ES_1}^u\left[ES_1^p S_2^p\right] + k_{S_1,bg}^u\left(\left[S_1^p S_2^p\right] + \left[WS_1^p S_2^p\right] + \left[ES_1^p S_2^p\right]\right) + k_{S_2,bg}^p[S_2^u] - k_{S_2,bg}^u\left[S_2^p\right] \tag{95}$$

$$\frac{d[WS_1^u]}{dt} = k_{WS}^+[W][S_1^u] - k_{WS}^-[WS_1^u] - k_{WS_1}^p[WS_1^u] + k_{S_1,bg}^u\left(\left[WS_1^p\right] + \left[WS_1^p S_2^u\right] + \left[WS_1^p S_2^p\right]\right) - k_{S_1,bg}^p[WS_1^u] \tag{96}$$

$$\frac{d[ES_1^u]}{dt} = k_{ES}^+[E][S_1^u] - k_{ES}^-[ES_1^u] + k_{ES_1}^u\left(\left[ES_1^p\right] + \left[ES_1^p S_2^u\right] + \left[ES_1^p S_2^p\right]\right) + k_{S_1,bg}^u\left(\left[ES_1^p\right] + \left[ES_1^p S_2^u\right] + \left[ES_1^p S_2^p\right]\right) - k_{S_1,bg}^p[ES_1^u] \tag{97}$$

$$\frac{d[WS_1^p]}{dt} = k_{WS}^+[W]\left[S_1^p\right] - k_{WS}^-\left[WS_1^p\right] + k_{S_1S_2}^-\left[WS_1^p S_2^u\right] - k_{S_1S_2}^+\left[WS_1^p\right][S_2^u] + k_{S_1S_2}^-\left[WS_1^p S_2^p\right] - k_{S_1S_2}^+\left[WS_1^p\right]\left[S_2^p\right] + k_{WS_1}^p[WS_1^u] + k_{S_1,bg}^p[WS_1^u] - k_{S_1,bg}^u\left[WS_1^p\right] \tag{98}$$

$$\frac{d[ES_1^p]}{dt} = k_{ES}^+[E]\left[S_1^p\right] - k_{ES}^-\left[ES_1^p\right] + k_{S_1S_2}^-\left[ES_1^p S_2^u\right] - k_{S_1S_2}^+\left[ES_1^p\right][S_2^u] + k_{S_1S_2}^-\left[ES_1^p S_2^p\right] - k_{S_1S_2}^+\left[ES_1^p\right]\left[S_2^p\right] - k_{ES_1}^u\left[ES_1^p\right] + k_{S_1,bg}^p[ES_1^u] - k_{S_1,bg}^u\left[ES_1^p\right] \tag{99}$$

$$\frac{d[S_1^p S_2^u]}{dt} = k_{S_1S_2}^+\left[S_1^p\right][S_2^u] - k_{S_1S_2}^-\left[S_1^p S_2^u\right] + k_{WS}^-\left[WS_1^p S_2^u\right] - k_{WS}^+[W]\left[S_1^p S_2^u\right] + k_{ES}^-\left[ES_1^p S_2^u\right] - k_{ES}^+[E]\left[S_1^p S_2^u\right] - k_{S_1S_2}^p\left[S_1^p S_2^u\right] - k_{S_1,bg}^u\left[S_1^p S_2^u\right] + k_{S_2,bg}^u\left[S_1^p S_2^p\right] - k_{S_2,bg}^p\left[S_1^p S_2^u\right] \tag{100}$$

$$\frac{d[S_1^p S_2^p]}{dt} = k^+_{S_1S_2}[S_1^p][S_2^p] - k^-_{S_1S_2}[S_1^p S_2^p] + k^-_{WS}[WS_1^p S_2^p] - k^+_{WS}[W][S_1^p S_2^p] + k^-_{ES}[ES_1^p S_2^p] - k^+_{ES}[E][S_1^p S_2^p] + k^p_{S_1S_2}[S_1^p S_2^u] - k^u_{S_1,bg}[S_1^p S_2^p] + k^p_{S_2,bg}[S_1^p S_2^u] - k^u_{S_2,bg}[S_1^p S_2^p] \quad (101)$$

$$\frac{d[WS_1^p S_2^u]}{dt} = k^+_{WS}[W][S_1^p S_2^u] - k^-_{WS}[WS_1^p S_2^u] + k^+_{S_1S_2}[WS_1^p][S_2^u] - k^-_{S_1S_2}[WS_1^p S_2^u] - k^p_{S_1S_2}[WS_1^p S_2^u] - k^u_{S_1,bg}[WS_1^p S_2^u] + k^u_{S_2,bg}[WS_1^p S_2^p] - k^p_{S_2,bg}[WS_1^p S_2^u] \quad (102)$$

$$\frac{d[ES_1^p S_2^u]}{dt} = k^+_{ES}[E][S_1^p S_2^u] - k^-_{ES}[ES_1^p S_2^u] + k^+_{S_1S_2}[ES_1^p][S_2^u] - k^-_{S_1S_2}[ES_1^p S_2^u] - k^u_{ES_1}[ES_1^p S_2^u] - k^p_{S_1S_2}[ES_1^p S_2^u] - k^u_{S_1,bg}[ES_1^p S_2^u] + k^u_{S_2,bg}[ES_1^p S_2^p] - k^p_{S_2,bg}[ES_1^p S_2^u] \quad (103)$$

$$\frac{d[WS_1^p S_2^p]}{dt} = k^+_{WS}[W][S_1^p S_2^p] - k^-_{WS}[WS_1^p S_2^p] + k^+_{S_1S_2}[WS_1^p][S_2^p] - k^-_{S_1S_2}[WS_1^p S_2^p] + k^p_{S_1S_2}[WS_1^p S_2^u] - k^u_{S_1,bg}[WS_1^p S_2^p] + k^p_{S_2,bg}[WS_1^p S_2^u] - k^u_{S_2,bg}[WS_1^p S_2^p] \quad (104)$$

$$\frac{d[ES_1^p S_2^p]}{dt} = k^+_{ES}[E][S_1^p S_2^p] - k^-_{ES}[ES_1^p S_2^p] + k^+_{S_1S_2}[ES_1^p][S_2^p] - k^-_{S_1S_2}[ES_1^p S_2^p] - k^u_{ES_1}[ES_1^p S_2^p] + k^p_{S_1S_2}[ES_1^p S_2^u] - k^u_{S_1,bg}[ES_1^p S_2^p] + k^p_{S_2,bg}[ES_1^p S_2^u] - k^u_{S_2,bg}[ES_1^p S_2^p] \quad (105)$$

Which can be reformulated into partition functions:

synKin:

$$Z_W = 1 + \frac{[S_1^p]}{K_{WS}} + \frac{[S_1^u]}{K_{WS}} + \frac{[S_1^p][S_2^u]}{K_{WS}K_{S_1S_2}} + \frac{[S_1^p][S_2^p]}{K_{WS}K_{S_1S_2}}$$
$$= 1 + e^{-\beta(\Delta\epsilon_{WS} - k_BT\log[S_1^p])} + e^{-\beta(\Delta\epsilon_{WS} - k_BT\log[S_1^u])} + e^{-\beta(\Delta\epsilon_{WS} + \Delta\epsilon_{S_1S_2} - k_BT\log[S_1^p] - k_BT\log[S_2^u])} + e^{-\beta(\Delta\epsilon_{WS} + \Delta\epsilon_{S_1S_2} - k_BT\log[S_1^p] - k_BT\log[S_2^p])} \quad (106)$$

synPhos:

$$Z_E = 1 + \frac{[S_1^p]}{K_{ES}} + \frac{[S_1^u]}{K_{ES}} + \frac{[S_1^p][S_2^u]}{K_{ES}K_{S_1S_2}} + \frac{[S_1^p][S_2^p]}{K_{ES}K_{S_1S_2}}$$

$$= 1 + e^{-\beta(\Delta\epsilon_{ES} - k_BT\log[S_1^p])} + e^{-\beta(\Delta\epsilon_{ES} - k_BT\log[S_1^u])} + e^{-\beta(\Delta\epsilon_{ES} + \Delta\epsilon_{S_1S_2} - k_BT\log[S_1^p] - k_BT\log[S_2^u])} +$$

$$e^{-\beta(\Delta\epsilon_{ES} + \Delta\epsilon_{S_1S_2} - k_BT\log[S_1^p] - k_BT\log[S_2^p])} \quad (107)$$

Unphosphorylated PC:

$$Z_{S_1^u} = 1 + \frac{[W]}{K_{WS}} + \frac{[E]}{K_{ES}} = 1 + e^{-\beta(\Delta\epsilon_{WS} - k_BT\log[W])} + e^{-\beta(\Delta\epsilon_{ES} - k_BT\log[E])} \quad (108)$$

Phosphorylated PC:

$$Z_{S_1^p} = 1 + \frac{[W]}{K_{WS}} + \frac{[E]}{K_{ES}} + \frac{[S_2^u]}{K_{S_1S_2}} + \frac{[S_2^p]}{K_{S_1S_2}} + \frac{[W][S_2^u]}{K_{WS}K_{S_1S_2}} + \frac{[W][S_2^p]}{K_{WS}K_{S_1S_2}} + \frac{[E][S_2^u]}{K_{ES}K_{S_1S_2}} + \frac{[E][S_2^p]}{K_{ES}K_{S_1S_2}}$$

$$= 1 + e^{-\beta(\Delta\epsilon_{WS} - k_BT\log[W])} + e^{-\beta(\Delta\epsilon_{ES} - k_BT\log[E])} + e^{-\beta(\Delta\epsilon_{S_1S_2} - k_BT\log[S_2^u])} + e^{-\beta(\Delta\epsilon_{S_1S_2} - k_BT\log[S_2^p])} +$$

$$e^{-\beta(\Delta\epsilon_{WS} + \Delta\epsilon_{S_1S_2} - k_BT\log[W] - k_BT\log[S_2^u])} + e^{-\beta(\Delta\epsilon_{WS} + \Delta\epsilon_{S_1S_2} - k_BT\log[W] - k_BT\log[S_2^p])} +$$

$$e^{-\beta(\Delta\epsilon_{ES} + \Delta\epsilon_{S_1S_2} - k_BT\log[E] - k_BT\log[S_2^u])} + e^{-\beta(\Delta\epsilon_{ES} + \Delta\epsilon_{S_1S_2} - k_BT\log[E] - k_BT\log[S_2^p])} \quad (109)$$

Unphosphorylated synSub:

$$Z_{S_2^u} = 1 + \frac{[S_1^p]}{K_{S_1S_2}} + \frac{[W][S_1^p]}{K_{WS}K_{S_1S_2}} + \frac{[E][S_1^p]}{K_{ES}K_{S_1S_2}}$$

$$= 1 + e^{-\beta(\Delta\epsilon_{S_1S_2} - k_BT\log[S_1^p])} + e^{-\beta(\Delta\epsilon_{WS}\Delta\epsilon_{S_1S_2} - k_BT\log[W] - k_BT\log[S_1^p])} +$$

$$e^{-\beta(\Delta\epsilon_{ES}\Delta\epsilon_{S_1S_2} - k_BT\log[E] - k_BT\log[S_1^p])} \quad (110)$$

Phosphorylated synSub:

$$Z_{S_2^p} = 1 + \frac{[S_1^p]}{K_{S_1S_2}} + \frac{[W][S_1^p]}{K_{WS}K_{S_1S_2}} + \frac{[E][S_1^p]}{K_{ES}K_{S_1S_2}}$$

$$= 1 + e^{-\beta(\Delta\epsilon_{S_1S_2} - k_BT\log[S_1^p])} + e^{-\beta(\Delta\epsilon_{WS}\Delta\epsilon_{S_1S_2} - k_BT\log[W] - k_BT\log[S_1^p])} +$$

$$e^{-\beta(\Delta\epsilon_{ES}\Delta\epsilon_{S_1S_2} - k_BT\log[E] - k_BT\log[S_1^p])} \quad (111)$$

The associated probabilities can be constructed from the partition functions in the same manner as the previous examples. The probabilities for each free component are:

$$p\left(W\middle|S_1^u,S_1^p,S_2^u,S_2^p\right)=\frac{[W]}{[W_T]}=\frac{1}{1+\frac{[S_1^p]}{K_{WS}}+\frac{[S_1^u]}{K_{WS}}+\frac{[S_1^p][S_2^u]}{K_{WS}K_{S_1S_2}}+\frac{[S_1^p][S_2^p]}{K_{WS}K_{S_1S_2}}} \tag{112}$$

$$p\left(E\middle|S_1^u,S_1^p,S_2^u,S_2^p\right)=\frac{[E]}{[E_T]}=\frac{1}{1+\frac{[S_1^p]}{K_{ES}}+\frac{[S_1^u]}{K_{ES}}+\frac{[S_1^p][S_2^u]}{K_{ES}K_{S_1S_2}}+\frac{[S_1^p][S_2^p]}{K_{ES}K_{S_1S_2}}} \tag{113}$$

$$p(S_1^u|W,E)=\frac{[S_1^u]}{[S_{1T}^u]}=\frac{1}{1+\frac{[W]}{K_{WS}}+\frac{[E]}{K_{ES}}} \tag{114}$$

$$p\left(S_1^p\middle|W,E,S_2^u,S_2^p\right)=\frac{[S_1^p]}{[S_{1T}^p]}=\frac{1}{1+\frac{[W]}{K_{WS}}+\frac{[E]}{K_{ES}}+\frac{[S_2^u]}{K_{S_1S_2}}+\frac{[S_2^p]}{K_{S_1S_2}}+\frac{[W][S_2^u]}{K_{WS}K_{S_1S_2}}+\frac{[W][S_2^p]}{K_{WS}K_{S_1S_2}}+\frac{[E][S_2^u]}{K_{ES}K_{S_1S_2}}+\frac{[E][S_2^p]}{K_{ES}K_{S_1S_2}}} \tag{115}$$

$$p\left(S_2^u\middle|W,E,S_1^p\right)=\frac{[S_2^u]}{[S_{2T}^u]}=\frac{1}{1+\frac{[S_1^p]}{K_{S_1S_2}}+\frac{[W][S_1^p]}{K_kK_{S_1S_2}}+\frac{[E][S_1^p]}{K_{ES}K_{S_1S_2}}} \tag{116}$$

$$p\left(S_2^p\middle|W,E,S_1^p\right)=\frac{[S_2^p]}{[S_{2T}^p]}=\frac{1}{1+\frac{[S_1^p]}{K_{S_1S_2}}+\frac{[W][S_1^p]}{K_{WS}K_{S_1S_2}}+\frac{[E][S_1^p]}{K_{ES}K_{S_1S_2}}}. \tag{117}$$

We will also need the following probabilities for bound components:

$$p(WS_1^u)=p(WS_1^u|W,E)=\frac{\frac{[W]}{K_{WS}}}{Z_{S_1^u}} \tag{118}$$

$$p\left(ES_1^p\right)=p\left(ES_1^p\middle|W,E,S_2^u,S_2^p\right)=\frac{\frac{[E]}{K_{ES}}}{Z_{S_1^p}} \tag{119}$$

$$p\left(ES_1^pS_2^u\right)=p\left(ES_1^pS_1^u\middle|W,E,S_2^u,S_2^p\right)=\frac{\frac{[E][S_2^u]}{K_kK_{S_1S_2}}}{Z_{S_1^p}} \tag{120}$$

$$p\left(ES_1^pS_2^p\right) = p\left(ES_1^pS_1^p\middle|W,E,S_2^u,S_2^p\right) = \frac{\frac{[E]\left[S_2^p\right]}{K_{ES}K_{S_1S_2}}}{Z_{S_1^p}} \tag{121}$$

$$p\left(S_1^pS_2^u\right) = p\left(S_1^pS_2^u\middle|W,E,S_1^p\right) = \frac{\frac{\left[S_1^p\right]}{K_{S_1S_2}}}{Z_{S_2^u}} \tag{122}$$

$$p\left(WS_1^pS_2^u\right) = p\left(WS_1^pS_2^u\middle|W,E,S_1^p\right) = \frac{\frac{[W]\left[S_1^p\right]}{K_{WS}K_{S_1S_2}}}{Z_{S_2^u}} \tag{123}$$

$$p\left(ES_1^pS_2^u\right) = p\left(ES_1^pS_2^u\middle|W,E,S_1^p\right) = \frac{\frac{[E]\left[S_1^p\right]}{K_{ES}K_{S_1S_2}}}{Z_{S_2^u}}. \tag{124}$$

Next, using the kinetic equation at steady state and the above probabilities, we can derive formulas for the fraction of each substrate that is phosphorylated:

$$\begin{aligned}\frac{\left[S_{1T}^p\right]}{[S_{1T}]} &= \frac{k_{WS_1}^p p(WS_1^u)+k_{S_1,bg}^p}{k_{WS_1}^p p(WS_1^u)+k_{ES_1}^u\left[p(ES_1^p)+p(ES_1^pS_2^u)+p(ES_1^pS_2^p)\right]+k_{S_1,bg}^p+k_{S_1,bg}^u} \\ &= \frac{\tilde{k}_{WS_1}^p p(WS_1^u)+\tilde{k}_{S_1,bg}^p}{\tilde{k}_{WS_1}^p p(WS_1^u)+\tilde{k}_{ES_1}^u\left[p(ES_1^p)+p(ES_1^pS_2^u)+p(ES_1^pS_2^p)\right]+\tilde{k}_{S_1,bg}^p+1}\end{aligned} \tag{125}$$

$$\begin{aligned}\frac{\left[S_{2T}^p\right]}{[S_{2T}]} &= \frac{k_{S_1S_2}^p\left[p(S_1^pS_2^u)+p(WS_1^pS_2^u)+p(ES_1^pS_2^u)\right]+k_{S_2,bg}^p}{k_{S_1S_2}^p\left[p(S_1^pS_2^u)+p(WS_1^pS_2^u)+p(ES_1^pS_2^u)\right]+k_{S_2,bg}^p+k_{S_1,bg}^u} \\ &= \frac{\tilde{k}_{S_1S_2}^p\left[p(S_1^pS_2^u)+p(WS_1^pS_2^u)+p(ES_1^pS_2^u)\right]+\tilde{k}_{S_2,bg}^p}{\tilde{k}_{S_1S_2}^p\left[p(S_1^pS_2^u)+p(WS_1^pS_2^u)+p(ES_1^pS_2^u)\right]+\tilde{k}_{S_2,bg}^p+1},\end{aligned} \tag{126}$$

where we have:

$$\tilde{k}_{WS_1}^p = \frac{k_{WS_1}^p}{k_{S_1,bg}^u} \tag{127}$$

$$\tilde{k}_{ES_1}^u = \frac{k_{ES_1}^u}{k_{S_1,bg}^u} \tag{128}$$

$$\tilde{k}^{p}_{S_1,bg} = \frac{k^{p}_{S_1,bg}}{k^{u}_{S_1,bg}} \tag{129}$$

$$\tilde{k}^{p}_{S_1S_2} = \frac{k^{p}_{S_1S_2}}{k^{u}_{S_2,bg}} \tag{130}$$

$$\tilde{k}^{p}_{S_2,bg} = \frac{k^{p}_{S_2,bg}}{k^{u}_{S_2,bg}}. \tag{131}$$

Numerical Strategy. We assume that $[W_T]$, $[E_T]$, $[S_{1T}]$ and $[S_{2T}]$ are known. Using a numerical root finding scheme, we solve the following equations for $[W]$, $[E]$, $[S_{1f}]$, $[S_{2f}]$, $[S_1^p]$, and $[S_{1T}^p]$:

$$\frac{[W]}{[W_T]} = \frac{1}{1+\frac{[s_1^f]}{K_{WS}}+\frac{[s_1^p][s_2^f]}{K_{WS}K_{S_1S_2}}} \tag{132}$$

$$\frac{[E]}{[E_T]} = \frac{1}{1+\frac{[s_1^f]}{K_{ES}}+\frac{[s_1^p][s_2^f]}{K_{ES}K_{S_1S_2}}} \tag{133}$$

$$\frac{[S_1^u]}{[S_{1T}^u]} = \frac{1}{1+\frac{[W]}{K_{WS}}+\frac{[E]}{K_{ES}}} \tag{134}$$

$$\frac{[S_1^p]}{[S_{1T}^p]} = \frac{1}{1+\frac{[W]}{K_{WS}}+\frac{[E]}{K_{ES}}+\frac{[s_2^f]}{K_{S_1S_2}}+\frac{[W][s_2^f]}{K_{WS}K_{S_1S_2}}+\frac{[E][s_2^f]}{K_{ES}K_{S_1S_2}}} \tag{135}$$

$$\frac{[s_2^f]}{[S_{2T}]} = \frac{1}{1+\frac{[s_1^p]}{K_{S_1S_2}}+\frac{[W][s_1^p]}{K_{WS}K_{S_1S_2}}+\frac{[E][s_1^p]}{K_{ES}K_{S_1S_2}}} \tag{136}$$

with Eqs. 125 and 126 above.

Data fitting and prediction of phosphorylation levels

In this section, we outline how the models described above can be used to fit our flow cytometry data and then predict intracellular phosphorylation levels for different circuit designs

based on their part compositions. Our data fitting procedure has three components: **i)** conversion of fluorophore-conjugated antibody fluorescence intensities to EGFP fluorescent equivalents, which acts as a common intracellular "pseudo concentration" units that can be used to relate different species composing the circuit; **ii)** a maximum-likelihood fitting procedure to remove intrinsic cell background fluorescence and estimate the signal underlying each component expression level measurement; and **iii)** a maximum-likelihood fitting procedure to fit phosphorylation measurements to the thermodynamic models and infer the parameters that underlie the biophysical behavior of each individual part.

Conversion of fluorescence data to uniform units. A general problem with fitting mathematical models to multi-color flow cytometry data is that different fluorophore-tagged antibodies typically have differential staining efficacies and fluorescence intensities, making it a challenge to describe the components of a measured molecular system in terms of stoichiometric equivalents. To address this, we converted antibody fluorescence measurements into EGFP fluorescence units, which served as proxy intracellular concentration units for the model. We refer to these units as MOCUs (model-operable concentration units). This conversion was accomplished by constructing chimeras in which EGFP was fused to epitope-tagged phosphorylation cycle components: FLAG-synKin-EGFP, HA-synPhos-EGFP, MYC-synKin-EGFP, MYC-PC-EGFP, and V5-synKin-synSub-EGFP (**fig. S10**). Because EGFP and the epitopes are covalently linked, they are expressed in cells at a 1:1 ratio and can be used to relate fluorescence values from each of the antibody-conjugated fluorophores to one another. To ensure that the antibody binding efficiencies to the EGFP-fused constructs were similar to circuit components, we avoided introducing significant structural changes by appending EGFP directly to the C-terminus of the original protein.

To obtain measurements of the EGFP-epitope chimeras, we transfected the **fig. S10** constructs into HEK293T cells and stained them with a corresponding antibody panel (see

Materials and Methods) to measure distributions of antibody fluorophore and EGFP fluorescence. We then fit a linear equation relating the two fluorescence measurements on a log-log scale, assuming a power-law relationship between the measurements:

$$\log[\text{EGFP fluorescence}] = a \log[\text{antibody fluorescence}] + b \tag{137}$$

where constants a and b are factors that convert antibody fluorophore fluorescence into EGFP units.

Before fitting our biophysical models to the phosphorylation cycle data, we removed the background fluorescence from the EGFP units for component expression data (e.g., expression of synKin, synSub, synPhos, etc., but not phosphorylated synSub) (**fig. S11**). To do this, we assume that each fluorescence measurement m is composed of a "signal" c, which corresponds to the actual circuit component concentration, and a "background" ε that comes from cell autofluorescence and non-specific staining:

$$m = c + \varepsilon \tag{138}$$

To infer the concentration c from a measurement m, we effectively average over all possible background fluorescence values ε observed in the control experiments (see description of empty cell experiments) that are consistent with the measurement. This "error model" averaging allows for better treatment of background autofluorescence. To represent this process, we assume that the probability of a measurement is conditional upon on a specific combination of concentration, and that background fluorescence, represented by a delta function:

$$p(m|c, \varepsilon) = \delta\big(m - (c + \varepsilon)\big) \tag{139}$$

which enforces the condition in Eq. (138). For each component, we separately measure the distribution for the background autofluorescence $p_\varepsilon(\varepsilon)$ from experiments. We further assume that the concentration of each component follows a log-normal distribution:

$$p_c(c|\mu,\sigma) = \exp\left[-\frac{(\log c-\mu)^2}{2\sigma^2}\right]\Theta(c) \tag{140}$$

where μ and σ are unknown parameters that we determine from the data (see below for fitting procedure). We will allow each component from each experiment to have its own values of μ and σ. Next, we write the likelihood of a measurement of component m in a cell given μ and σ by integrating over all possible underlying concentrations c and background fluorescence values ε as follows:

$$\begin{aligned} p(m|\mu,\sigma) &= \int d\varepsilon dc\, p(m|c,\varepsilon)p_c(c|\mu\sigma)p_\varepsilon(\varepsilon) \\ &= \int d\varepsilon dc\, \delta\big(m-(c+\varepsilon)\big)p_c(c|\mu,\sigma)p_\varepsilon(\varepsilon) \\ &= \int d\varepsilon p_\varepsilon(\varepsilon)p_c(m-\varepsilon|\mu,\sigma) \end{aligned} \tag{141}$$

To estimate μ and σ for a given component in a single experiment, we then perform Maximum Likelihood Estimation (MLE) over all cells in a population. We sum the negative log likelihood from Eq. (141),

$$L = -\frac{1}{N_d}\sum_i \log p(m_i|\mu,\sigma) \tag{142}$$

where the sum i runs over the N_d cells being fit. We find our MLE estimators by choosing $\hat{\mu}$ and $\hat{\sigma}$ that minimize L. From these fit parameters, we obtain an approximation of the distribution of underlying concentration c. Next, we use Bayes's rule to write the conditional probability of a concentration c given a measurement m:

$$p(c|m,\hat{\mu},\hat{\sigma}) = \frac{p(m|c)p_c(c|\hat{\mu},\hat{\sigma})}{p(m)}$$

$$= \frac{\int d\varepsilon p(m|c,\varepsilon)p_c(c|\hat{\mu},\hat{\sigma})p_\varepsilon(\varepsilon)}{\int dcd\varepsilon p(m|c,\varepsilon)p_c(c|\hat{\mu},\hat{\sigma})p_\varepsilon(\varepsilon)} \quad (143)$$

Using this formula, we can then infer the average concentration underlying the measurement for each individual cell:

$$\langle c(m)\rangle = \frac{\int dcc \int d\varepsilon\delta\big(m-(c+\varepsilon)\big)p_\varepsilon(\varepsilon)p(c|m,\hat{\mu},\hat{\sigma})}{\int d\varepsilon p_\varepsilon(\varepsilon)\Theta(m-\varepsilon)}$$

$$= \frac{\int d\varepsilon p_\varepsilon(\varepsilon)p(m-\varepsilon|m,\hat{\mu},\hat{\sigma})(m-\varepsilon)}{\int d\varepsilon p_\varepsilon(\varepsilon)} = m - \langle\varepsilon(m)\rangle \quad (144)$$

The quantity $\langle\varepsilon(m)\rangle$ represents the average value of the background noise underlying the measurement m. The average background-subtracted concentrations $\langle c(m)\rangle$ of the circuit components in each cell (synKin, synSub, synPhos)—the MOCU units—then serves as input to our thermodynamic models, as discussed in the next section.

Fitting thermodynamic models to infer biophysical parameters for a single phosphorylation cycle. As stated above, our models yield the concentration of phosphorylated synSub (output of circuit) as a function of the total synKin, synPhos, and synSub concentrations and fitted parameters: the equilibrium disassociation, enzymatic activities, and an extra parameter σ describing the variance of the log-normal distribution for phosphorylated synSub that we introduce below (**fig. S12A**).

We use a similar setup to the previous section, where measurements m of output phosphorylated synSub reflect a combination of a concentration c and background ε with conditional probability:

$$p(m|c,\varepsilon) = \delta\big(m-(c+\varepsilon)\big). \quad (145)$$

For the concentration c, we again assume a log-normal distribution, but choose the mean $\mu = \log \bar{c}$ that depends on the fit parameters of the model θ and the input concentrations of components in the cell inferred in the previous section:

$$p_c(c|\theta,\sigma) = exp\left[-\frac{(\log c - \log \bar{c}(\theta))^2}{2\sigma^2}\right]\Theta(c). \tag{146}$$

To write the likelihood of a measurement, we average over all possible values of the background autofluorescence noise $p_\varepsilon(\varepsilon)$ and concentration c. This yields the following:

$$\begin{aligned} p(m|\theta,\sigma) &= \int d\varepsilon dc\, p(m|c,\varepsilon)p_c(c|\theta,\sigma)p_\varepsilon(\varepsilon) \\ &= \int d\varepsilon dc\, \delta\big(m-(c+\varepsilon)\big)p_c(c|\theta,\sigma)p_\varepsilon(\varepsilon) \\ &= \int d\varepsilon p_\varepsilon(\varepsilon)p_c(m-\varepsilon|\theta,\sigma). \end{aligned} \tag{147}$$

The negative log likelihood summed over the data is then:

$$L = -\frac{1}{N_d}\log p(m_i|\theta,\sigma). \tag{148}$$

where the sum runs over measured cells. To estimate parameters, we perform standard MLE (**fig. S11**, bottom right). To estimate errors, we vary each parameter θ_i independently by increasing and decreasing the parameter until the log-likelihood function changes by 1% from its minimum value. This yields two-sided error bars that can have very different confidence intervals for increasing and decreasing a parameter value. Such an approach is necessary as many parameters may be unbounded either above or below as is the case for some binding affinities (**fig. S12B**). This procedure yields error bars that are a reasonable proxy for confidence; any values from this range will generate similar fitting results within 99% of the MLE (**fig. S11**).

To compare LZ affinity values obtained from fitting with *in vitro* disassociation constants (K_d) reported in the literature (*31*), we calculated the corresponding *in vitro* K_d values and set the medium LZ affinity value obtained from fitting to be equal to the in vitro K_d, then converted the other fitted zipper affinities to K_d values using their ratios to the medium zipper affinity. This approach revealed that the fitted LZ affinities were very close (within 2-fold) to the *in vitro* values, indicating high accuracy in our modeling fitting.

Generating model predictions for a single phosphorylation cycle. After we fit our model to a dataset and obtained estimates for all biophysical parameters, we use both our thermodynamic and MLE model to generate predicted distributions of phosphorylated synSub in antibody fluorescence units (**fig. S11**, right bottom to top). For the first step in this process, we use the thermodynamic model to predict the average concentration of phosphorylated synSub in each cell based on the total concentrations and of each component in MOCU, along with the previously estimated kinetic parameters. For each individual cell, this quantity represents a "denoised" estimate of the phosphorylated synSub concentration generated by the model. Mathematically, this quantity corresponds to the mean $\log \bar{c}$ of the log-normal distribution for concentration in Eq. 146. Next, for each cell, we use these generated values of average concentration $\log \bar{c}$ to randomly sample from the concentration distributions in Eq. 146, providing us with a simulated measurement of concentration of phosphorylated synSub in MOCU. To convert to EGFP units for an individual cell, we than randomly sample from the experimental background autofluorescence distribution $p_{\varepsilon}(\varepsilon)$ for phosphorylated synSub (in EGFP units) and add this to the predicted concentration. Finally, we utilize our EGFP-to-antibody-fluorescence conversion standard from Eq. 137 to convert our predicted phosphorylated synSub/PC to antibody fluorescence. The final result of this four-step process is a distribution of simulated single cell antibody measurements created by our model which can be directly compared to the experimental distribution.

Generating model predictions for a single phosphorylation cycle design space. We next used our fitted phosphorylation cycle model to simulate phosphorylation equilibria across our entire part-determined design space, which contained 216 part combinations of different LZ affinities, catalytic activities, and expression levels (**Fig. 1E** and **fig. S12A**). For cycle compositions that don't involve adjusting synKin, synSub, and synPhos expression levels, we applied fit parameters from the model to predict phosphorylation for each cell in the distribution of the cycle composition shown in **Fig. 1D**, and then calculated mean phosphorylation values from the entire distribution. To predict phosphorylation for compositions with Kozak-tuned expression levels, experimentally generated expression profiles for each of the components used to calculate mean phosphorylation.

Using the model to map the behavior space allowed us to comprehensively investigate how part usage varied for different phosphorylation levels (**fig. S13A**). After plotting mean values in a beeswarm plot (**fig. S13B**), we examined three different bins representing low, medium, and high phosphorylation, calculating parts frequencies for synKin, synPhos, and synSub (**fig. S13B**). As expected, we observed that the high phosphorylation bin contains synKin compositions with stronger kinase activity and LZ affinities, but weaker synPhos activity and affinities, while the low bin is enriched for activities and affinities that are weaker for synKin but stronger for synPhos.

Sensitivity analysis for a single phosphorylation cycle. We next sought to analyze the sensitivity of our synthetic phosphorylation cycles to understand whether they were operating in a linear or ultrasensitive regime. As described above our data analysis pipeline generates "denoised" single-cell concentrations for synKin, synSub, synPhos, and phosphorylated synSub in MOCU for all cells within a measured population. For all 216 phosphorylation cycle compositions, we used parameters determined in **Figure 1E** and **F** to generate sensitivity curves inspired by classic Goldbeter-Koshland analysis (*23*) that show the relationship between the noise-model transformed values for phosphorylated synSub and the ratio of [synKin] to [synPhos] (**Fig. S14A**).

To do this, we used parameters that were specific to each cycle composition to generate curves by holding denoised concentrations of synPhos and synSub constant at their mean measured MOCU values, and then uniformly sampling synKin in logarithmic space for synSub phosphorylation levels. From these curves we used the following equation to infer values of interest (*23*):

$$\frac{S_{0.9}}{S_{0.1}} = (81)^{\frac{1}{n_H}} \quad (149)$$

Here $S_{0.9}$ and $S_{0.1}$ are the [synKin]/[synPhos] values required to respectively achieve 90% and 10% of the maximal response and n_H is the effective Hill coefficient value. EC_{50} values for [synKin]/[synPhos] can be inferred from the midpoint between $S_{0.9}$ and $S_{0.1}$.

Applying this analysis to the phosphorylation cycle in **Fig. 1D**, we observed n_H values of ~1 for synPhos, weak synPhos, and synPhos dead cases, with the EC_{50} value decreasing with lower synPhos activity (**fig. S14A**). Thus, our default configuration, which is used in **Figure 3** in the sensor circuit, operates in a linear regime. We extended this analysis to the complete design space shown in **Fig. 1F**, plotting EC_{50} and n_H values along with the maximum phosphorylation level (**fig. S14B**). While most part compositions were approximately linear ($n_H \sim 1$), we identified several that produced more sensitive compositions that exhibited a n_H approaching 2, as well as compositions with higher EC_{50} values. More sensitive compositions generally had stronger synKin LZ affinity (low K_{WS}) paired with weaker synPhos LZ (high K_{ES}), while those with high EC_{50} values showed the opposite trend. Part usage and predicted dose-response curves for compositions in these regions are shown in **fig. S14B**. Finally, we use the model to identify regions of parameter space outside of our part set that could lead to even sharper responses. We performed analysis for n_H across a larger 2D parameter surface, simultaneously modulating synKin LZ affinity (K_{WS}) and activity ($\tilde{k}^p_{WS}$) while holding synPhos LZ affinity (K_{ES}) and activity ($\tilde{k}^u_{ES}$) constant at values

obtained from the **Fig. 1D** synPhos cycle. n_H values were computed across these surfaces at three different substrate concentrations: 1) the default synSub expression level; 2) a 100x lower synSub, and 3) a 100x higher synSub concentration to that observed (**fig. S14C**, top). The same analysis was performed with varied the synPhos LZ affinity (K_{ES}) and strength ($\tilde{k}^{p}_{ES}$) while holding synKin affinity and activity constant at the values obtained from the phosphorylation cycle configuration in **Fig. 1D** (**fig. S14C**, bottom). Consistent with the results from **fig. S14B**, this analysis predicts that an ultrasensitive n_H may be best achieved by further tuning K_{WS} down, keeping K_{ES} high, and expressing high synSub relative to synKin and synPhos. In summary, while our part regime does allow some degree of ultrasensitivity, highly switch-like compositions will likely require new, higher affinity domain parts.

Parts for engineering phosphorylation cycle network connections

With abilities to construct and predictively tune cycle phosphorylation levels in hand, we next developed an approach that used phosphorylation-dependent protein-protein interactions to connect phosphorylation cycles together into networks (**Fig. 2A**). Here, we turned to tSH2s, which are the native binding partner for phosphorylated ITAMs and ITIMs in immune cells (*38*). To identify tSH2/pY motif pairs that are compatible with the synKins that we developed in **Fig. 1**, we established a 'two-hybrid' style mCherry transcriptional reporter assay (**fig. S15A**). We designed the reporter by fusing a synthetic zinc finger transcription factor (synTF) (*7*) and LZ domain to potential synKin-phosphorylatable motifs (bait), and the tripartite activator VP64-p65-Rta (VPR) (*111*) to potential tSH2 binders (prey). By co-expressing synKin with the synTF, it was possible to identify tSH2/pY motif pairs that showed synKin phosphorylation-dependent interactions. As an initial demonstration of recruitment-driven transcriptional activation in our system, we fused an LZ-R to the synTF and co-expressed with a VPR activator fused to LZ-E, demonstrating that this cognate LZ interaction is able to strongly activate mCherry reporter expression (**fig. S15B)**.

To screen for interaction pairs, we co-expressed a synKin ($ABL_{228\text{-}540\ FF}$) with a synTF fused to variety of human derived ITAM and ITIM motifs (**fig. S15C**) (*93*), including six ITAMs from the TCR ($CD3Z_{64\text{-}95}$, $CD3Z_{105\text{-}136}$, $CD3Z_{131\text{-}164}$, $CD3\delta_{141\text{-}171}$, $CD3\gamma_{163\text{-}182}$, $CD3\varepsilon_{180\text{-}207}$), two from BCR ($IgA_{181\text{-}211}$, $IgB_{188\text{-}221}$), one from FcRγ ($Fc\varepsilon R1\gamma_{56\text{-}86}$), one from PDGFR ($PDGFRB_{731\text{-}757}$), and the ITIM from SHPS-1 ($SHPS\text{-}1_{424\text{-}459}$) (**fig. S15D**). We also expressed VPR fused to tSH2 domains, including $ZAP70_{2\text{-}259}$, $Syk_{15\text{-}263}$, $SHP1_{4\text{-}232}$, $SHP2_{6\text{-}216}$, and $p85a_{333\text{-}724}$. Testing these constructs with the assay demonstrated that TCR-derived ITAMs have similar tSH2 binding specificity, showing phospho-dependent interactions with ZAP70- and Syk-derived tSH2s, while IgA, IgB and FcRγ showed binding to the ZAP70 tSH2 and limited binding to the p85a tSH2. PDGFR showed exclusive binding to the p85 and SHPS-1 only bound SHP2, with neither binding to ZAP70. We also constructed a synthetic tSH2 that could act as a phospho-dependent binder for the $SLP76_{108\text{-}154}$ by fusing the SH2s from Vav1 and ITK together (*112*) (**fig. S16A**). Since both proteins bind natively to the SLP76 at nearby pY residues (Vav1 binds Y128, ITK binds Y145) we reasoned that we could create a higher affinity interaction by fusing the domains together. As our data show, this fusion protein demonstrated phospho-dependent interaction with SLP76, with a 2x tandem repeat of the two-SH2 fusion demonstrating particularly strong activation (**fig. S16B**). Also, the ZAP70-derived SH2 was unable to bind to the SLP76 motif to activate transcription. In summary, while the specificities for the set the tSH2s that we tested demonstrated limited overall orthogonality, we were able to identify PDGFR/p85 and SLP76/Vav1-ITK as pY motif/SH2 pairs with orthogonality to the CD3Z/ZAP70 pair.

Making connections between two phosphorylation cycles

In order to use the tSH2/pY motif pairs we identified in **figs. S15** and **S16** to engineer network connections between two synthetic phosphorylation cycles, we utilized a scheme where phosphorylation of the upstream cycle establishes a phospho-dependent interaction that drives phosphorylation of the downstream cycle (**Fig. 2A**). To enable this scheme, we engineered a

phospho-couple (PC)—a protein that functions as both the substrate in the upstream phosphorylation cycle and the kinase in the second—by fusing the $ZAP70_{326\text{-}619\ FF}$ kinase domain to the N-terminus of a $CD3Z_{131\text{-}164}$-derived synSub containing three motif repeats (**fig. S17A**). After recruiting an upstream synKin via an LZ interaction, the PC is phosphorylated and can subsequently recruit a second substrate protein consisting of a ZAP70 $tSH2_{2\text{-}259}$ fused to the $SLP76_{108\text{-}154}$, which is in turn phosphorylated by the $ZAP70_{326\text{-}619\ FF}$ domain in the PC. In order for the signal to pass from the first cycle to the second as a function of upstream synKin activity, it was necessary to minimize cis-phosphorylation within the PC, which we hypothesized could be accomplished by introducing a rigid linker domain between the substrate motif and kinase domain, thereby sterically restricting their interaction (**fig. S17A**). We identified engineered proline-rich linkers, GlySer-polyPro-β2m-polyPro (GPbP) and GS-polyPro-ZAG-polyPro (GPZP) (*113*) as potential sterically-limiting linker elements and inserted them into the PC. We tested their ability to diminish cis-phosphorylation in an experiment with a system of three genes: and upstream synKin derived from $ABL_{228\text{-}540\ FF}$, along with the PC and the tSH2-pY fusion proteins shown in **fig. S17A** (**fig. S17B**). We found the GPZP linker showed the best suppression of basal cis phosphorylation, while still allowing high levels of synKin-dependent phosphorylation of both up- and downstream substrates (**fig. S17C**). This composition was used to construct the two-step circuits featured in **Fig. 2B**.

Two-step phosphorylation cycle circuit fitting and prediction

To fit two-step circuit data, we used a similar approach as for the single phosphorylation cycle in **Fig. 1E**. All the biophysical parameters that were fit in the model are shown in **fig. S18A**. We fit the data shown in **Fig. 2B**, with the exception of the monovalent composition, as well as 2 compositions containing additional synKin activity variants (**fig. S18B**). During fitting, we made the simplifying assumption that the catalytic turnover rates ($\tilde{k}_{WS1}$, $\tilde{k}_{ES1}$) for a synSub harboring three motifs was processive, and similar to that of one motif. As before we used D_{KS} to show fit

quality, which was comparable to that obtained for the single cycle in **Fig. 1E** (**fig. S18B**). These data allowed fitting of all part-specific parameters shown in **fig. S18C**. When combined with parameters obtained in **fig. S12** (medium and weak K_{WS1}, medium and weak $\tilde{k}_{S1S2}$), we could predict the behavior space shown in **Fig. 2C.** Part-specific parameters that the two circuits had in common show excellent agreement, including the strong LZ affinity (single: <546, two-step:17 to 289). WT ZAP70$_{326\text{-}619}$ $\tilde{k}_{WS}$ was slightly lower, but in a similar range as in the single cycle (single: 2.5 to 3.3, two-step: 0.66 to 0.81), while WT PTPN1$_{1\text{-}319}$ $\tilde{k}_{ES}$ was similar (single: 5.6 to 11, two-step: 6.09 to 8.05). Fitted AU values were converted to K_d values as in **fig. S12**, and both the strong LZ and the SH2 binding affinity obtained from the fit were similar to *in vitro* K_d values measured by surface plasmon resonance binding experiments (*114*). In summary, these results offer further demonstration that our modeling approach is able to extract values for part component behavior that are biophysically plausible and consistent with values measured in the literature, offering evidence that the modularity of our parts extends to both single and two-step circuit contexts.

We next generated behavior predictions for the entire two-step circuit parameter space, which totaled 3,456 compositions (**fig. S19A**). As before, for combinations that did not involve adjusting expression levels of the circuit components, we generated predictions using the profile from the default composition shown in **Fig. 2B** (multivalent, upper right) and then predicted phosphorylation levels for both substrates by permuting model-fitted parameters. For predictions with adjusted component expression, we generated separate profiles for pairwise combinations of each expression level variant ([low and high synKin] • [low and high PC] • [low and high synPhos] • [low and high synSub] = 16 total profiles). For background phosphorylation predictions, we set the expression level for synKin to 0 and reran predictions for all the compositions.

After predicting up- and downstream phosphorylation for each composition, we plotted downstream substrate phosphorylation in the presence and absence of synKin to depict a 2D

fold-change (with vs. without upstream synKin) behavior space: phosphorylation of the second substrate in the absence of the upstream synKin compared to phosphorylation with the synKin (**Fig. 2C** and **fig. S19B**). In analyzing this space, our goal was to identify compositions that show high fold-change (upper-left corner), as well high stoichiometric activation (top). To interrogate the part composition of different behavior regimes, we subdivided the scatter plot into six regions based on low, medium, and high fold change that were subdivided based on low and high activation (**fig. S19B**). The high fold-change, high activation region showed an enrichment of strong synKin and PC activity, strong affinity between synKin and PC, and high expression of the second substrate. Interestingly, high usage for strong phosphatase and low expression for the middle substrate were also utilized—part combinations that are likely to contribute to the low background phosphorylation and stoichiometric amplification. We used this analysis to inform our choices for optimal construction of high-gain variants that were experimentally validated in **Figure 2C**, and were also used for selecting the amplification module design in the sense-and-respond circuits described in **Fig. 4**.

Phospho-sensor circuit design

We next used our part toolkit to engineer circuits that could sense extracellular signal and convert it into changes in phosphorylation cycle equilibrium (**Fig. 3A**)**.** To facilitate the coupling of extracellular ligand binding to phosphorylation cycle phosphorylation, we used a well-known chemical dimerization domain pair: the FK506 binding protein (FKBP) and K2095P mutant of the FKBP-rapamycin binding (FRB*) protein (*115*) (**fig. S20A**). These proteins heterodimerize in the presence of the rapamycin analog AP21967, which binds with a lower affinity than rapamycin and is not a potent inhibitor of mTOR (*116*). On the extracellular side, we fused FKBP and FRB* to the transmembrane domain from CD28 via flexible GS linkers. On the cytoplasmic side, we also appended LZ and the $ABL_{228\text{-}540\ FF}$ kinase domain with intervening GS linkers. Both receptor

chains had N-terminal signal peptides from IgGλ (*117*), and the FRB*-kinase chain had a 1x FLAG epitope.

To optimize receptor performance, we tuned the interdomain linker length and TM motif sequence, both of which have been shown to play significant roles in synthetic receptor function (*118-120*). We tested various linker lengths between the dimerization domains and the TM, as well as between the TM and the kinase and LZ domains (**figs. S20B-D**). We determined that a 10x GS-TM-10x GS composition for the FKBP-LZ chain and 10x GS-TM-5x GS for the FRB*-kinase chain produced the highest fold change in phosphorylation upon ligand binding. Further refinement in fold-change performance was achieved by optimizing receptor TMs using this linker composition. Within the TM, residues W154 and W179 have been shown to promote CD28-TM homodimerization, while C165 can form a disulfide bond between monomers, and Y166, S167, and T171 form hydrogen bonds (*121*). To test whether mutating these residues could lower ligand-independent phosphorylation due to spontaneous dimerization, we introduced mutation sets M3 (W154L and W179L) and M4 (C165L, Y166L, S167L, and T171L) into each receptor chain and tested combinations of the sets with each other with the WT TM (**fig. S20D**). Our results identified the combination of the M3 TM for the FKBP-LZ chain and the WT TM set for the FRB*-kinase chain as having the highest fold change activation. With these optimized synthetic receptor designs in hand, we rigorously validated that the activation of the phospho-sensor circuit is ligand-inducible and recruitment-dependent by abrogating circuit function with either a non-binding receptor FRB* (L2098T, W2101F) (*116*) or a non-cognate LZ (**Fig. 3B**).

We measured dose responses for the synPhos-containing sensor circuit, which was fit to the following Hill equation (code description in **Table S3**):

$$fluor = \left(\frac{a \cdot [ligand]^{n_H}}{EC_{50} + [ligand]^{n_H}}\right) + c \quad (150)$$

where *fluor* is the mean pY fluorescence from the HHH analysis, EC_{50} is the AP21967 (or TNF-α) concentration at which fluorescence is half-maximal, n_H is the Hill coefficient, *a* is the maximum activation level, and *c* is basal fluorescence signal.

Using a condensate colocalization reporter to measure phosphorylation sensor circuit dynamics.

In order to measure the dynamics of activation for our ligand-activated phospho-sensor circuit, we aimed to create a reporter that would allow us to use time-lapse fluorescence imaging to detect the accumulation of a phosphorylated synSub tagged with a fluorescent protein (**Fig. 3C** and **fig. S21**). To design a reporter that enables both rapid signal detection and observation of reversibility when upon pathway deactivation, we considered several options that leveraged the ability of our SH2 domains to specify phospho-dependent binding. While split fluorescent protein reporters have been frequently used to detect protein-protein interactions (*122*), including those that are phospho-dependent (*123*), they were ruled out due to their irreversibility and the extended maturation time required for observing a fluorescent signal. FRET reporters offer another potential solution, but are difficult to engineer and optimize to achieve strong signal (*124, 125*). Another option is subcellular localization-based reporters, which rely on recruitment or trafficking of a phosphorylated species to the cell membrane or nucleus (*126*). However, using these reporters for our system is challenged by the fact that a membrane-localized reporter could potentially report on receptor-bound synSub in addition to phosphorylated synSub. Also, there are no know molecular mechanism that could easily be used to convert Y phosphorylation into nuclear translocation. We reasoned that the expression of proteins capable of forming ectopic liquid-liquid phase condensates (LLPCs) could offer an alternative 'cytoplasmic subcompartment' for co-localization of phosphorylated synSub (*61, 127*). For this purpose, we chose a recently characterized bacterially-derived condensate-forming protein PopZ (*128*), and demonstrated that

a truncated version ($PopZ_{24\text{-}177}$) can be fused to mCherry to spontaneously form visible cytoplasmic condensates when expressed in HEK293T cells (**figs. S21A**).

To make PopZ-mCherry into a reporter for our phospho-sensor circuit, we fused it to ZAP70 $tSH2_{2\text{-}254}$. We also replaced GST in the synSub (**fig. S4**) with EGFP (**fig. S21A**). This composition allows phosphorylated synSub to be recruited to pre-formed PopZ-mCherry condensates upon phosphorylation, resulting in red and green colocalization. We developed an image processing pipeline (see **Materials and Methods** for details, illustrated in **fig. S21B**) that determines the fraction of condensate-recruited EGFP at the single-cell level. We used this approach to track circuit activation following AP21967 addition (t=0), and observe circuit deactivation after addition of the ABL kinase inhibitor imatinib mesylate (**Fig. 3C, movies S1** and **S2**). Additionally, we demonstrated that reporter co-localization is both circuit- and phosphorylation-dependent by showing that a non-ligand binding receptor and non-binding SH2 alleles both abrogate EGFP co-localization (**fig. S21C**). In addition to monitoring condensate co-localization, we also performed phospho-flow on our reporter circuit 30 mins after ligand addition (**fig. S21D**), demonstrating similar maximum phosphorylation signal generated between the colocalization reporter and the non-reporter circuit in **Fig. 3B**.

To verify the role of synPhos-mediated dephosphorylation in causing de-localization, we also measured the off kinetics of a circuit with synPhos absent and showed that de-localization no longer occurs upon addition of the ABL inhibitor (**fig. S22A**). Obtaining these data allowed us to quantitate circuit activation and deactivation dynamics by formulating an ordinary differential equation model (**fig. S22B**). Receptor dimerization was modeled with the following equation:

$$\frac{d[Receptor_{dim}]}{dt} = k_c \cdot (1 - [Receptor]) \tag{151}$$

where k_c is the rate constant for receptor dimerization upon binding the ligand (held constant here), while the normalized EGFP condensate ratio $[GFP_{conden.}]$ was denoted by the following equation:

$$\frac{d[GFP_{conden.}]}{dt} = k_k \cdot [Receptor_{dim}] - (k_p + k_p^{bg}) \cdot [GFP_{conden.}] + k_k^{bg} \quad (152)$$

Here k_k is a composite rate representing phosphorylation of synSub and its subsequent diffusion into the condensates, while k_p represents synPhos-dependent dissociation and diffusion out of the condensate. k_p^{bg} is the background phosphatase activity.

We used the above equations to perform parametric fitting of the activation and deactivation time course data from **Fig. 3C** and **fig. S22A** to obtain rate constants for the system (**fig. S22B**), which were similar to those obtained for kinase activity from the thermodynamic model (**fig. S12, Fig. 2C**) after values were normalized by the background phosphatase rate measured in **fig. S22A**. We compared the timescale of activation observed for our synthetic circuit with that of localization reporters for various native pathways, including EGFR/ERK (*129*), RTK/JAK-STAT (*43*), TGF-β/SMAD (*44*), and WNT/β-catenin (*130*) (**fig. S22C**). While ERK activation by EGFR occurs the fastest, our system showed similar dynamics to RTK/JAK-STAT and TGF-β/SMAD pathways. One potential explanation for this is that while our system, as well as RTK and TGF-β signaling pathways, require that receptors dimerize upon ligand binding (*131*), the EGFR receptor is poised to activate more quickly because it is already organized as a dimer prior to ligand binding. The WNT/β-catenin pathway is activated on a much slower time scale than the other pathways, possibly due to the requirement for cytoplasmic accumulation of β-catenin (*132*). Overall, these results demonstrate that we can use our design scheme to build synthetic phosphorylation pathways with dynamic behavior that is comparable to native pathways.

Constructing a synthetic pathway connecting receptor input to transcriptional output.

In native phosphorylation signaling pathways, propagation of a signal originating at the cell membrane may require stoichiometric amplification through multiple signaling steps to create the chemical potential necessary to travel across and between subcellular compartments. To engineer a signaling pathway that could facilitate efficient transmission of an extracellular signal to transcriptional machinery in the nucleus, we combined our two-step amplifier (**Fig. 2**) and phospho-sensor (**Fig. 3**) modules (**Fig. 4A**). We coupled amplifier output to transcriptional activation using the engineered Vav1-ITK SH2 described in **fig. S16**, and a phospho-activated synTF module similar to the one depicted in **fig. S15** (**fig. S23A**). Here the SH2 is fused to VPR (*111*), which drives EGFP expression upon phosphorylation of a 3x SLP76-dervied pY motif that is fused to the synTF. To couple the amplifier and phospho-sensor modules, we programmed the PC to serve as the substrate for receptor-activated phosphorylation. Since the synTF, which is the substrate for the second cycle, is permanently localized to the nucleus (it contains an NLS), pathway signaling requires that the PC be phosphorylated at the plasma membrane, and then imported to the nucleus to activate transcription. While at ~79 kDa, the PC may be able to diffuse passively between the cytoplasm and nucleus in HEK293T cells (*133*), this rate is likely to be slow, with the majority of PC partitioning to the cytoplasm. Therefore, we sought to improve pathway performance by tagging the PC with an NLS and NES to enhance its nuclear import and export rates. In a test circuit that lacked EGFP reporter SH2-VPR genes, we found that tagging the PC with only NLS or NES resulted in limited phosphorylation of the synTF or PC, respectively (**fig. S23B**). By comparison, incorporating both NLS and NES showed the best overall phosphorylation level as well as EGFP reporter expression following ligand addition (**Fig. 4A**, left).

To demonstrate that the part composition we chose for the sense-and-respond circuit was optimized for circuit activation, we tested a number of other amplifier module designs, including the other high-gain compositions from **Fig. 2C** that were predicted to show >10x fold-change in activation, as well as a set of circuits from the <10x fold-change region. Consistent with our model, composition #1 demonstrated high fold-change in transcriptional reporter activity, but low

activation, while composition #2 and #3 showed the best overall performance. Thus, we chose composition #2 for sense-and-respond circuit construction. Other compositions exhibited weak ligand-dependent output, underscoring the pivotal role of amplification as a critical design feature (**fig. S24**). These results demonstrate that design principles derived from our model-guided analysis of the two-step amplifier circuit could be applied to sense-and-respond circuit construction to select performance-optimized compositions. We measured a dose response curve for our sense-and-respond circuit (**fig. S24B**), fitting data to Eq. 150. We found that this circuit was also highly linear (n_H=0.97), with an EC_{50} of 3.75 nM.

Engineering new receptor inputs

To further demonstrate the configurability of our system, we sought to expand its sensing capabilities by engineering receptors capable of detecting new extracellular ligands. We hypothesized that the structure of our receptors would permit us to modify sensing specificity by swapping the extracellular dimerization domain. We identified an scFv (*134*) that binds specifically to the cytokine TNF-α, which exists as a multimer (*135*), and fused it to both receptor chains, replacing the FKBP and FRB* domains used for the sensor circuit in **Figure 3** (**fig. S25A**). This enabled the phospho-sensor circuit to activate in the presence of TNF-α (**Fig. 4B)**, demonstrating a nearly 6-fold induction in synSub phosphorylation upon treatment with 20 ng/mL TNF-α (**fig. S25B**). We measured a dose response curve for our TNF-α sense-and-response circuit, fitting data to equation 150. We found that this sensor circuit, like the one measured in **Figure 3B**, was highly linear (n_H=1.07), with an EC_{50} (6.14 ng/mL) similar to reported scFv interaction affinity (*134*).

Engineering and testing a closed-loop therapeutic control circuit

Next, we asked whether our framework could be used to engineer a circuit programmed to sense markers associated with inflammation and respond via secretion of a therapeutic factor. Because TNF-α is broadly involved in inflammation and is a marker for numerous inflammatory

disorders, we elected to use TNF-α as the circuit's input. To create a circuit that responds with an anti-inflammatory output, we selected the cytokine IL-10 due to its well-documented immunosuppressive properties, including the inhibition of CD28-costimulated T cell activation, proliferation, and cytokine production under inflammatory conditions (*136-139*). Such a TNF-α sensing/IL-10 response circuit offers an excellent test-case for our system. For the past two decades, numerous studies and preclinical trials have been conducted using IL-10 to treat a variety of inflammatory disorders, including inflammatory bowel disease (*140, 141*), and psoriasis (*142*). However, clinical trials have generally failed to significantly improve patient outcomes (*143, 144*), which is likely due to an inability to achieve sufficiently high local concentrations of IL-10 following systemic infusion (*145*). On the other hand, high systematic levels of IL-10 can lead to toxicity involving excessive B cell activation and antibody production (*146*), a mechanism that plays a significant role in systemic lupus erythematosus (SLE) pathology (*147*). Furthermore, the immunosuppressive effect of IL-10 can lead to chronic viral infection without timely clearance (*148*). As a way to potentially mitigate these toxic effects, our goal was to develop a circuit that responds to TNF-α by proportional secretion of IL-10, thereby inhibiting T cell activation and TNF-α production and rapidly establishing a low setpoint for both cytokines (**Fig. 4C**, left).

Building upon the design of the optimized sense-and-respond circuit composition from **Fig. 4A**, we coupled our TNF-α sensor circuit to our sense-and-respond circuit and placed the expression of IL-10 under control of the synTF cassette. To demonstrate circuit function, we used a transwell system to co-culture CD3/CD28-activated human PBMCs with HEK293T cells transfected with the circuit for 60 h (**Fig. 4C**, bottom left). We sampled TNF-α and IL-10 secretion from the culture every 12 h, and assayed T cell proliferation (**figs. S26A** and **B**) and IFN-γ secretion (**fig. S26C**) at the end of the time course. In the coculture containing activated T cells and HEK293T cells with no circuit, we observed rapid TNF-α accumulation and robust T cell proliferation (**Fig. 4C**, top right). In the open-loop circuit (**Fig. 4C**, top right), which is configured with a synKin (no receptors) that constitutively activates a two-step circuit driving IL-10

expression, we observed continuous accumulation of IL-10 as well as substantial inhibition of TNF-α production and T cell proliferation. In contrast to the open-loop composition, the closed-loop circuit could dynamically sense TNF-α levels and adjust IL-10 production down early in the time course, but still suppressed T cell proliferation and reduced IFN-γ secretion (**Fig. 4C** bottom right, **fig. S26C**). As a demonstration that sustained circuit activity was responsible for the low setpoint of TNF-α and IL-10, we added imatinib mesylate (10 μM) midway through the time course at 36 h. We observed a ~40% drop in IL-10 and 2-fold increase for TNF-α and IFN-γ secretion compared to the uninhibited circuit, indicating that secreted cytokine suppression is driven by continuous circuit activity throughout the time course and is not an artifact of initial culture conditions (**fig. S26C**).

To develop a more complete understanding of the role that the closed-loop circuit plays in determining TNF-α and IL-10 coculture dynamics, we extended the kinetic model in **fig. S22** to incorporate cytokine production and degradation (**fig. S27**). We modeled the dynamics of each of the co-cultured circuits shown in **Fig. 4B**. The empty cell co-culture was modeled using the following equation:

$$\frac{d[TNF-\alpha]}{dt} = k^{+}_{TNF-\alpha} - k^{-}_{TNF-\alpha} \bullet [TNF-\alpha] \tag{153}$$

Where $[TNF-\alpha]$ represents the concentration of the cytokine in the media, as measured by ELISA. $k^{+}_{TNF-\alpha}$ is the production rate of the TNF-α by activated T-cells, which is assumed to be continuous over the course of the experiment, and $k^{-}_{TNF-\alpha}$ is the TNF-α degradation rate in media. The open-loop circuit was represented by the following equations:

$$\frac{d[Active]}{dt} = k_k + k_k^{bg} - \left(k_p + k_p^{bg}\right) \bullet [Active] \tag{154}$$

$$\frac{d[IL-10]}{dt} = k^{+}_{IL-10} - k^{-}_{IL-10} \bullet [IL-10] \tag{155}$$

$$\frac{d[TNF-\alpha]}{dt} = k_{TNF-\alpha}^{basal} + \frac{k_{TNF-\alpha}^{+} - k_{TNF-\alpha}^{basal}}{1+\left[\frac{[IL-10]}{K_{int}}\right]} - k_{TNF-\alpha}^{-} \bullet [TNF-\alpha] \quad (156)$$

Where $[Active]$ represents the proportion of circuit activated HEK293T cells, and k_k and k_p represent the activation and deactivation rates for the signaling circuit response measured in **fig. S22**, while k_k^{bg} and k_p^{bg} represent corresponding background activation and deactivation rates. k_{IL-10}^{+} and k_{IL-10}^{-} are the production and degradation of IL-10, while K_{int} represents the half-maximal inhibitory concentration of IL-10 for TNF-α production and $k_{TNF-\alpha}^{basal}$ is the basal production rate at saturating IL-10 levels. The closed-loop circuit was represented by the following:

$$\frac{d[Active]}{dt} = k_k \bullet \frac{[TNF-\alpha]}{[TNF-\alpha] + K_{TNF-\alpha}} + k_k^{bg} - \left(k_p + k_p^{bg}\right) \bullet [Active] \quad (157)$$

$$\frac{d[IL-10]}{dt} = k_{IL-10}^{+} - k_{IL-10}^{-} \bullet [IL-10] \quad (158)$$

$$\frac{d[TNF-\alpha]}{dt} = k_{TNF-\alpha}^{basal} + \frac{k_{TNF-\alpha}^{+} - k_{TNF-\alpha}^{basal}}{1+\left[\frac{[IL-10]}{K_{int}}\right]} - k_{TNF-\alpha}^{-} \bullet [TNF-\alpha] \quad (159)$$

Where $K_{TNF-\alpha}$ is the half-maximal concentration at which TNF-α activates the signaling circuit.

Using these equations, we carried out a global fit to extract parameters for rates of cytokine production and degradation (**fig. S27**, bottom). During the fit, we constrained $K_{TNF-\alpha}$ by 2-fold according to the value extracted from the fit in **figure S25C** (6.14 ng/mL). We then used the parameterized equations to simulate cytokine dynamics for systems harboring hypothetical synthetic circuits with slower characteristic response timescales, testing whether the circuits could maintain low setpoint levels for both cytokines as efficiently as our phosphorylation-based circuit

(**fig. S28**). We included circuits actuated by transcription factor production or proteolysis, both of which have slower rates of activation (k_k), as well as much slower rates of inactivation (k_p) that are effectively limited by protein turnover. In our simulations, we observed a larger initial TNF-α pulse for these circuits, likely due to slower onset of IL-10 secretion (**fig. S28A**). We also observed an inability to maintain a low setpoint for IL-10. We also examined cytokine profiles simulated for proteolysis (*50*) and transcriptional (*149*) circuits using k_k, and k_p values inferred from circuit activation/deactivation profiles reported in the literature (**fig. S28B**). We found that both classes performed differently than a circuit that our phosphorylation, with the transcriptional circuit unable to maintain tight control of TNF-α, and both circuits unable to keep IL-10 low after reaching their respective steady states. These results argue that the relatively fast characteristic timescale that our phospho-circuit operates at is important for maintaining low setpoints for both cytokines.

Testing synthetic signaling circuit translatability

As a final set of experimental demonstrations, we sought to assess the potential translatability of our synthetic phospho-signaling components. One reason we selected protein domain parts derived from human cell signaling pathways was to mitigate potential immunogenicity associated with deploying the circuits in an adoptive cell therapy setting. We analyzed all the protein components from the sense-and-respond circuit in **Fig. 4C** using T Cell Class I pMHC Immunogenicity Tool, an established immunogenicity prediction tool (*150*) used to predict the relative chance a peptide/MHC complex will elicit an immune response. We compared our signaling components to several widely used synthetic receptors (*151, 152*), protease parts used for engineering post-translational circuits (*153*), chimeric antigen receptors (*154*), and FDA-approved fully humanized monoclonal antibodies (mAbs) (*155*) as references (**Fig. S29**). We evaluated the immunogenicity scores of all 9-mer peptide sequences within the six engineered proteins in the cytokine control circuit, along with the synthetic receptors, proteases and mAbs and set a cutoff threshold value of 0.328 as the mean + 2xSD of the immunogenicity scores for

all the peptides in the three chosen FDA-approved mAbs. Proteins with a percentage of peptides scoring higher than 0.328 are more likely to be more immunogenic compared to these mAbs. While certain regions of our synthetic proteins (e.g., the TM domains), showed high predicted immunogenicity, our phosphorylation circuit components had average scores that were similar to the other parts. It should be possible to further de-immunize our part set using a combination of computational analysis and functional testing, thereby improving the safety profile of cell therapy products engineered using our proteins (*152*). This should be aided by the modularity of our design scheme set, which allows us to swap out highly immunogenic parts for less reactive parts that retain similar biophysical properties (e.g., new protein-protein interaction domains that bind with equivalent, tunable affinity). We also tested our circuits for their ability to function in therapeutically relevant cell types. We introduced circuits into human umbilical-cord-derived mesenchymal stem cells (hUC-MSCs) (*156*), which have been historically one of the most frequently investigated therapeutic cell types, and ARPE-19 cells (*157*), which have been approved for clinical trials involving *in vivo* therapeutic production (*4*). Our phospho-sensor circuit ported well into both cell types, yielding 9.7x and 6.0x fold-change inductions in response to AP21967 as assayed by flow cytometry (**fig. S30A**). We also tested the sense and respond circuit in ARPE-19 cells and showed that the full pathway response works, exhibiting a 7.3x fold-change induction (**fig. S30B**). These results demonstrate that, with little optimization, our synthetic signaling circuits can function in cell types that can be translated to clinical settings.

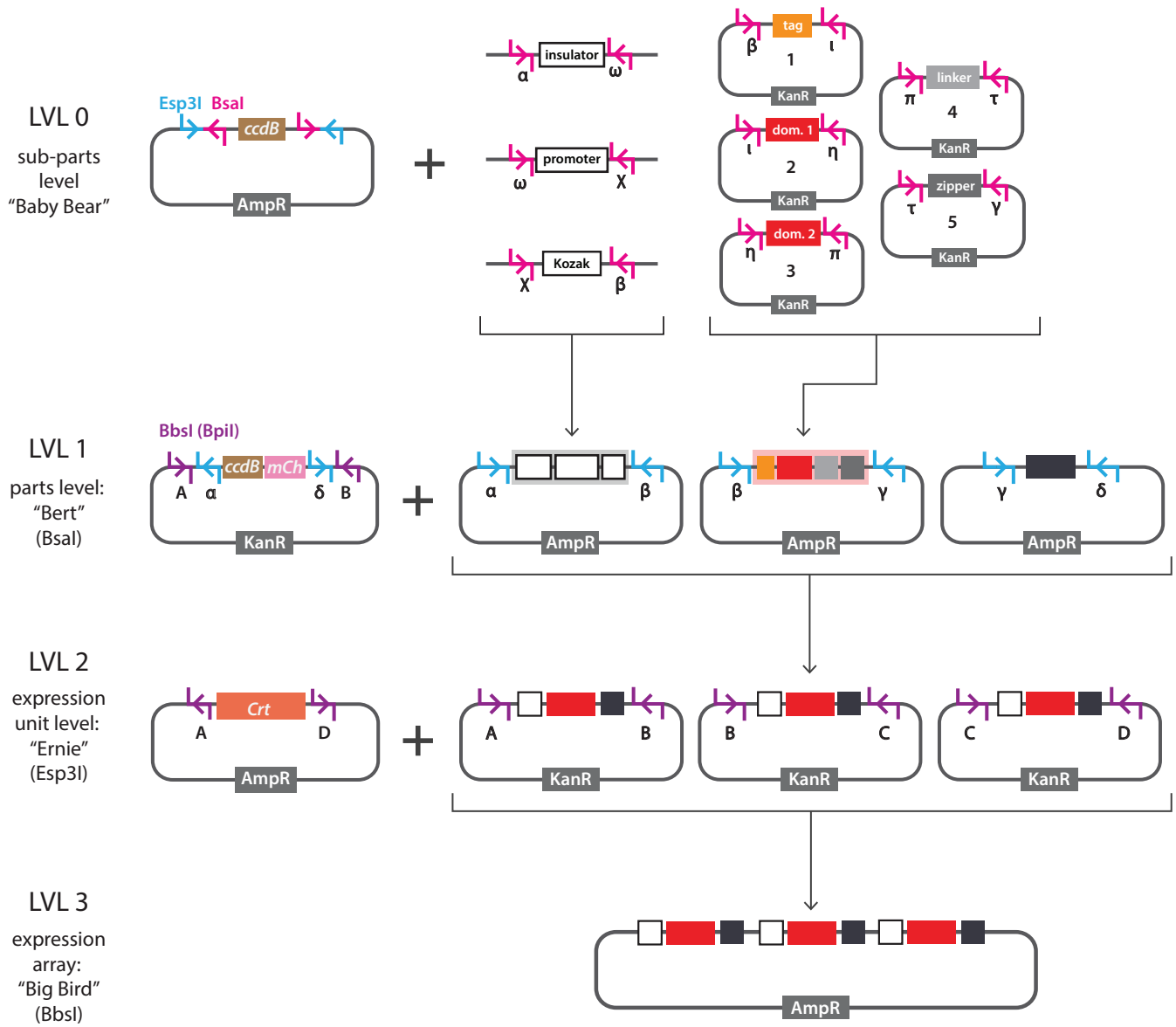

Figure S1. Cloning workflow used in this study. Multi-level hierarchical cloning workflow for constructing the plasmids described in **Table S1**. For level 1 assemblies, PCR-amplification of DNA fragments or plasmids containing "sub-parts" (e.g., protein domains or promoter fragments) were used as inputs for assembly into ccdB-containing, AmpR entry vectors using BsaI (pink) to generate plasmids containing a promoter, open reading frame (ORF), or terminator. For Level 2 assemblies, EUs were constructed by assembling promoter, ORF, and terminator part plasmids into a KanR destination vector containing a dual ccdB-mCherry2 expression cassette using Esp3I (blue). In the final level 3 assemblies, EUs are combined into a destination vector containing an AmpR marker. This occurs via BbsI-mediated assembly (purple) to replace a Crt operon marker, resulting in multi-EU arrays where genes are ordered based on level 2 entry vector overhangs. Lower-case Greek and upper-case Roman letters represent different overhangs for type IIS assembly. Arrows on the vectors show the orientations of type IIS cutting.

A

KINETIC CONSTANTS FOR SIGNALING KINASES

		k_{cat} (s^{-1})	K_m (μM)	references
pS/T	CDK	5.7	6	*80*
	GSK	20-30	300-500	*81*
	PKA	10-30	5.4	*82*
pY	EGFR	0.1-0.4	200-1000	*83, 85*
	Zap70	0.5-3	50-1500	*85, 86*
	ABL	0.25-3	50-200	*87, 88*

B

TCR PATHWAY ACTIVATION

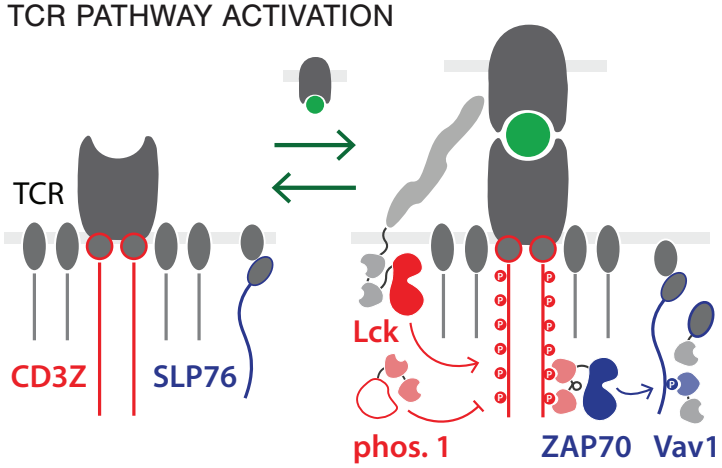

C

DOMAIN PARTS

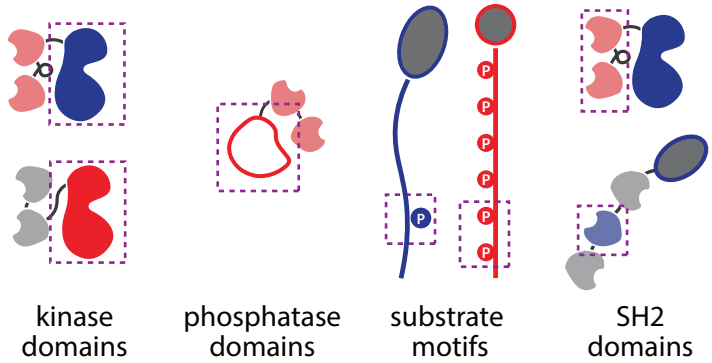

Figure S2. Native pathways as sources of synthetic signaling circuit parts. (a) Kinetic constants for various pS/T and pY kinases involved in signal transduction as measured *in vitro* against peptide substrates. **(b)** During TCR signaling, the Y residues of TCR ITAMs are phosphorylated after Y kinases (Lck, ZAP70) are physically recruited to the complex. The Y phosphatases are also recruited to the complex to dephosphorylate the pYs. The pYs can then serve as docking sites for specific tandem SH2 domains, mediating downstream signal transduction, which includes phosphorylation of the scaffold protein SLP76. **(c)** The component properties of the domains comprising native signaling pathway proteins allow them to be appropriated and modifed to create parts for constructing synthetic phosphorylation cycles.

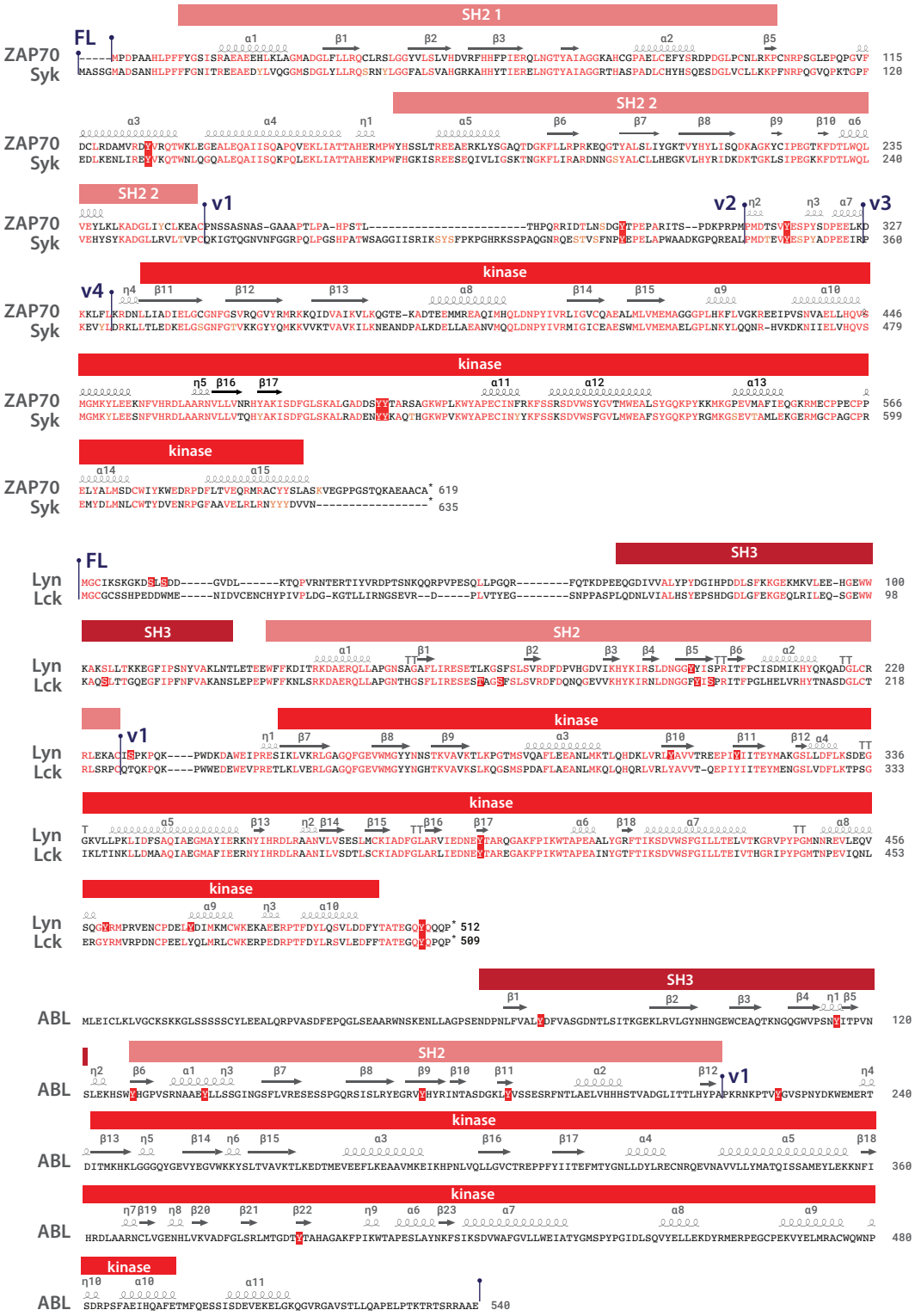

Figure S3. Native tyrosine kinase sequence alignments. Amino acid sequences and 2° structure elements for all kinases tested in this study. ZAP70 and Syk are aligned with each other. Src family kinases (Lyn and Lck) are also aligned. ABL is shown separately. Red boxes indicate predicted domain boundaries for SH2, SH3, and kinase domains (Uniprot predictions). 2° structure features (α-helix and β-strand) are also indicated. Purple lollipops indicate boundaries for tested truncation variants. Highlighted Ys indicate known phosphorylation sites.

SYNTHETIC SIGNALING PROTEIN DESIGN: synKin & synSub

Figure S4. Synthetic kinase and substrate designs. Amino acid sequences of the synKin and synSub pair featured in **Figure 1B** and available part variants. The synKin contains a 3x FLAG epitope tag on the N terminus, an engineered pY kinase domain, a flexible 10x GS repeat linker, and an acidic leucine zipper (LZ-E) on the C terminus. A synKin derived from the kinase domain of ZAP70 (AAs 326-619) is shown (see **figure S6**). The synSub features (from the N- to C-terminus) a 3x MYC epitope tag, GST, a Y-containing substrate motif derived from CD3Z (AAs 131-164), and a cognate basic zipper (LZ-R). GS linkers are inserted between GST and the substrate motif, as well as the substrate motif and the LZ-R. Brackets indicate part sequences that are varied to tune component function, including LZ affinity (3 total LZ-E variants) and substrate identity (SLP76-derived motif [AAs 108-154] and/or multiple motif repeats). Mutated kinase domain residues that tune catalytic activity are shown in purple, including the residue that was altered to make the kinase dead allele (K369R). Residues that tune LZ affinity are orange. Y residues that are phosphorylated by synKin are shown as dark red. Dots indicate residues (Y142 for CD3Z and Y128 for SLP76) that are recognized in their phospho form by α-pY antibodies (see **Materials and Methods**).

A

FLOW CYTOMETRY GATING AND PLOTTING STRATEGY

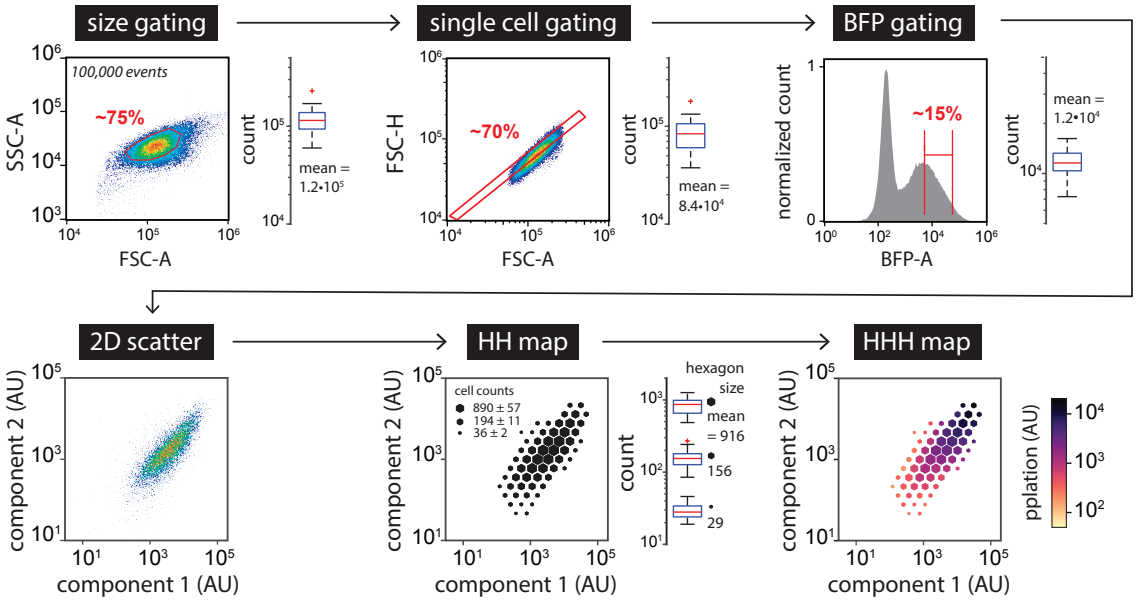

B

FLUORESCENT CHANNEL SPILLOVER

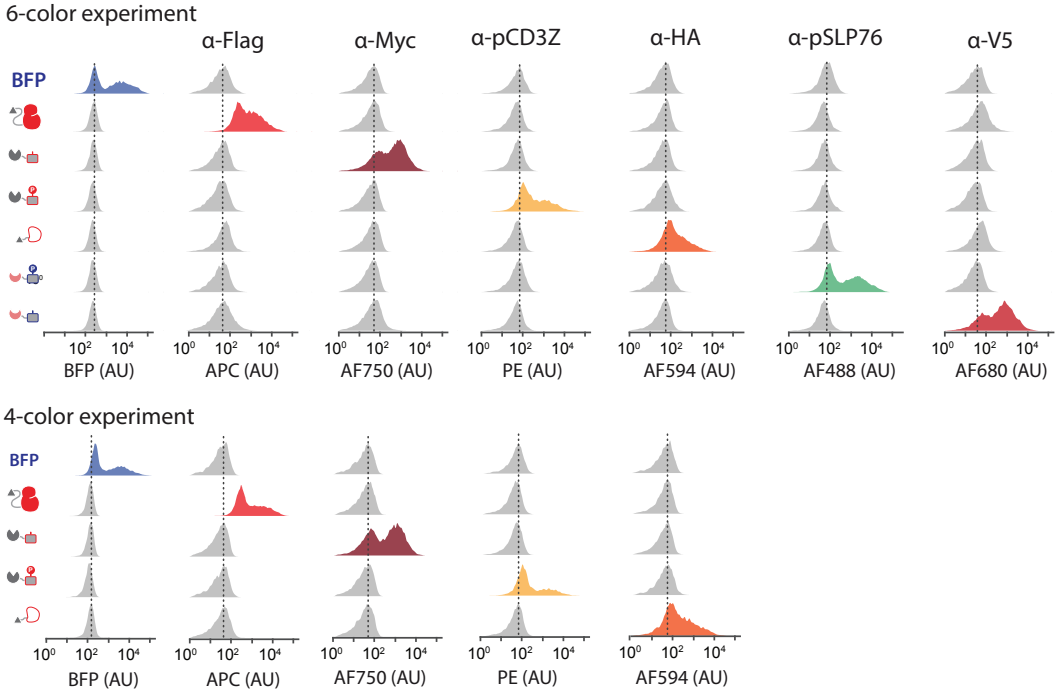

C

TRANSFECTION METHOD COMPARISON

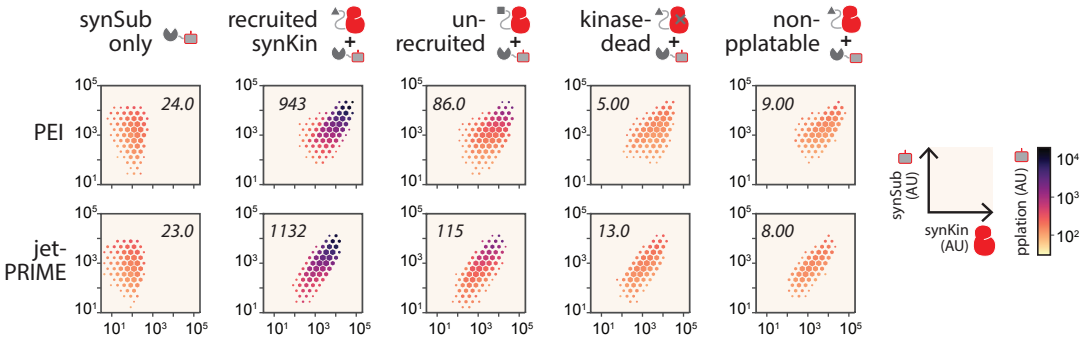

Figure S5. Multi-color flow cytometry data processing workflow. (a) Gating and plotting strategy (see **Materials and Methods** for details). Events (1-2x10^5) are size gated by forward (FSC-A) and side scatter area (SSC-A). Single cells were then gated by forward scatter height (FSC-H) versus area (FSC-A) to yield ~8.4x10^4 events. Cells were gated for BFP+ events to identify transfected cells. Adjacent box plots show event counts distribution for all experimental replicates reported in the study (*n* = 99). Transfection-gated cells are plotted as a two-dimensional scatter plot of component expression (e.g., synKin vs. synSub) and then replotted as an HH plot, where event count is indicated by hexagon size. Average counts per hexagon across all HHH plots in the study are shown in the box plots. HHH plots are created by overlaying a colormap indicating mean phosphorylation level for events in each hexagon. Data shown are representative expression and phosphorylation levels for cells expressing a synKin and synSub (**Figure 1B**, upper right panel). **(b)** Measuring spillover between fluorescence channels. Plasmids expressing individual components (see **Table 1**) harboring epitopes for each antibody. Data from the channel corresponding to the emission of each fluorophore is colored and other histograms are grey (dotted lines, mean intensity from blank cells in each channel). Top, unmixing of a 6-color experiment. Bottom, unmixing of a 4-color experiment. **(c)** Comparing transfection reagents. Experimental groups from **Figure 1B** were transfected using PEI and jetPRIME (see **Materials and Methods**) and data plotted as HHH plots (number in each HHH plot, phosphorylation geometric mean).

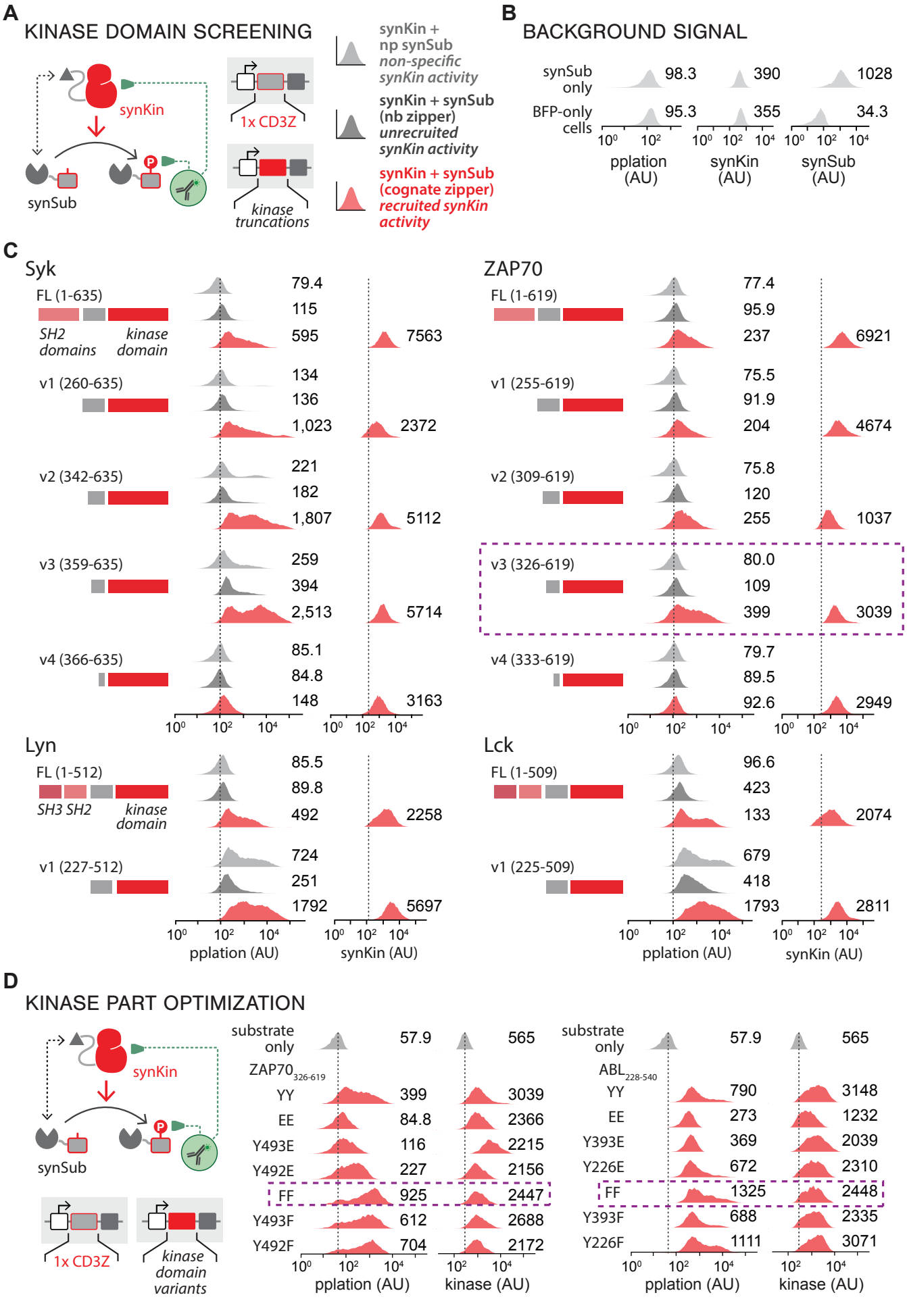
A
KINASE DOMAIN SCREENING
synKin
synSub
1x CD3Z
kinase truncations
synKin + np synSub
non-specific synKin activity
synKin + synSub (nb zipper)
unrecruited synKin activity
synKin + synSub (cognate zipper)
recruited synKin activity
B
BACKGROUND SIGNAL
synSub only
BFP-only cells
98.3
390
1028
95.3
355
34.3
pplation (AU)
synKin (AU)
synSub (AU)
C
Syk
FL (1-635)
SH2 domains
kinase domain
v1 (260-635)
v2 (342-635)
v3 (359-635)
v4 (366-635)
79.4
115
595
7563
134
136
1,023
2372
221
182
1,807
5112
259
394
2,513
5714
85.1
84.8
148
3163
ZAP70
FL (1-619)
v1 (255-619)
v2 (309-619)
v3 (326-619)
v4 (333-619)
77.4
95.9
237
6921
75.5
91.9
204
4674
75.8
120
255
1037
80.0
109
399
3039
79.7
89.5
92.6
2949
Lyn
FL (1-512)
SH3 SH2
kinase domain
v1 (227-512)
85.5
89.8
492
2258
724
251
1792
5697
pplation (AU)
synKin (AU)
Lck
FL (1-509)
v1 (225-509)
96.6
423
133
2074
679
418
1793
2811
pplation (AU)
synKin (AU)
D
KINASE PART OPTIMIZATION
synKin
synSub
1x CD3Z
kinase domain variants
substrate only
ZAP70326-619
YY
EE
Y493E
Y492E
FF
Y493F
Y492F
57.9
565
399
3039
84.8
2366
116
2215
227
2156
925
2447
612
2688
704
2172
pplation (AU)
kinase (AU)
substrate only
ABL228-540
YY
EE
Y393E
Y226E
FF
Y393F
Y226F
57.9
565
790
3148
273
1232
369
2039
672
2310
1325
2448
688
2335
1111
3071
pplation (AU)
kinase (AU)

Figure S6. Screening kinase domain truncation variants for synKin optimization. (a) synKin activity screen design. Truncation variants are fused to a cognate or non-binding (nb) LZ and co-expressed with synSub in HEK293T cells. Flow cytometry is used to measure variant expression levels (α-FLAG, APC) and phosphorylation signal (α-pY, PE). α-pY antibody signal from non-specific kinase activity is assessed by co-expression with a non-phosphorylatable (np) synSub. Recruitment-independent phosphorylation is assessed by co-expressing synSub with kinase variants fused to a nb LZ. Recruitment-dependent activity is tested by expressing synSub with active kinase variants fused to cognate LZ. **(b)** Background signal for phosphorylation level and component expression measured for empty cells and cells expressing synSub only. **(c)** Phosphorylation signal and expression level for each truncated variant are measured for non-specific, unrecruited, and recruited kinase configurations. Numbers indicate the geometric mean of the measured histograms. Dotted lines indicate background measurements for cells transfected with BFP only. Purple box indicates the truncation allele chosen for further synKin engineering. **(d)** Screening synKin point mutants for optimized expression and activity profiles. Potentially phosphorylatable Y residues in selected ZAP70 and ABL truncation variants are mutated to F or E, fused to a cognate LZ, and co-expressed with synSub containing a single repeat of a CD3Z-derived ITAM motif (AAs 131-164). Phosphorylation level and kinase expression were measured for all the mutants. Numbers indicate histogram geometric means. Dotted lines indicate background measured for empty cells. Purple boxes indicate the mutant alleles chosen as synKins for use throughout the study.

S7

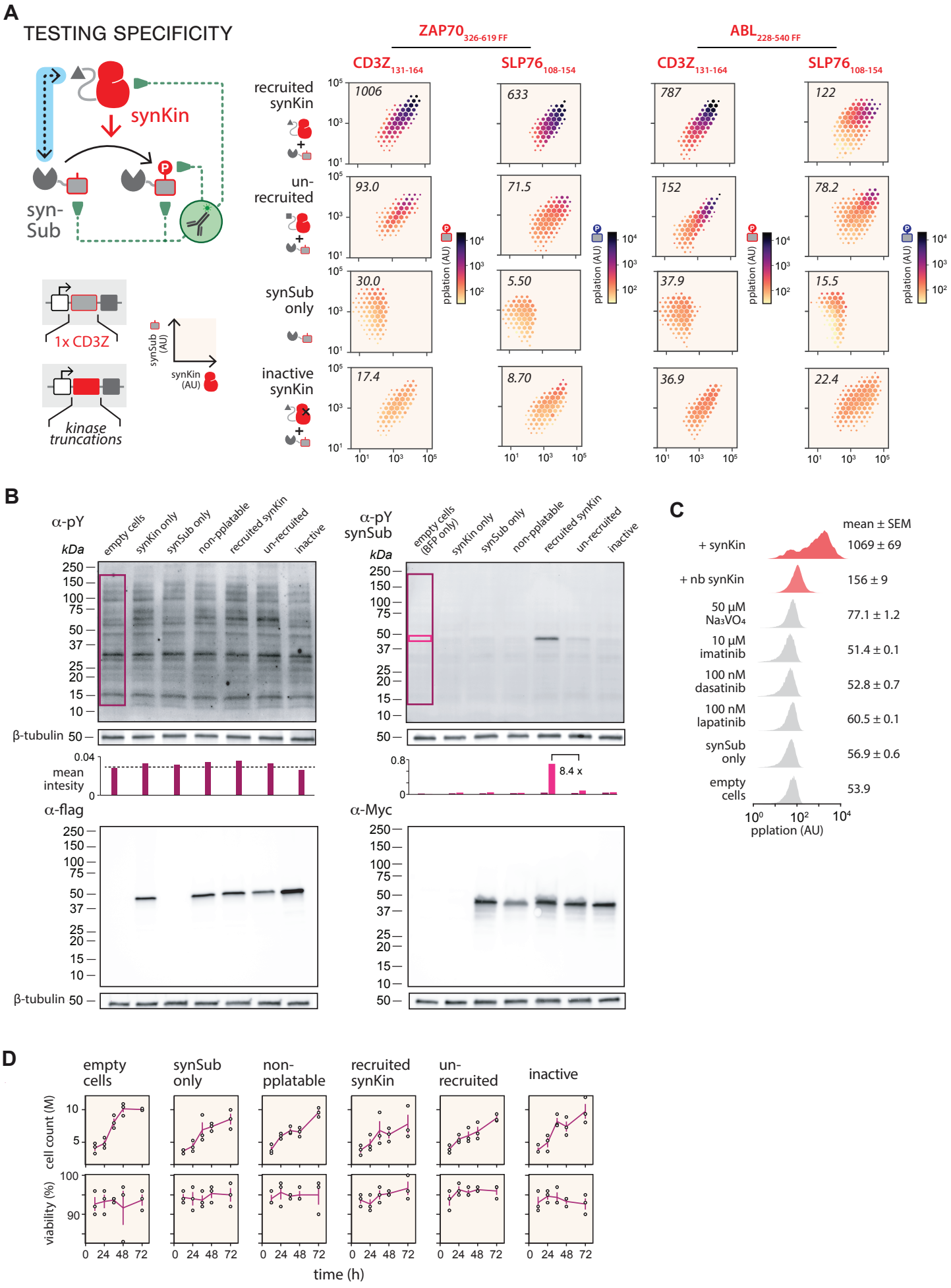
A
TESTING SPECIFICITY
synKin
syn-Sub
1x CD3Z
kinase truncations
synSub (AU)
synKin (AU)
ZAP70326-619 FF
ABL228-540 FF
CD3Z131-164
SLP76108-154
recruited synKin
un-recruited
synSub only
inactive synKin
1006
633
787
122
93.0
71.5
152
78.2
30.0
5.50
37.9
15.5
17.4
8.70
36.9
22.4
pplation (AU)
B
α-pY
kDa
empty cells
synKin only
synSub only
non-pplatable
recruited synKin
un-recruited
inactive
β-tubulin
mean intesity
α-pY synSub
empty cells (BFP only)
8.4 x
α-flag
α-Myc
C
mean ± SEM
+ synKin
1069 ± 69
+ nb synKin
156 ± 9
50 μM Na3VO4
77.1 ± 1.2
10 μM imatinib
51.4 ± 0.1
100 nM dasatinib
52.8 ± 0.7
100 nM lapatinib
60.5 ± 0.1
synSub only
56.9 ± 0.6
empty cells
53.9
pplation (AU)
D
empty cells
synSub only
non-pplatable
recruited synKin
un-recruited
inactive
cell count (M)
viability (%)
time (h)

Figure S7. Testing specificity of synthetic signaling components. (a) The two synKin designs-identified in **figure S6B** ($ZAP70_{326\text{-}619\ FF}$ and $ABL_{228\text{-}540\ FF}$) were tested against synSubs harboring motifs derived from CD3Z and SLP76 (see **fig. S4**), number in each HHH plot indicates phosphorylation geometric mean. **(b)** Western blot analysis of synKin and synSub components **(**see **Fig. 1B),** along with controls. Lysates were generated for indicated samples (see **table S3**) and probed for general α-pY, α-pY synSub, α-Flag, and α-Myc. In the pY blot, magenta bar plots display normalized intensity values relative to the loading control for the area highlighted by magenta boxes, with the dashed line showing the value from empty cells. In the pY synSub blot, pink bar plots display normalized intensity values for the area highlighted by pink boxes, while magenta bar plots show values for the area highlighted by magenta boxes subtracted by those highlighted by pink boxes to represent background signaling from the pY synSub antibody. The values above the bar plots indicate the fold change in synSub phosphorylation between the compared samples. **(c)** Cells expressing synSub were treated with various Y kinase inhibitors and Na_3VO_4. Histograms of phosphorylation level is shown for each condition, with values showing mean phosphorylation (AU) ± SEM (n=2). **(d)** Growth burden of synthetic signaling components on HEK293T cells. Cell populations transfected with constructs encoding expression of the indicated proteins were measured for viability and cell density every 12 h for the experimental groups in **Figure 1B,** with error bars representing mean ± SEM (n=3).

PTPN1

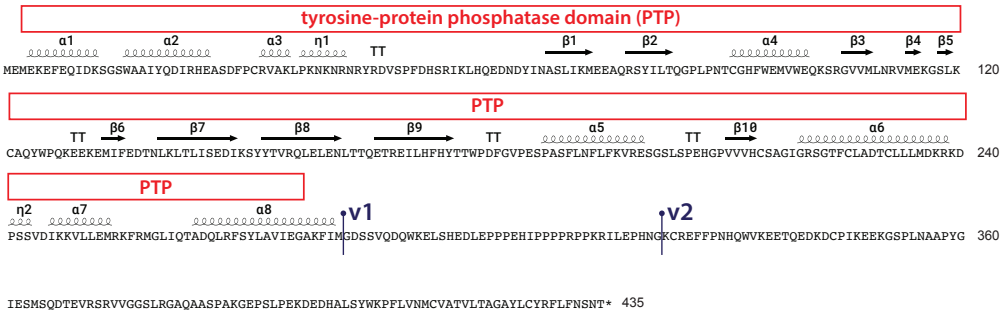

PTPN3 (PTPH1)

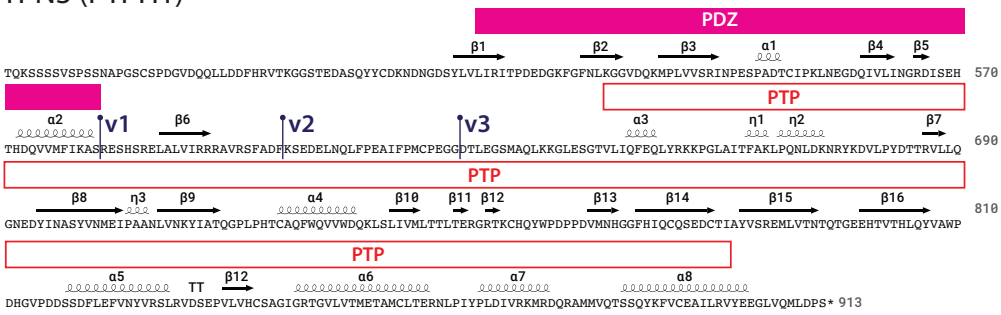

PTPN6 (SHP1)

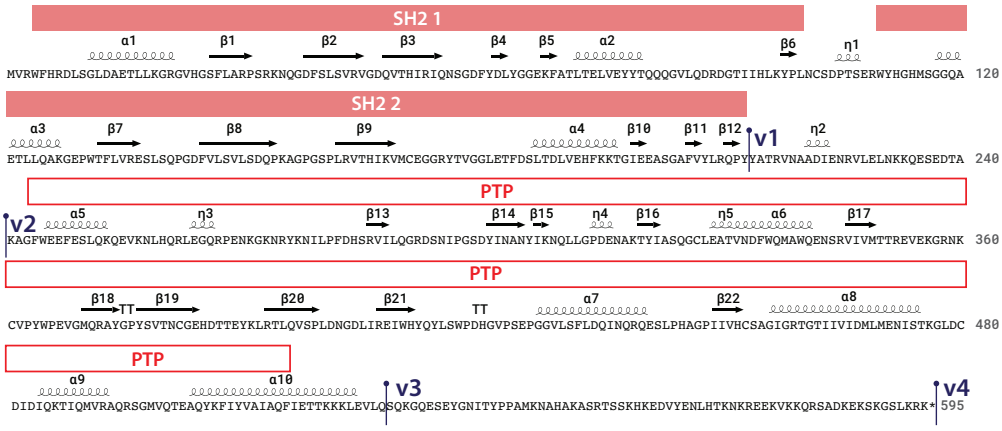

Figure S8. Native Y phosphatase sequences. Amino acid sequences with 2° structures for all the phosphatases tested in the study. PTPN1, PTPN3, and PTPN6 were chosen to represent the three PTP subfamilies (see **Supplementary Text**). Red boxes indicate the boundaries for PTP domains and regulatory domains such as PDZ and SH2 (Uniprot predictions). 2° structure features (α-helix and β-strand) are also indicated. Purple lollipops indicate boundaries for tested truncation variants.

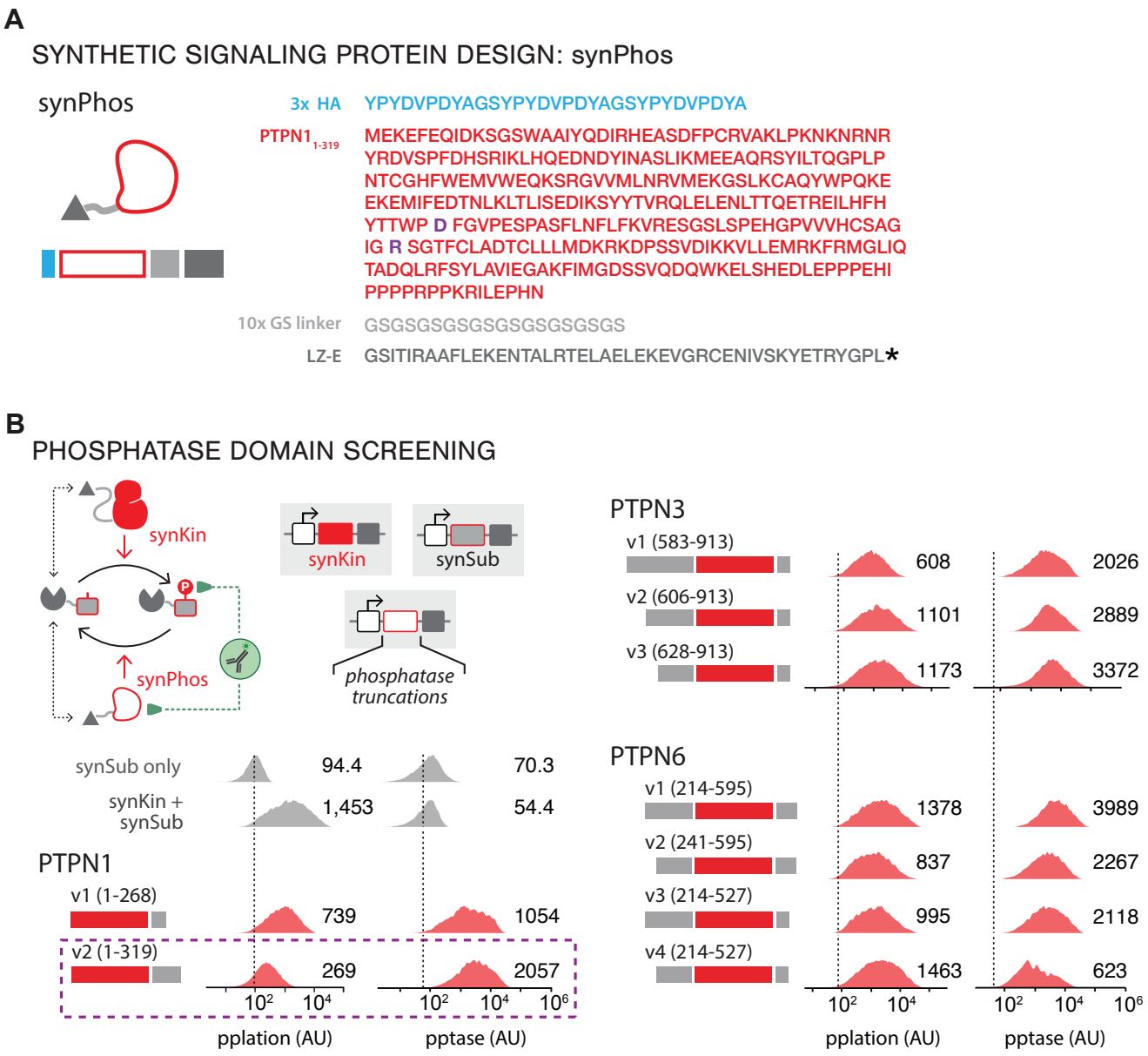

Figure S9. Synthetic phosphatase designs and truncation variant screening. (a) Amino acid sequences of parts comprising synPhos. synPhos contains a 3x HA epitope tag, truncated phosphatase domain, flexible 10x GS linker, and an LZ-E. A synPhos derived from PTPN1 is shown (see **fig. S8**). The purple residue indicates the position of the mutations used for the phosphatase dead allele (D181A, R221M). **(b)** All phosphatase truncations are fused with a cognate LZ and co-expressed with the synKin and synSub shown in **Figure 1B**. The phosphorylation levels of synSub and expression levels of phosphatase domain truncation variants are measured by flow cytometry. Numbers next to the histogram indicate the geometric mean of the measured distribution. Dotted lines indicate the mean intensity from blank cells for phosphorylation and phosphatase expression. Purple box highlights the chosen variant for synPhos used in circuit construction throughout the study.

GFP NORMALIZATION CONTROLS

ANTIBODY CONJ FLUOROPHORE → GFP FLUORESCENCE UNITS

Flag-to-GFP

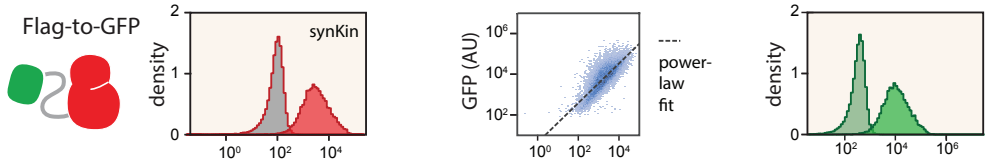

3x FLAG	DYKDHDGDYKDHDIDYKDDDDK
ZAP70$_{326\text{-}619\ FF}$	DKKLFLKRDN . . . TQKAEAACAS
20x GS linker	GSGSGSGSGSGSGSGSGSGSGSGSGSGSGSGSGSGSGS
EGFP	VSKGEELFTGVVPILVELDGDVNGHKFSVSGEGEGDATYGKLTLKFICTTGKLPVPWPTL VTTLTYGVQCFSRYPDHMKQHDFFKSAMPEGYVQERTIFFKDDGNYKTRAEVKFEGDT LVNRIELKGIDFKEDGNILGHKLEYNYNSHNVYIMADKQKNGIKVNFKIRHNIEDGSVQLA DHYQQNTPIGDGPVLLPDNHYLSTQSALSKDPNEKRDHMVLLEFVTAAGITLGMDELYK*

Myc-to-GFP

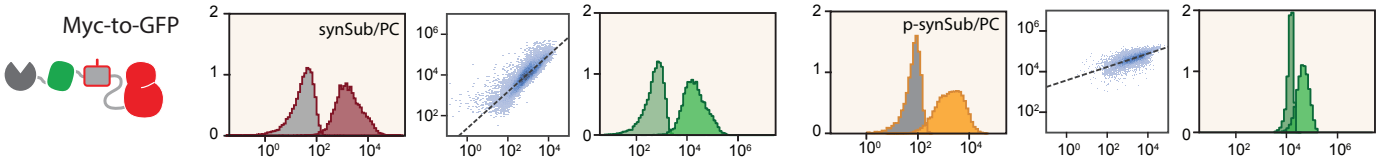

3x MYC	EQKLISEEDLLRSEEQKLISEEDLLRSEEQKLISEEDL
ZAP70$_{326\text{-}619\ FF}$	DKKLFLKRDN . . . TQKAEAACAS
20x GS linker	GSGSGSGSGSGSGSGSGSGSGSGSGSGSGSGSGSGSGS
CD3Z$_{131\text{-}164}$ (ITAM3)	ERRRGKGHDGLYQGLSTATKDTYDALHMQALPPR
15x GS linker	GSGSGSGSGSGSGSGSGSGSGSGSGS
EGFP	VSKGEELFTG . . . GITLGMDELYK
LZ-R	GSGTGSLEIRAAFLEKENTALRTRAAELRKRVGRCRNIVSKYETRYGPL*

V5-to-GFP

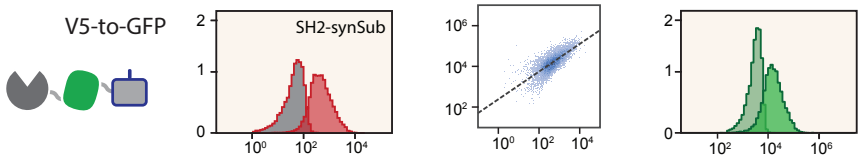

3x V5	MGNSGKPIPNPLLGLDSTGSGKPIPNPLLGLDSTGSGKPIPNPLLGLDST
ZAP70$_{326\text{-}619\ FF}$	DKKLFLKRDN . . . TQKAEAACAS
20x GS linker	GSGSGSGSGSGSGSGSGSGSGSGSGSGSGSGSGSGSGS
3x SLP76$_{108\text{-}354}$	(SFEEDDYESPNDDQDGEDDGDYESPNEEEEAPVEDDADYEPPPSNDEESGGSGGGS)$_3$
10x GS linker	GSGSGSGSGSGSGSGSGSGS
LZ-R	GSGTGSLEIRAAFLEKENTALRTRAAELRKRVGRCRNIVSKYETRYGPL*

HA-to-GFP

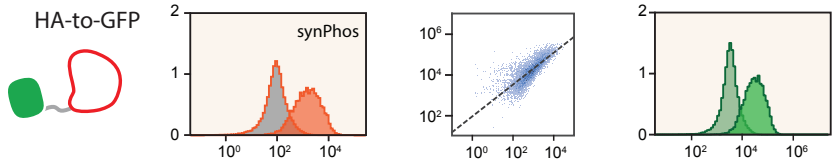

3x HA	YPYDVPDYAGSYPYDVPDYAGSYPYDVPDYA
PTPN1$_{1\text{-}139}$	RESHSRELAL . . . VYEEGLVQML
20x GS linker	GSGSGSGSGSGSGSGSGSGSGSGSGSGSGSGSGSGSGS
EGFP	VSKGEELFTG . . . GITLGMDELYK*

SLP76-to-V5

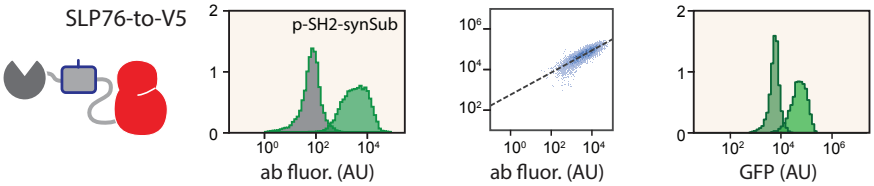

3x V5	MGNSGKPIPNPLLGLDSTGSGKPIPNPLLGLDSTGSGKPIPNPLLGLDST
GST	SPILGYWKIK . . . FGGGDHPPKS
10x GS linker	GSGSGSGSGSGSGSGSGS
3x SLP76$_{108\text{-}354}$	(SFEEDDYESPNDDQDGEDDGDYESPNEEEEAPVEDDADYEPPPSNDEE SGGSGGGSS)$_3$
15x GS linker	GSGSGSGSGSGSGSGSGSGSGSGSGS
EGFP	VSKGEELFTG . . . GITLGMDELYK
LZ-R	GSGTGSLEIRAAFLEKENTALRTRAAE LRKRVGRCRNIVSKYETRYGPL*

Figure S10. Design of constructs for fluorescence signal conversion. Constructs used for converting antibody-conjugated fluorophore singal to EGFP units. The FLAG-to-EGFP construct replaces the synKin LZ from **figure S4** with EGFP. The HA-to-EGFP construct replaces the synPhos LZ from **figure S9A** with EGFP. A single construct supports pCD3Z-to-EGFP and MYC-to-EGFP conversion; it has a 3x MYC epitope, ZAP70 kinase domain (from **fig. S4**), 1x CD3Z substrate motif, EGFP, and a cognate LZ-R. The V5-to-EGFP construct contains a 3x V5 epitope tag, GST, 1x SLP76 substrate motif, EGFP, and LZ-R. 20x GS linkers separate the substrate motif from the synKin and EGFP. The pSLP76-to-V5 construct has 3x V5 epitope tag, ZAP70 kinase domain (from **fig. S4**), 1x SLP76 peptide, a cognate LZ-R, a 20x GS linker are inserted between kinase domain and SLP76, and a 10x GS linker between SLP76 and LZ. Constructs were expressed in HEK293T cells and used to convert ab-conjugated fluorescence into EGFP signal. The left column shows the distribution of fluorescence signals from each of the constructs (represented by colored histograms) alongside empty cells (depicted in grey-shaded histograms). Middle column, the 2D scatter plot of the fluorescence vs. EGFP expression from each construct, with dashed lines denoting the power-law fit from ab-conjugated fluorescence to EGFP. Right column, the distribution of the EGFP signal from the corresponding construct (light green histograms) and empty cells (depicted in dark green histograms).

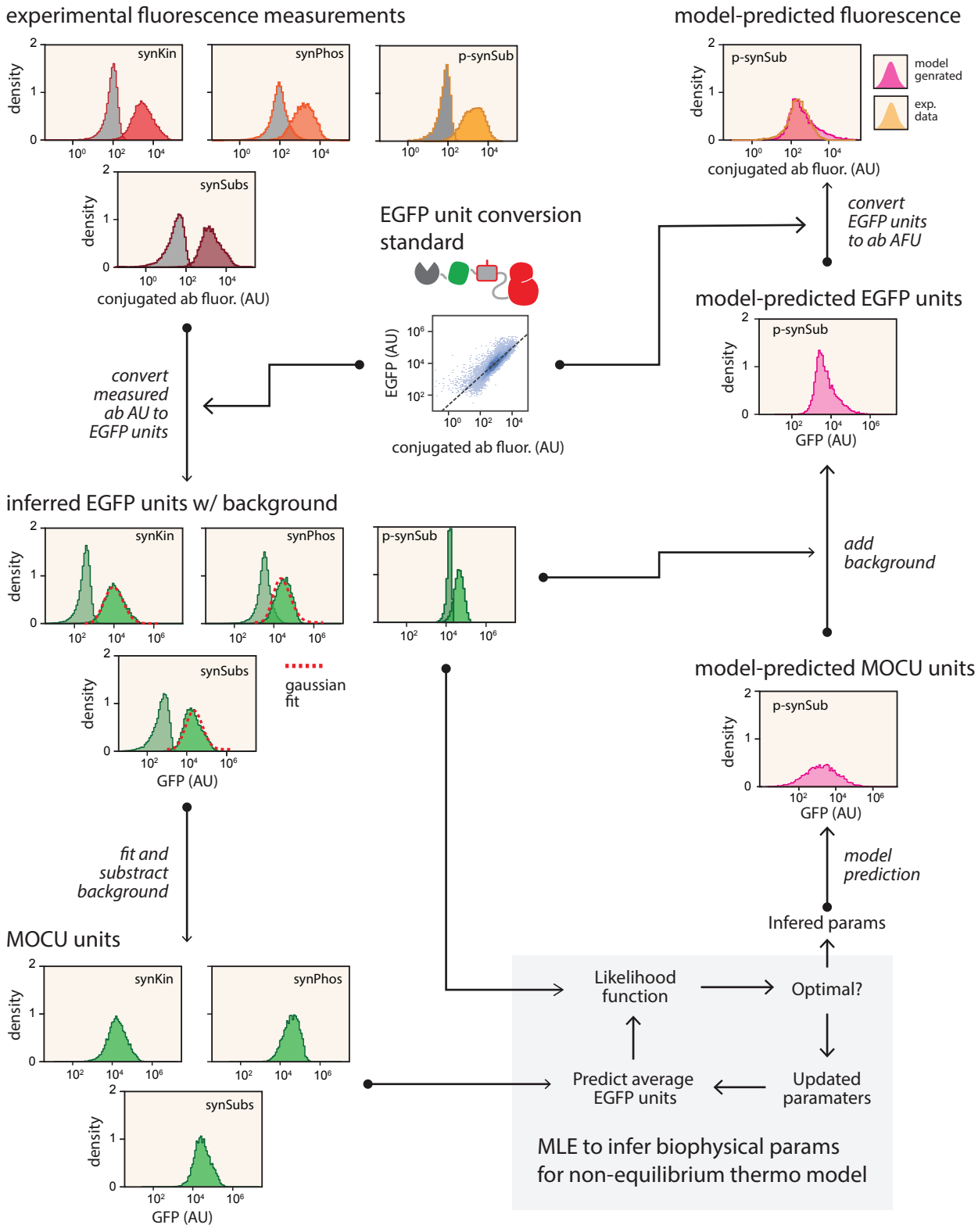

Figure S11. Computational workflow for model fitting and phosphorylation prediction. On the left (from top to bottom), antibody-conjugated fluorescence values obtained from flow cytometry experiments are converted into stoichiometrically equivalent EGFP units (see **fig. S10**) and then background fluorescence values are subtracted, yielding model-operable concentration unit (MOCU) distributions that are then used for fitting. On the right (from bottom to top), parameters iteratively generated from the model fitting via MLE are used to generate predicted phosphorylation levels in EGFP units, which then have background signal added back to them. Finally, predicted EGFP signals are transformed back into phospho-antibody fluorescence for comparison with experimental measurements (see **Data fitting and prediction** section for details).

A

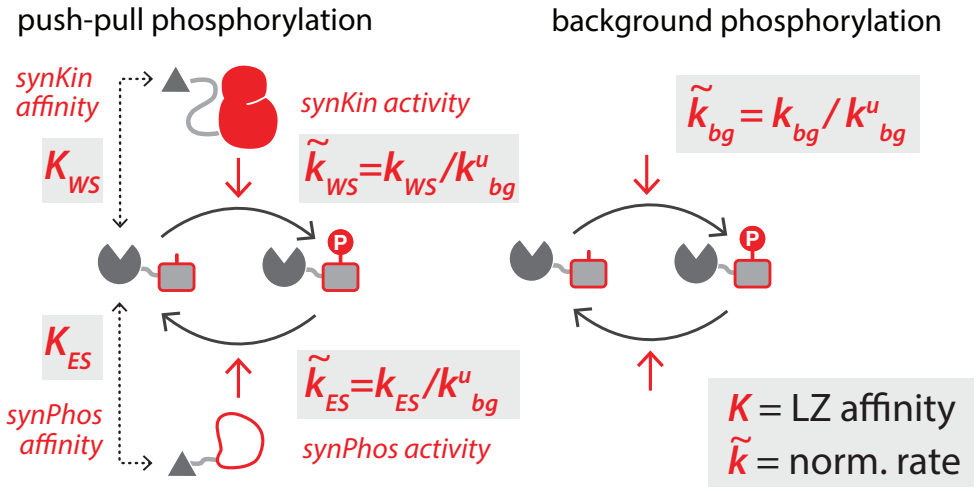

B

MODEL PARAMETER FITTING

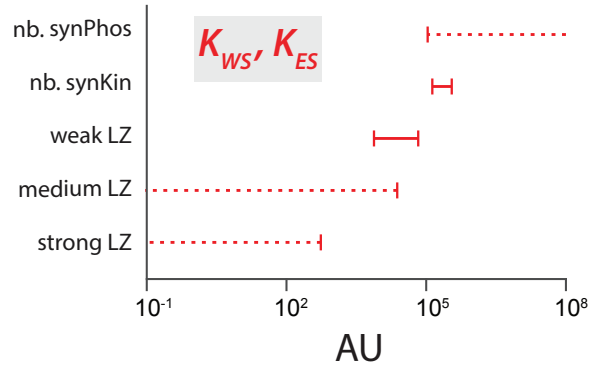

	K		K_{min}		K_{max}		
	AU	K_d	AU	K_d	AU	K_d	*in vitro*
nb. synPhos	4.0×10^{5}	47	1.1×10^{5}	13	$>10^{8}$	$>10^{7}$	N.A.
nb. synKin	2.2×10^{5}	26	1.3×10^{5}	15	3.5×10^{5}	43	N.A.
weak LZ	1.1×10^{4}	1.3	7.6×10^{3}	9.0×10^{-1}	6.7×10^{4}	8.2	6.5×10^{-1}
medium LZ	1.3×10^{3}	1.6×10^{-1}	$<10^{-1}$	$< 10^{-6}$	2.4×10^{4}	2.9	1.6×10^{-1}
strong LZ	1.7	2.1×10^{-4}	$<10^{-1}$	$< 10^{-6}$	5.5×10^{2}	6.7×10^{-2}	2.8×10^{-3}

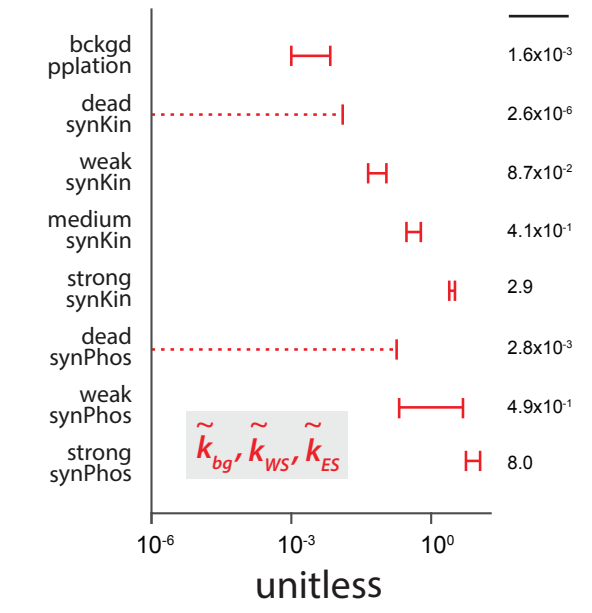

	$\tilde{k}$	$\tilde{k}_{min}$	$\tilde{k}_{max}$
bckgd pplation	1.6×10^{-3}	1.0×10^{-3}	6.9×10^{-3}
dead synKin	2.6×10^{-6}	$<10^{-6}$	4.6×10^{-3}
weak synKin	8.7×10^{-2}	4.5×10^{-2}	1.1×10^{-1}
medium synKin	4.1×10^{-1}	3.0×10^{-1}	6.1×10^{-1}
strong synKin	2.9	2.5	3.3
dead synPhos	2.8×10^{-3}	$<10^{-6}$	1.8×10^{-1}
weak synPhos	4.9×10^{-1}	2.1×10^{-1}	4.9
strong synPhos	8.0	5.6	11

Figure S12. Fit parameters for one-layer synthetic phosphorylation cycle . (a) Parameterization for background-normalized synKin/synPhos activity rates (k) and binding affinity for the LZs (K). All catalytic rates are normalized by the background dephosphorylation rate (k_{bg}). **(b)** Summary of thermodynamic model parameters. Each parameter is plotted with two-sided error bars (see **Data fitting and prediction section** for how error bars were generated). Solid line error bars indicate parameters with upper and lower limits, and the dashed line indicates parameters with only an upper or lower limit. For affinity and rate constants, fitted, lower limit, and upper limit values are shown in three columns. Affinity values are expressed as arbitrary units and as K_d values calculated based on *in vitro* measured data value for the medium affinity LZ value. Other *In vitro* measured K_d values are shown in the last column.

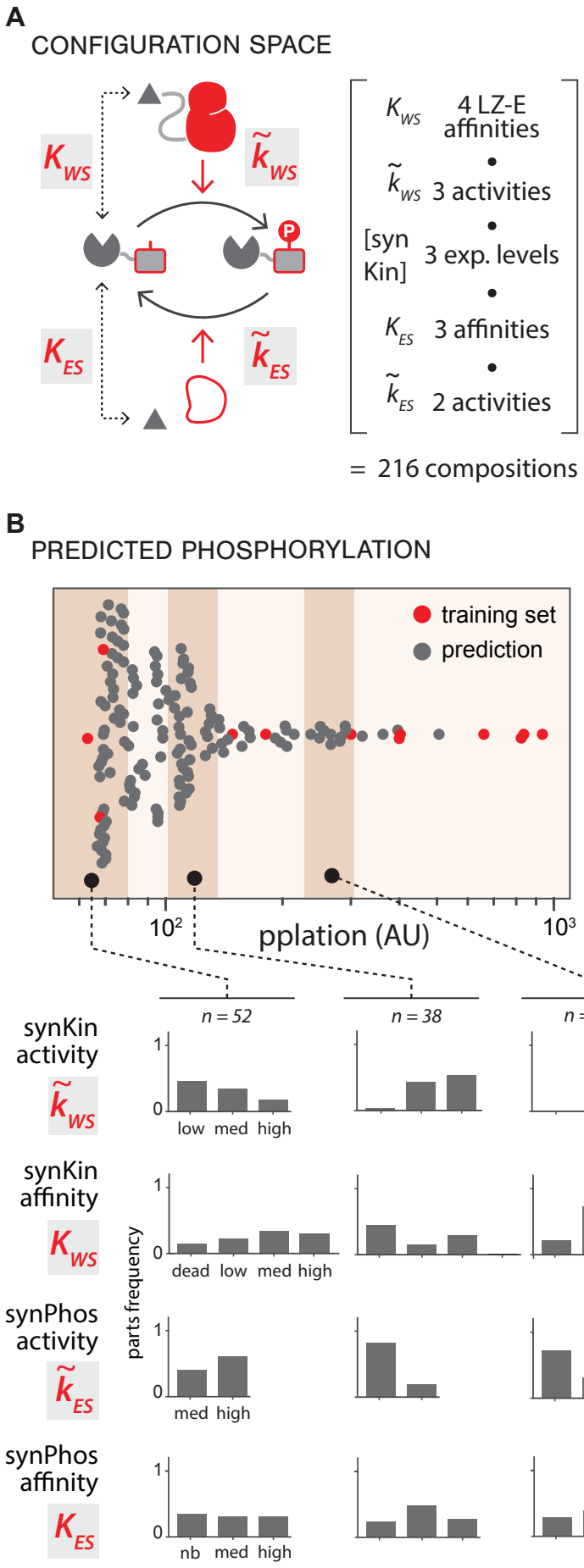

Figure S13. Modeling phosphouylation cycle behavior space. (a) Defining the part-allowed composition space. Part combinations that include kinase domains with different activities (active site mutations), synKin expression level (different Kozak sequences), and LZ-E affinities resulted in a final set of 216 compositions. **(b)** Predicted phosphorylation levels for all compositions in phosphorylation cycle design space. Beeswarm plot corresponds to the geometric mean of phosphorylation for a each circuit composition. Red dots indicate experimentally measured compositions that the model was trained on (n=12, data from **Fig. 1B-D**) while grey dots indicated model-predicted behavior for the rest of design space (n=204). Below the behavior space is a part frequency analysis of part parameter values for three different scatter regions, corresponding to low, medium, and high levels of predicted phosphorylation.

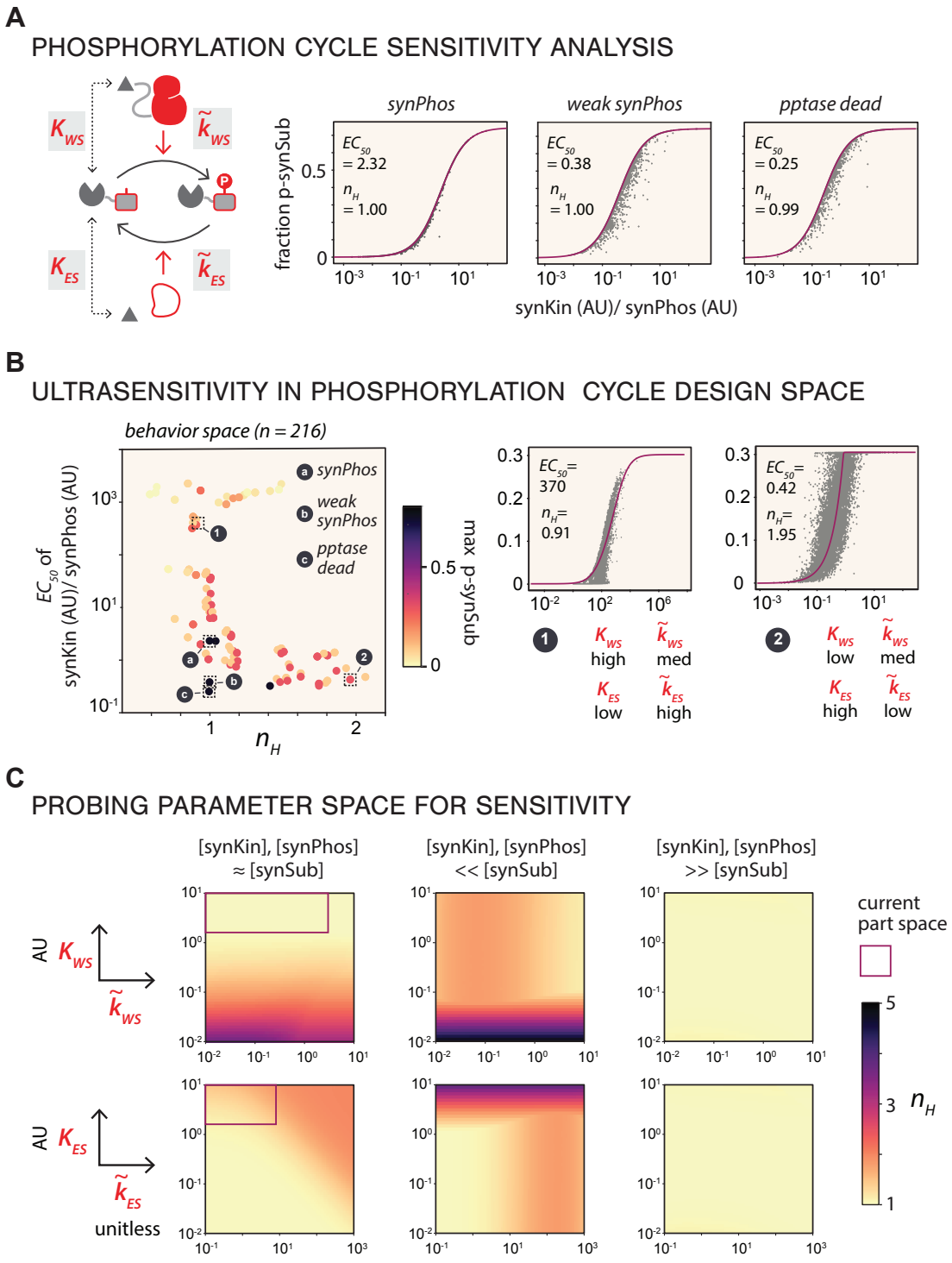

Figure S14. Sensitivity analysis phosphorylation cycle design space. (a) Behavior of circuit compositions in **Fig. 1D** are shown in Goldbeter-Koshland-style sensitivity plots, with [synKin]/[synPhos] ratio as x axis and fraction synSub phosphorylation as the y axis**.** Grey dots, noise model-inferred measurements acquired from **Fig. 1D** for single cells; magenta lines, predicted dose response curve based on the sampled expression level space for [synKin]/[synPhos]. n_H, effective hill coefficient; EC_{50}, [synKin]/[synPhos] values at half maximal activation (unitless). See **Supplementary Text** for detail. **(b)** Left, scatter plot of EC_{50} and n_H for all part-allowed circuit configurations from **Fig. 1F**, color scale shows the maximum synSub phosphorylation level. Circuits from **Fig. S14A** are highlighted as **a, b,** and **c**. One circuit from high n_H region and one from the high EC_{50} region are also highlighted. Predicted single-cell fraction phosphorylation levels and predicted curves are shown in Goldbeter-Koshland plots, with detailed part usage displayed below. **(c)** Sensitivity analysis for expanded parameter space. n_H heatmaps are shown while varying synKin (top) or synPhos (bottom) activity vs. LZ affinity, shown for three distinct synSub concentations. K_{WS} and K_{ES} are plotted with AU, $\tilde{k}_{WS}$ and $\tilde{k}_{ES}$ are unitless, as shown in **fig. S12B.** Purple boxes indicate current parts allowed space from **fig. S12B**.

A SYNTHETIC PROTEIN DESIGN: TF ACTIVATION

SV40 NLS	MPKKKRKVGS
VP64	DALDDFDLDMLGSDALDDFDLDMLGSDALDDFDLDMLGSDALDDFDLDML
p65	INSRSSGSPK . . . DFSALL
Rta	GSGSGSRDSR . . . LFGSPKKKRK
10x GS linker	GSGSGGSGSG
LZ-E	GSITIRAAFLEKENTALRTELAELEKEVGRCENIVSKYETRYGPL*
3x MYC	EQKLISEEDLLRSEEQKLISEEDLLRSEEQKLISEEDLINSVN
SV40 NLS	PKKKRKV
3x ZF (42-10)	VNQLERPFQCRICMRNFSTGQILDRHTRTHTGEKPFQCRIC MRNFSVAHSLKRHLRTHTGEKPFQCRICMRNFSDPSNLRR HLKTHLRGGSGSSGSGS
10x GS linker	GSGSGSGSGS
LZ-R	GSGTGSLEIRAAFLEKENTALRTRAAELRKRVGRCRNIVSKYETRYGPL*

B TESTING synTF RECRUITMENT

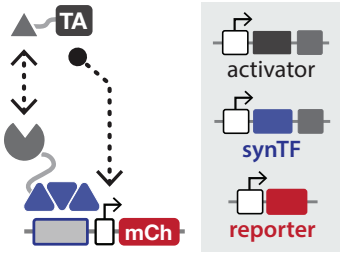

C SYNTHETIC PROTEIN DESIGN: PHOSPHO-DEPENDENT TRANSCRIPTIONAL ACTIVATION

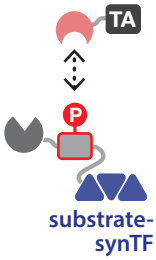

SV40 NLS	MPKKKRKVG
ZAP70 $SH2_{2-254}$	PDPAAHLPFF . . . LKEACPNSSA
10x GS linker	GSGSG
VP64	DALDDFDLDMLGSDALDDFDLDMLGSDALDDFDLDMLGSDALDDFDLDML
p65	INSRSSGSPK . . . DFSALL
Rta	GSGSGSRDSR . . . LFGSPKKKRK*
3x MYC	EQKLISEEDLLRSEEQKLISEEDLLRSEEQKLISEEDL
3x ZF (42-10)	VNQLER . . . SSGSGS
GST	SPILGY . . . DHPPKS
10x GS linker	GSGSGSGSGS
$CD3Z_{131-164}$ (ITAM3)	$(ERRRGKGHDGLYQGLSTATKDTYDALHMQALPPRGSGSGSGSGS)_2$ ERRRGKGHDGLYQGLSTATKDTYDALHMQALPPR
LZ-R	GSGTGSLEIRAAFLEKENTALRTRAAELRKRVGRCRNIVSKYETRYGPL*

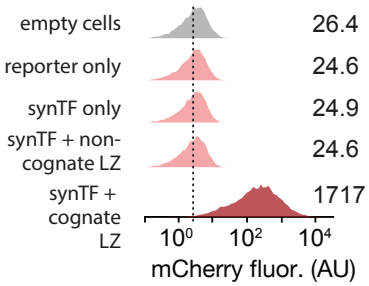

D TESTING PHOSPHO-RECRUITMENT

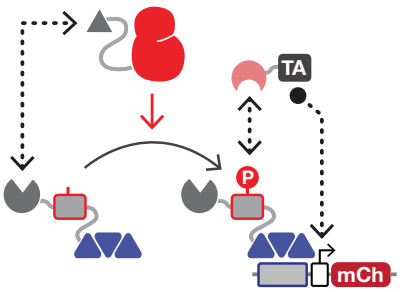

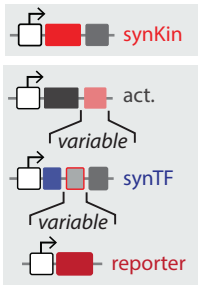

TCR-ITAMs

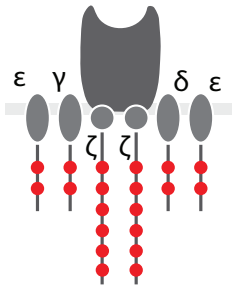

CD3Z-ITAM1 (64-95)
tSH2 domains YQQGQNQLpYNELNLG - RREEpYDVLDKRRGRDP

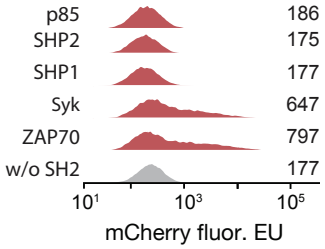

CD3Z-ITAM2 (64-95)
NPQEGLpYNELQKDKM - AEApYSEIGMKGERRRGK

CD3Z-ITAM3 (131-164)
ERRRGKGHDGLpYQGLST - ATKDTpYDALHMQALPPR

CD3δ (141-171)
ALLRNDQVpYQPLRDRD - DAQpYSHLGGNWARNK

CD3γ (163-182)
PPPNDQLpYQPLKDRE - DDQpYSHLQGNQLRRN

CD3ε (180-207)
PPPVPNPDpYEPIRK - GQRDLpYSGLNQRRI

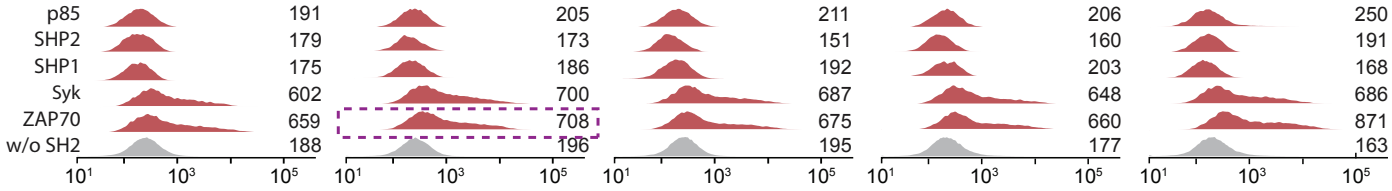

BCR-ITAMs

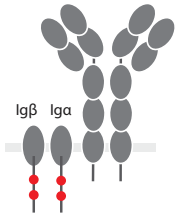

IgA ITAM (181-211)
EYEDENLpYEGLNLDD - CSMpYEDISRGLQGTYQ

IgB ITAM (188-121)
AGMEEDHTpYEGLDIDQ - TATpYEDIVTLRTGEVKWS

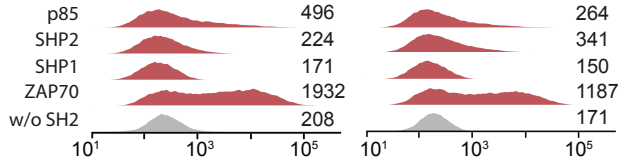

Fc RECEPTOR ITAMS

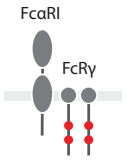

FcRγ (55-86)
SYEKSDGVpYTGLSTR - NQETpYETLKHEKPPQ

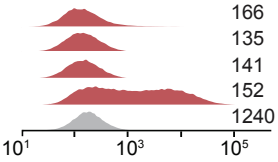

PDGFR 731-757
SLTGESDGGpYMDM - SKDESVDpYVPMLDM

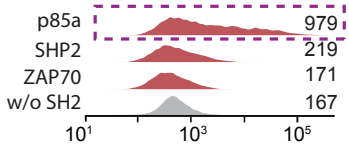

SHPS-1 ITIM (424-459)
TNDITpYADLNLPKGKKPA - PQAAEPNNHTEpYASIQTS

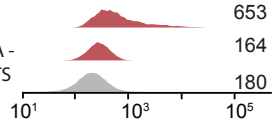

Figure S15. Using a transcriptional reporter to measure phospho-dependent tSH2 binding. **(a)** Reporter design. A phospho-dependent transcriptional reporter system leverages the interaction between a pY motif and a tSH2 domain to activate transcription. It consists of two parts: 1) a transactivator-tSH2 fusion, which contains an SV40 NLS, VPR activation domain, and a tSH2 domain; 2) a synTF-pY motif fusion, which contains of a 3x MYC epitope, SV40 NLS, 3x ZF array, GST, a 3x substrate motif, and LZ-R. **(b)** Design and validation of LZ-recruited transcriptional activation system. The LZ-recruited transcriptional activation module consists of two parts: an activator comprising a VPR-LZ-E fusion with an N-terminal NLS; 2) a synTF made up of a 3x MYC epitope tag, SV40 NLS, 3x ZF array, and LZ-E. **(c)** Using the reporter to test phospho-dependent tSH2 recruitment. Phosphorylation by synKin can result in binding between VPR-tSH2 and synTF-pY ITAM-LZ-R activates the reporter gene expression. Binding specificity was assessed by screening tandem tSH2 domains from ZAP70, Syk, SHP1, SHP2, and p85a against ITAM motifs from the TCR, BCR and Fc receptor, as well as tandem pY motifs from PDGFR, and SHPS-1. Amino acid sequences for each motif are shown with phosphorylated Ys highlighted in red. Geometric means are shown beside histograms. tSH2/motif pairs chosen for later use are indicated with purple boxes. **(d)** Binding of VPR-LZ-E to synTF-LZ-R activates reporter gene expression. EUs encoding activator, synTF, and mCherry reporter were assembled into one plasmid (grey box) using the workflow shown in **figure S1**. Flow cytometry data for the mCherry reporter expression on the right for the 3-EU combination, empty cells as well as reporter only, synTF only, and negative controls without recruited activator (non-cognate LZ). Numbers indicate geometric means for mCherry expression. The dotted line indicates background mCherry fluorescence.

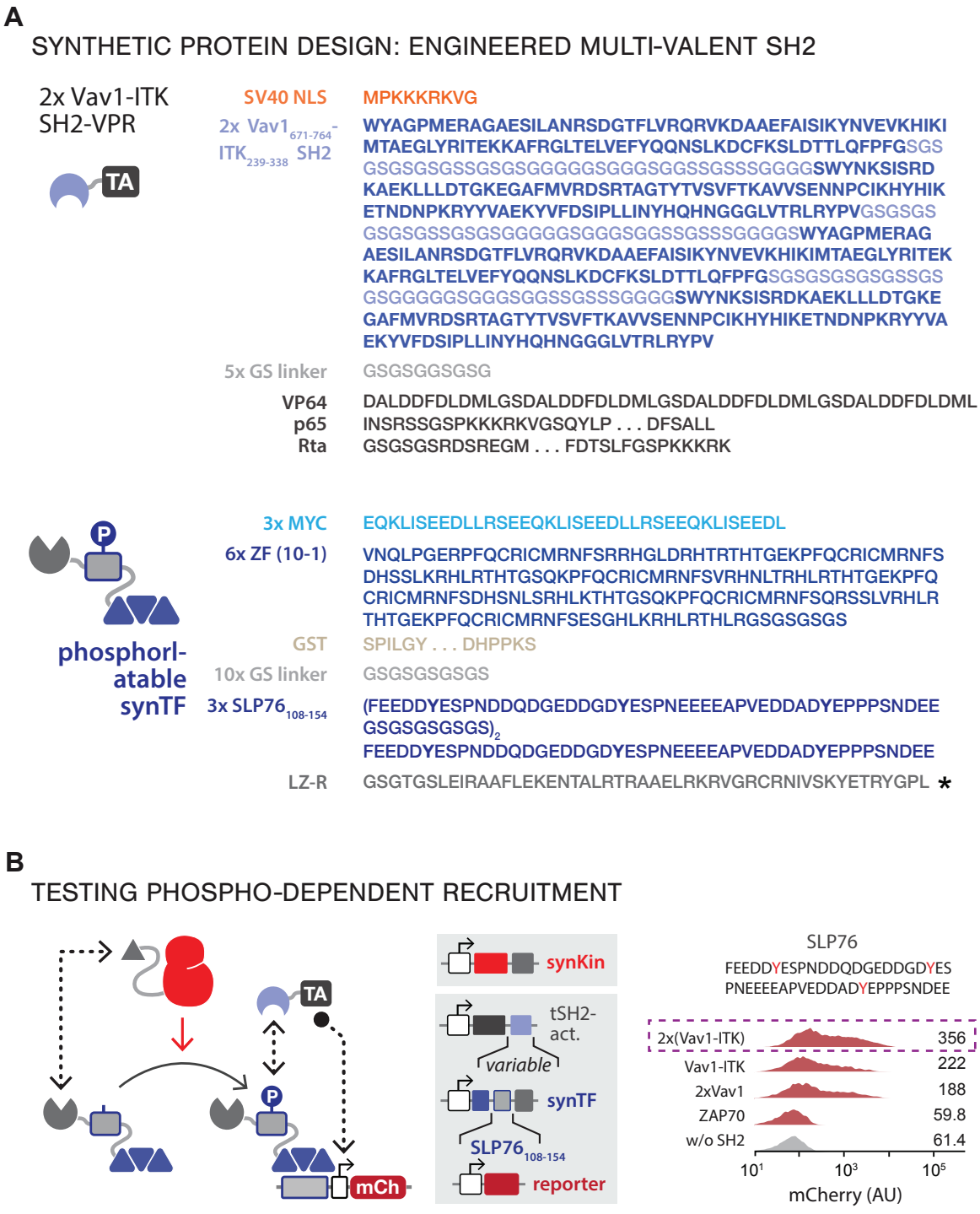

Figure S16. Design of a phopho-depdendent binder for a SLP76-derived pY motif. (a) The design of a transactivator-tSH2 fusion for binding to a 3x $SLP76_{108-154}$ motif, which contains an SV40 NLS, VPR, and a 2x repeat of a synthetic Vav1-ITK SH2 fusion. **(b)** Assessment of pY-SLP76-motif-dependent tSH2 recruitment using the reporter system. The same reporter system used in **figure S15** was employed to evaluate the interaction between synthetic SH2 domains and 3x $SLP76_{108-154}$. Following phosphorylation by synKin, the binding capabilities of various synthetic SH2 domains with 3x $SLP76_{108-154}$ were examined by measuring the mCherry reporter expression. Geometric means for phosphorylation are shown beside the histograms. The optimized synthetic tSH2 chosen for later use in circuit construction is indicated with the purple box.

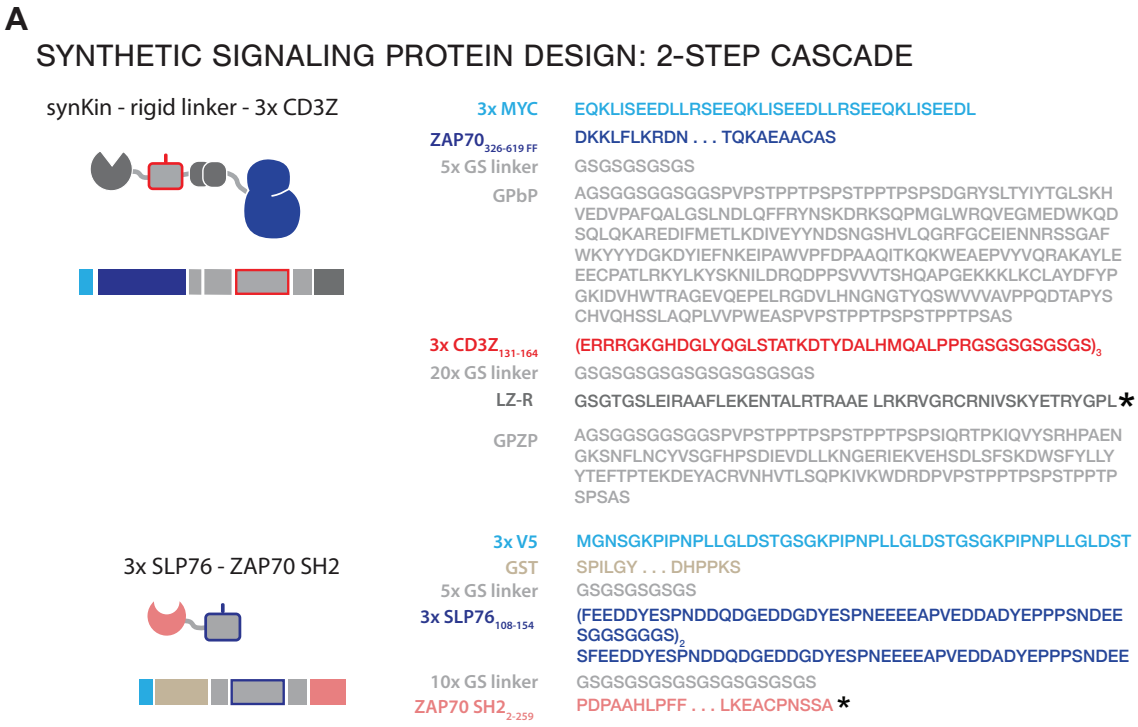

Figure S17. Design and optimization of signaling proteins to interconnect phosphorylation cycles. (a) The middle substrate features a 3x MYC tag, synKin, 3x CD3Z substrate motif, and LZ-R. A rigid linker domain is inserted between synKin and CD3Z to avoid cis-phosphorylation and GS linkers are inserted between the ITAM and the LZ. The SH2-substrate protein features a 3x V5 epitope tag, GST, 3x SLP76-dervied substrate motif, and 2x ZAP70 SH2. **(b)** Optimizing the PC rigid linker to limit cis-phosphorylation. Interconnected two-step circuit schematic. The placement of a rigid linker protein betweeen the kinase domain and substrate motif within the PC is designed to limit intramolecular phosphorylation. Proteins are expressed on three plasmids (grey boxes). **(c)** Testing the effects of rigid linkers on cis phosphorylation. Phosphorylation levels were measured for configurations where the PC contained different rigid linkers or a flexible linker, with and without the upstream synKin. Dotted lines indicate mean background phosphorylation levels. The purple box indicates the rigid linker selected for further engineering.

A

cycle phosphorylation

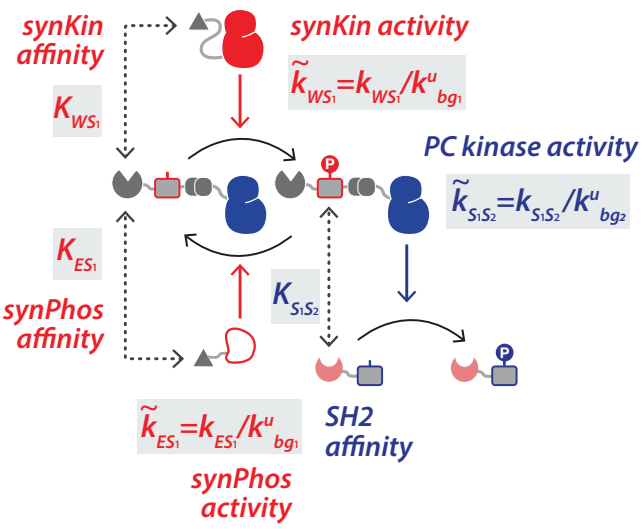

background phosphorylation

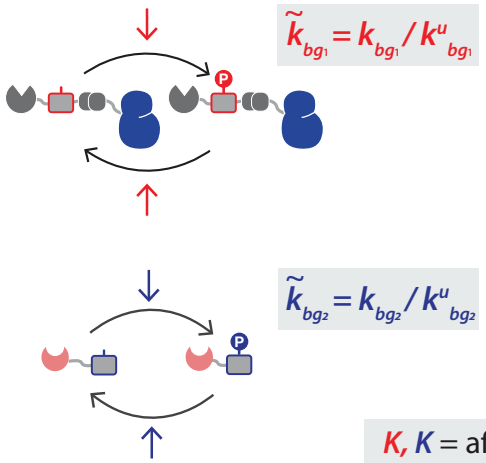

K, K = affinity
$\tilde{k}$, $\tilde{k}$ = norm. rate

B

FITTING DATA FOR TWO-STEP CIRCUIT

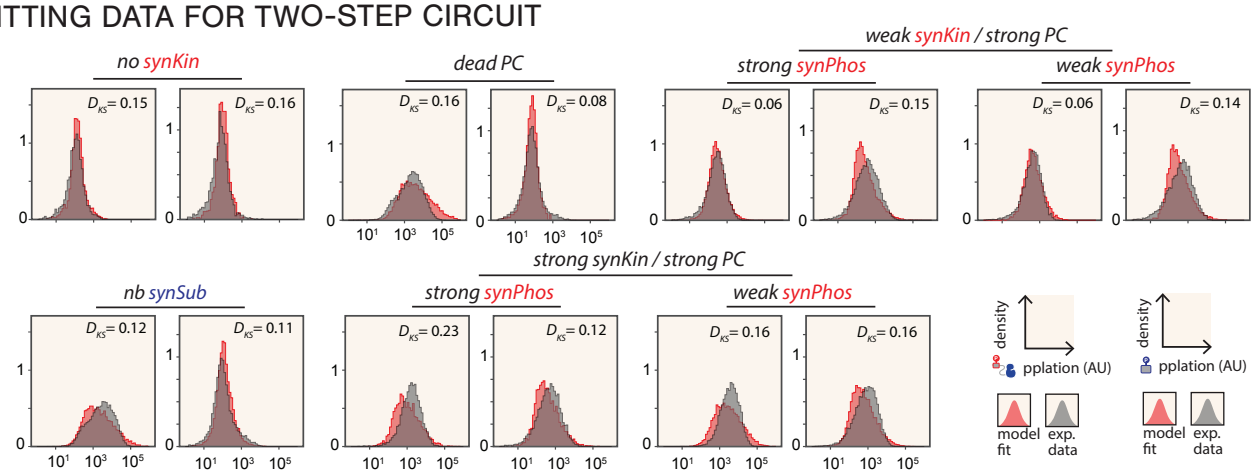

C

MODEL PARAMETER FITTING

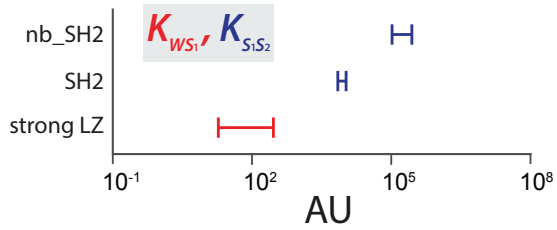

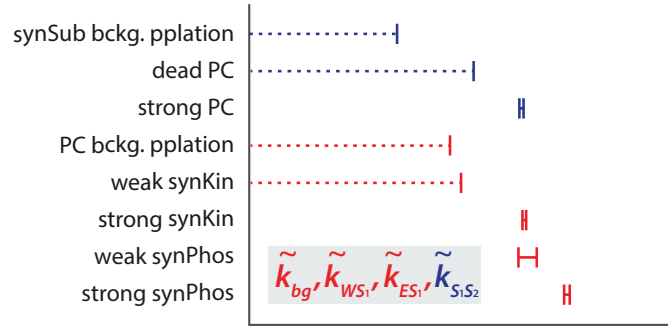

K		K_{min}		K_{max}		in vitro
AU	K_d	AU	K_d	AU	K_d	
$1.5x10^5$	1	$1.0x10^5$	$6.8x10^{-1}$	$2.8x10^5$	1.9	N.A.
$8.0x10^3$	$5.4x10^{-2}$	$7.1x10^3$	$4.8x10^{-2}$	$1.1x10^4$	$7.5x10^{-2}$	$5.0x10^{-2}$
41	$2.8x10^{-4}$	17	$2.1x10^{-3}$	$2.9X10^2$	$3.5x10^{-2}$	$2.8x10^{-4}$

$\tilde{k}$	$\tilde{k}_{min}$	$\tilde{k}_{max}$
$2.4x10^{-4}$	$<10^{-6}$	$1.6x10^{-3}$
$4.6x10^{-4}$	$<10^{-6}$	$4.7x10^{-2}$
$7.4x10^{-1}$	$6.6x10^{-1}$	$8.1x10^{-1}$
$3.7x10^{-3}$	$<10^{-6}$	$9.2x10^{-3}$
$1.3x10^{-3}$	$<10^{-6}$	$2.0x10^{-2}$
$8.6x10^{-1}$	$7.7x10^{-1}$	$9.3x10^{-1}$
$9.5x10^{-1}$	$6.3x10^{-1}$	1.6
6.9	6.1	8.0

Figure S18. Fitting paramaters for the two-step phosphorylation circuit. (a) Parametrization for the activity for both synKin and synPhos, binding affinity for the LZs between synKin/PC and synPhos/PC, and the binding affinity between phosphorylated CD3Z and ZAP70 $SH2_{2\text{-}254}$. Similar to **figure S10**, all activity terms are normalized by the background dephosphorylation rate for fitting. **(b)** Goodness of fit for the two-step phosphorylation circuit. The comparison between experimental and fitted phosphorylation levels for both substrates is shown for all the circuit configurations in **Figure 2B**. K-S was calculated for each set of comparisons between experimental and fitting data and D_{KS} is shown on the top-right of each group of histograms. **(c)** Summary of thermodynamic model parameters. The two-sided error bars and the parameters are calculated and plotted the same way as **figure S12.**

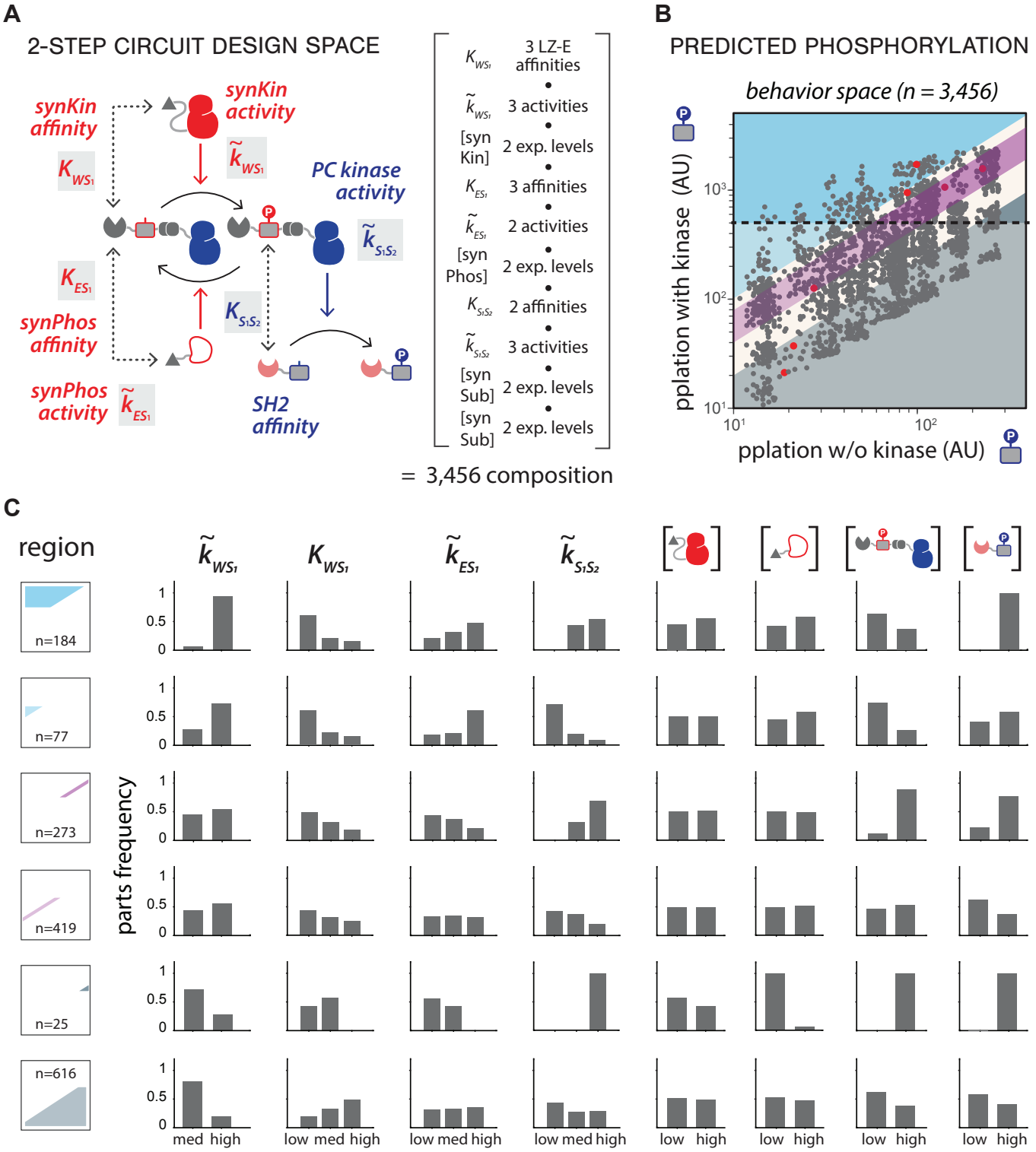

Figure S19. Exploring the design basis of behavior space for coupled phosphorylation cycles. **(a)** Defining configuration space. Part variants were modeled for all part-allowed configurations of the two-step phosphorylation circuit, resulting in a final set of 3,456 compositions. **(b)** Predicted behavior space. The behavior space is divided into 6 regions based on phosphorylation of the second synSub. **(c)** Parameter frequency analysis for the 6 regions of circuit behavior space. The number of compositions in each region is labeled in the icon for each region (left).

A

SYNTHETIC SIGNALING PROTEIN DESIGN: RECEPTORS

signal peptide	MAWTSLILSLLALCSGASS
FLAG	DYKDDDDK
FRB*	LEMWHEGLEEASRLYFGERNVKGMFEVLE **P** LHAMMERGPQTLKETSFNQA YGRDLMEAQEWCRKYMKSGNVKDLLQAWDLYYHVFRRISK
GS-CD28TM-GS	TRSSGGSGGGGSGLVVVAGVLFCYGLLVTVALCVENLSSGGSGGSGG
$ABL_{228-540\ FF}$	DKKLFLKRDNL . . . CYYSLASKVE

signal peptide	MAWTSLILSLLALCSGASS
V5	GKPIPNPLLGLDST
FKBP	MGVQVETISPGDGRTFPKRGQTCVVHYTGMLEDGKKFDSSRDRNKPFKFM LGKQEVIRGWEEGVAQMSVGQRAKLTISPDYAYGATGHPGIIPPHATLVFDVE LLKLE
GS-CD28TM-GS	TRSSGGSGGGGSGLVVVAGVLFCYGLLVTVALCVENLSSGGSGGSGG
LZ-E	GSITIRAAFLEKENTALRTELAELEKEVGRCENIVSKYETRYGPL
GS-CD28TM_M3-GS	TRSSGGSGGGGSGFLVLVVVGGVLACYSLLVTVAFIIFLVTRSSGGSGGGSG
GS-CD28TM_M4-GS	TRSSGGSGGGGSGFWVLVVVGGVLALLLLLVLVAFIIFWVTRSSGGSGGGSG

B

RECEPTOR OPTIMIZATION

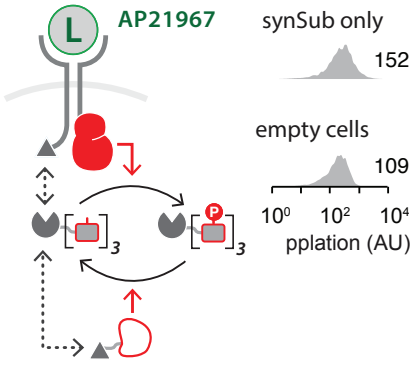

C

OPTIMIZING LINKER LENGTH

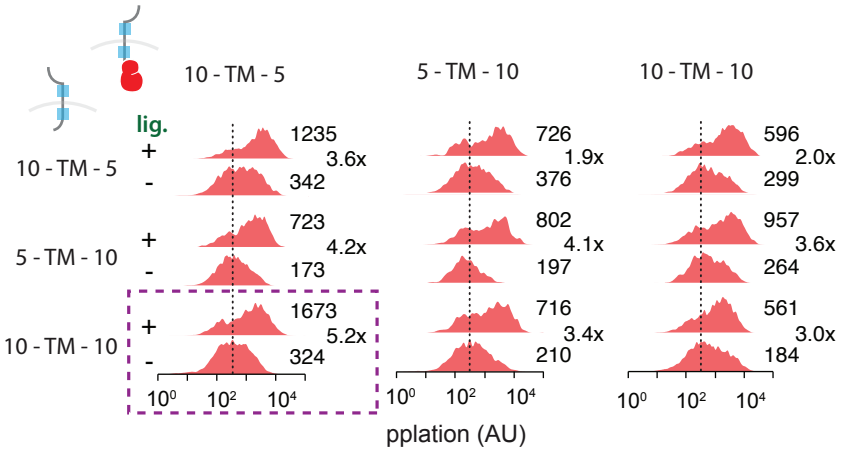

D

OPTIMIZING TRANSMEMBRANE MOTIF

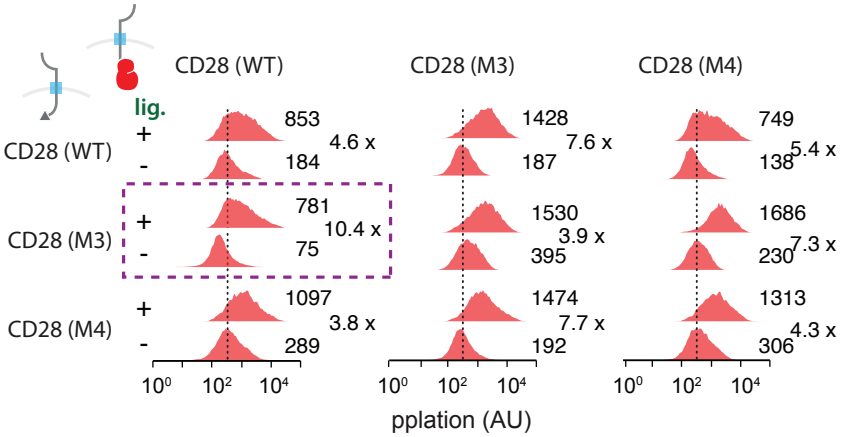

Figure S20. Receptor design optimization for the phospho-sensor circuit. (a) The kinase domain and LZ from a synKin is appended to two receptor chains that are fused with membrane-localized FKBP and FRB* (K2095P, bold grey) domains. The FRB* chain has an extracellular FLAG epitope tag and C-terminal kinase domain. The FKBP features an extracellular V5 epitope tag and a LZ-E at the C terminus. Both chains feature a CD28 TM flanked by 10x GS linkers and a signal peptide from IgGλ. **(b)** Design for the phospho-sensor circuit. The histograms to the right show background phosphorylation for empty cells and cells transfected with synSub only. **(c)** Flexible GS linkers before and after the TM for both receptor chains were combinatorially tested to identify linker lengths that yield high fold- change of ligand-inducible phosphorylation. Three linker lengths were tested for each receptor chain. Phosphorylation levels were measured for each combination with or without the addition of ligand. Geometric means are indicated to the right of the histograms, and fold change was calculated by dividing ligand-induced phosphorylation by uninduced. Black dotted lines indicate the geometric mean of phosphorylation for blank cells. The purple box indicates linker combinations with the highest ligand-inducible fold change in phosphorylation. **(d)** Mutations in the TM for both receptor chains were tested to identify TM combinations that yield high fold change ligand-inducible phosphorylation. Sequence details for the TMs are shown in **figure S20A**. TM variants for the FRB*-synKin chain were tested against variants in the FKBP-LZ-E. Phosphorylation levels and fold change values were calculated as before. Purple box indicates the TM combinations with the highest fold change.

A

SYNTHETIC PROTEIN DESIGN: LLPS REPORTER

mCherry-PopZ

mCherry MVSKGEEDNMAIIKEFMRFKVHMEGSVNG
HEFEIEGEGEGRPYEGTQTAKLKVTKGGPL
PFAWDILSPQFMYGSKAYVKHPADIPDYLK
LSFPEGFKWERVMNFEDGGVVTVTQDSSL
QDGEFIYKVKLRGTNFPSDGPVMQKKTMG
WQASSERMYPEDGALKGEIKQRLKLKDGG
HYDAEVKTTYKAKKPVQLPGAYNVNIKLDIT
SHNEDYTIVEQYERAEGRHSTGGMDELYK

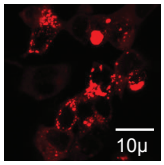

10x GS linker GSGSGSGSGSGSGSGSGSGS

popZ (24-177) DDAPAEPAAEAAPPPPPEPEPEPVSFDDEVLELTDPIAPEPELPPL
ETVGDIDVYSPPEPESEPAYTPPPAAPVFDRDEVAEQLVGVSAASA
AASAFGSLSSALLMPKDGRTLEDVVRELLRPLLKEWLDQNLPRIV
ETKVEEEVQRISRGRGA

SynSub
EGFP-3xCD3Z-LZ-R

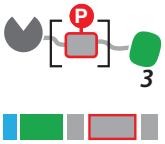

3x MYC EQKLISEEDLLRSEEQKLISEEDLLRSEEQKLISEEDL

EGFP VSKGEELFTGVVPILVELDGDVNGHKFSVSGEGEGDATYGKLTLKFIC
TTGKLPVPWPTLVTTLTYGVQCFSRYPDHMKQHDFFKSAMPEGYVQ
ERTIFFKDDGNYKTRAEVKFEGDTLVNRIELKGIDFKEDGNILGHKLEY
NYNSHNVYIMADKQKNGIKVNFKIRHNIEDGSVQLADHYQQNTPIGD
GPVLLPDNHYLSTQSALSKDPNEKRDHMVLLEFVTAAGITLGMDELYK

10x GS-PKI-NES GGSSGSGGSSSGGSGSRNSNELALKLAGLDINKGS

3x CD3Z$_{131-164}$ (ERRRGKGHDGLYQGLSTATKDTYDALHMQALPPRGSGSGSGSGS)$_3$

10x GS linker GSGSGSGSGSGSGSGSGSGS

LZ-R GSGTGSLEIRAAFLEKENTALRTRAAELRKRVGRCRNIVSKYETRYGPL

tSH2-
mCherry-PopZ

ZAP70 tSH2$_{2-259}$ PDPAAHLPFFYGSISRAEAEEHLKLAGMADGLFLLRQCLRSLGGYVL
SLVHDVRFHHFPIERQLNGTYAIAGGKAHCGPAELCEFYSRDPDGLP
CNLRKPCNRPSGLEPQPGVFDCLRDAMVRDYVRQTWKLEGEALEQ
AIISQAPQVEKLIATTAHERMPWYHSSLTREEAERKLYSGAQTDGKFLL
RPRKEQGTYALSLIYGKTVYHYLISQDKAGKYCIPEGTKFDTLWQLVEY
LKLKADGLIYCLKEACPNSSA

mCherry MVSKGEED...GMDELYK

10x GS linker GSGSGSGSGSGSGSGSGSGS

PopZ (24-177) DDAPAEPAAEAAPPPPPEPEPEPVSFDDEVLELTDPIAPEPELPPL
ETVGDIDVYSPPEPESEPAYTPPPAAPVFDRDEVAEQLVGVSAASA
AASAFGSLSSALLMPKDGRTLEDVVRELLRPLLKEWLDQNLPRIV
ETKVEEEVQRISRGRGA

C

EGFP/mCherry
COLOCALIZATION

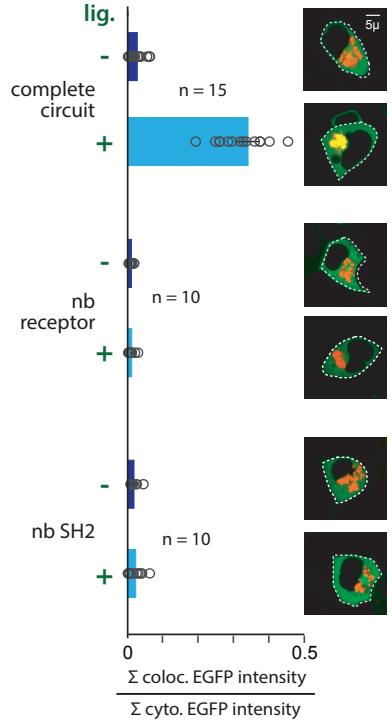

B

CONDENSATE REPORTER WORKFLOW

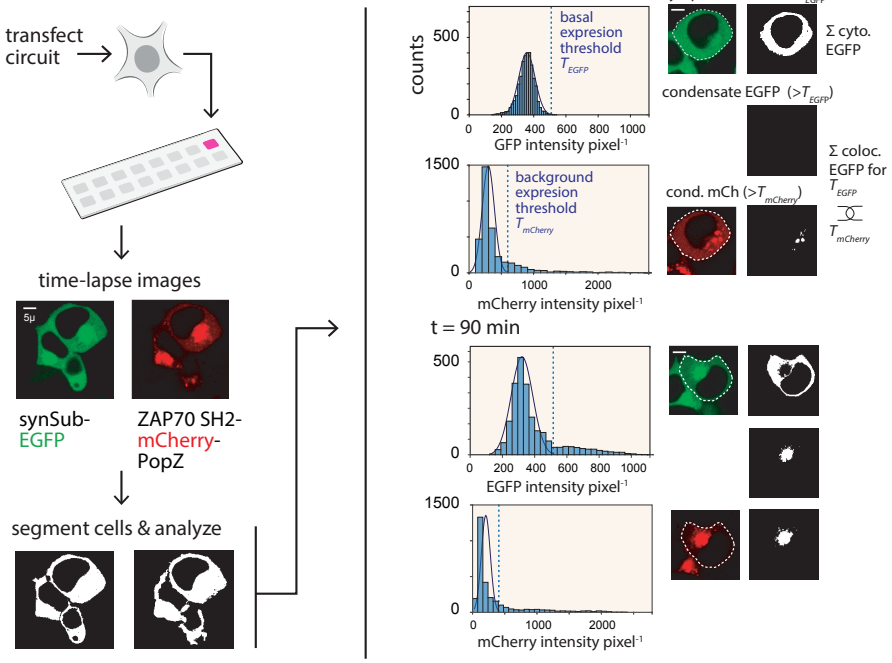

D

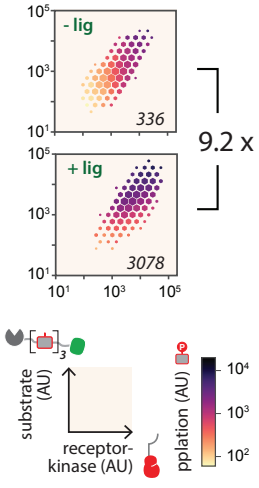

Figure S21. Condensate co-localization reporter design. (a) The reporter uses a synSub design in which GST is replaced wtih an EGFP (see **fig. S4**). Condensates were fomed using an mCherry-PopZ tag fused to a 2x ZAP70 $tSH2_{2\text{-}259}$ domain. Expression of the PopZ-mCherry fusion alone in HEK293T cells results in spontaneous formation of cytoplasmic condensates (top right). **(b)** Workflow for time-lapse microscopy and data processing (see **Materials and Methods**). Left: transfected HEK293T cells are loaded into an multi-well chamber slide and imaged using time-lapse microscopy. Left-middle: single-cell segmentation is performed for both EGFP and mCherry channels to identify single-cell masks and trajectories. Right: To assess EGFP/mCherry co-localization, masks (white dotted line) were used to quantitate subcellular fluorescence for both colors. The resulting pixel intensity distribution was fit to a normal distribution (blue histogram) and the threshold for the condensate (dotted line) is placed at the 99th quantile (T_{EGFP}, $T_{mCherry}$). EGFP pixel intensities below T_{EGFP} (cytoplasmic EGFP white mask) are summed to calculate cytoplasmic intensity. mCherry pixel intensities above $T_{mCherry}$ are considered part of the condensate and used as a mask (condensate mCherry mask) to quantitate overlappling EGFP pixel intensity for pixels > T_{EGFP} (condensate EGFP mask). Representative images from the beginning (t=0 min) and the end (t=80 min) of the time-lapse experiment are shown in **Figure 3C**. **(c)** EGFP/mCherry co-localization is measured for deficient circuits and compared with the full circuit, error bars indicated mean values ± SEM. Number of replicates are labelled on top of each group. Bottom, EGFP and mCherry merged images are shown for representative single cells, with the cell boundaries that were determined by custom segmentation software represented as dotted white outlines (see **Materials and Methods**). **(d)** Phosphorylation level was measured in the condensate reporter circuit with or without the addition of ligand. HHH maps are used to plot the component expression and phosphorylation. The geometric mean for phosphorylation is noted in the bottom right of the maps and the fold change is labeled on the right.

A

CIRCUIT DEACTIVATION WITHOUT synPhos

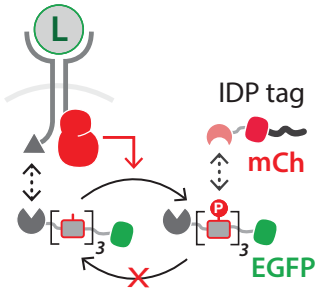

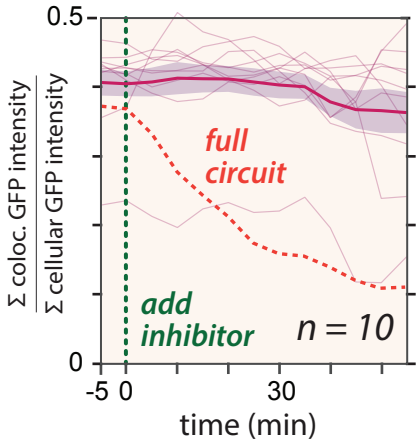

B

FITTING ACTIVATION & DEACTIVATION DYNAMICS

Step 1: receptor dimerization

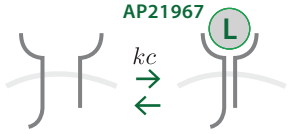

$$\frac{d[Receptor_{dim}]}{dt} = kc \cdot (1 - [Receptor_{dim}])$$

Step 2: synSub phosphorylation

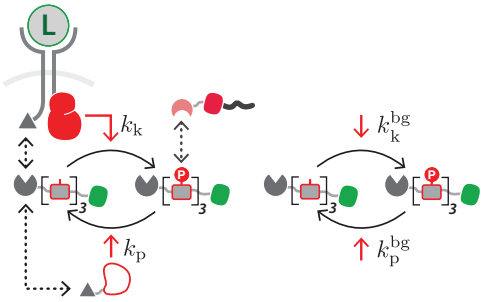

$$\frac{d[GFP_{conden.}]}{dt} = k_k \cdot [Receptor_{dim}] - (k_p + k_p^{bg}) \cdot [GFP_{cond}] + k_k^{bg}$$

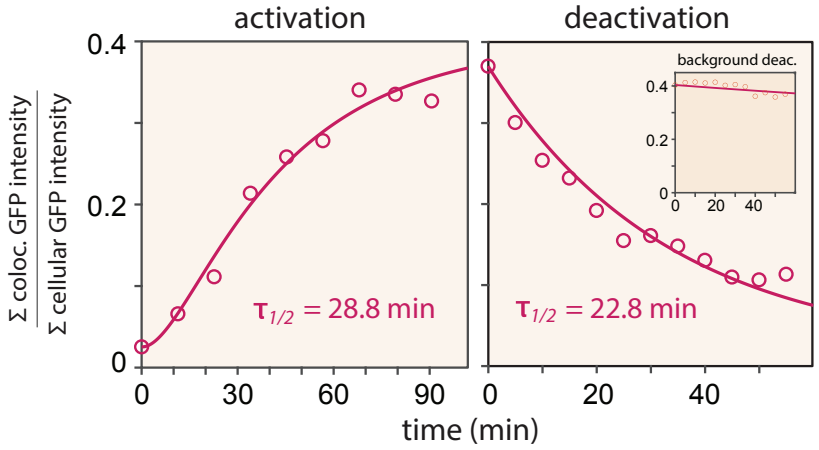

k_k	2.5x10^{-4} s^{-1}
k_p	4.5x10^{-4} s^{-1}
k_k^{bg}	8.3x10^{-5} s^{-1}
k_p^{bg}	4.3x10^{-5} s^{-1}

	kinetic	thermo.
$\frac{k_k}{k_{bg}}$	40	93
$\frac{k_p}{k_{bg}}$	54	101
$\frac{k_k}{k_p}$	0.56	0.92

C

COMPARISON OF SYNTHETIC PATHWAY WITH NATIVE PATHWAY DYNAMICS

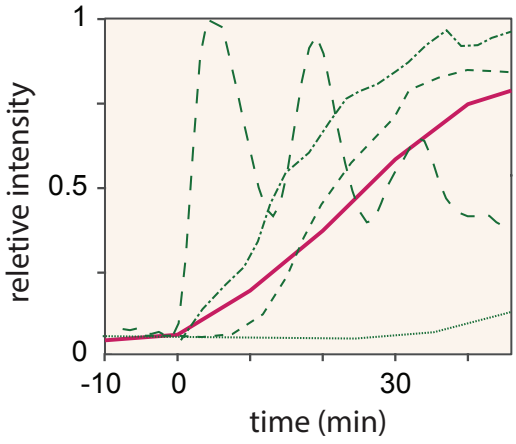

- EGFR ⟶ ERK — *Shankaran, H., et al 2009* — τ 1/2 = 2 min
- RTK ⟶ JAK/STAT — *Chen, HC., et al 2010* — τ 1/2 = 15 min
- TGFb ⟶ SMAD4 — *Labibi, B., et al 2020* — τ 1/2 = 20 min
- synthetic pathway — τ 1/2 = 28.8 min
- WNT ⟶ β-catenin — *Kafri, P., et al 2016* — τ 1/2 = 65 min

Figure S22. Obtaining kinetic parameters for the phospho-sensor circuit. (a) The off kinetics of the phospho-sensor circuit measured with synPhos absent. The red dashed line the mean deactivation data of the complete circuit shown in **Figure 3C**. For the circuit lacking synPhos, trajectories for 10 cells are shown (light pink lines), with mean values (thick pink line) ± SEM (shaded pink band). Green dashed line indicates the addition of ABL inhibitor imatinib mesylate (10 μM). **(b)** Kinetic model of activation and deactivation dynamics of the phospho-sensor. ODEs are used to account for receptor activation and phospho-dependent condensate co-localization. Bottom left, fitting experimental data (circles) from **Figure 3C** and **A** to the model (pink line) and $\tau_{1/2}$ values were calculated from the fitted model paramaters. Bottom right, rate constants were obtained from fitting for activation and deactvation data. Background-normalized rate constants are compared with values obtained from fitting in **S18C**. **(c)** Activation kinetics for native pathways. Localization reporter data from native signaling pathways are plotted using data obtained from the cited references to compare with the dynamics of the ligand-inducible phosphorylation circuit. All activation curves are normalized to the maximum output signal. $\tau_{1/2}$ values are estimated based on data from the indicated references.

A

SYNTHETIC SIGNALING PROTEIN STRUCTURE: PHOSPHO-ACTIVATED synTF

SV40 NLS	MPKKKRKVG
2x Vav1$_{671-764}$-ITK$_{239-338}$ SH2	WYAGPMERAGAESILANRSDGTFLVRQRVKDAAEFAISIKYNVEVKHIKI MTAEGLYRITEKKAFRGLTELVEFYQQNSLKDCFKSLDTTLQFPFGSGS GSGSGSGSSGSGSGGGGGSGGGSGGSSGSSSGGGGSWYNKSISRD KAEKLLLDTGKEGAFMVRDSRTAGTYTVSVFTKAVVSENNPCIKHYHIK ETNDNPKRYYVAEKYVFDSIPLLINYHQHNGGGLVTRLRYPVGSGSGS GSGSGSSGSGSGGGGSGGGSGGSSGSSSGGGGSWYAGPMERAG AESILANRSDGTFLVRQRVKDAAEFAISIKYNVEVKHIKIMTAEGLYRITEK KAFRGLTELVEFYQQNSLKDCFKSLDTTLQFPFGSGSGSGSGSGSSGS GSGGGGGSGGGSGGSSGSSSGGGGSWYNKSISRDKAEKLLLDTGKE GAFMVRDSRTAGTYTVSVFTKAVVSENNPCIKHYHIKETNDNPKRYYVA EKYVFDSIPLLINYHQHNGGGLVTRLRYPV
5x GS linker	GSGSGGSGSG
VP64	DALDDFDLDMLGSDALDDFDLDMLGSDALDDFDLDMLGSDALDDFDLDML
p65	INSRSSGSPKKKRKVGSQYLP...DFSALL
Rta	GSGSGSRDSREGM...FDTSLFGSPKKKRK

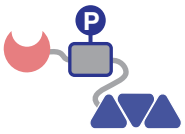

3x MYC	EQKLISEEDLLRSEEQKLISEEDLLRSEEQKLISEEDL
6x ZF (10-1)	VNQLPG . . . SSGSGS
GST	SPILGY...DHPPKS
10x GS linker	GSGSGSGSGS
3x SLP76$_{108-154}$	SFEEDDYESPNDDQDGEDDGDYESPNEEEEAPVEDDADYEPPPSNDEE SGGSGGGSSFEEDDYESPNDDQDGEDDGDYESPNEEEEAPVEDDADY EPPPSNDEESGGSGGGSSFEEDDYESPNDDQDGEDDGDYESPNEEEE APVEDDADYEPPPSNDEE
10xGS linker	GSGSGSGSGSGSGSGSGSGS
ZAP70 tSH2$_{2-259}$	PDPAAHLPFF...LKEACPNSSA

B

TESTING PC NUCLEAR IMPORT/EXPORT FUNCTION

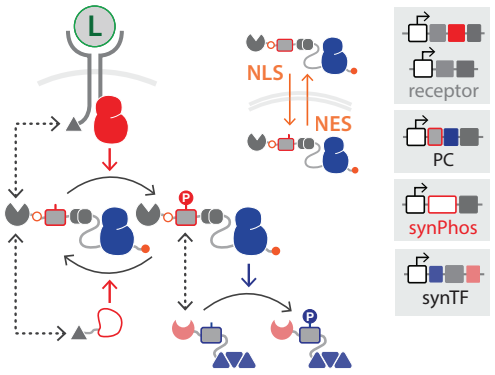

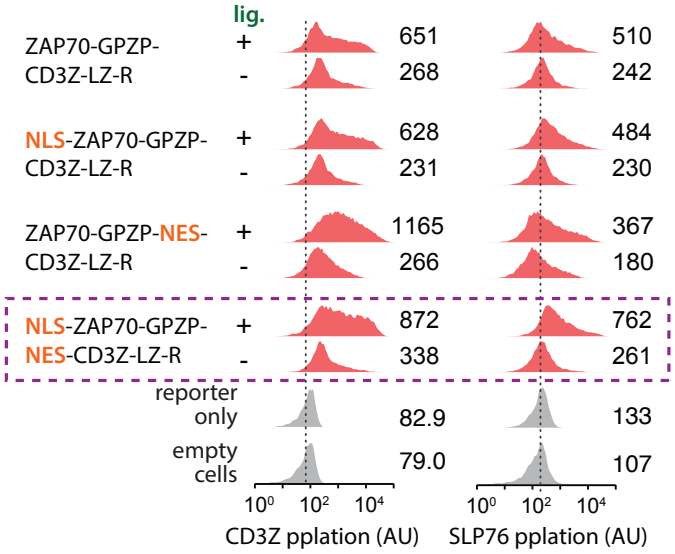

Figure S23. Design of sense-and-respond signalling circuit components. (a) The same design strategy from **figure S17A** was used to connect the phosphorylation of the second substrate to the transcriptional activation (TA) domain. The TA-SH2 fusion features SV40 NLS, VPR, and a double repeat of the synthetic Vav1-ITK SH2, while the synTF-ITAM consists of a 3x MYC epitope tag, SV40 NLS, 10-1 zinc finger array, GST, a 3x SLP76 peptide and LZ-R. **(b)** To enhance signaling from the cell membrane to the nucleus, subcellular localization tags were added to the PC. Dashed lines show the geometric mean of empty cell phosphorylation. The purple box indicates the configuration that was used for sense-and-respond circuit engineering in **Figure 4A**.

A VALIDATION OF SIGNALING PATHWAY DESIGN

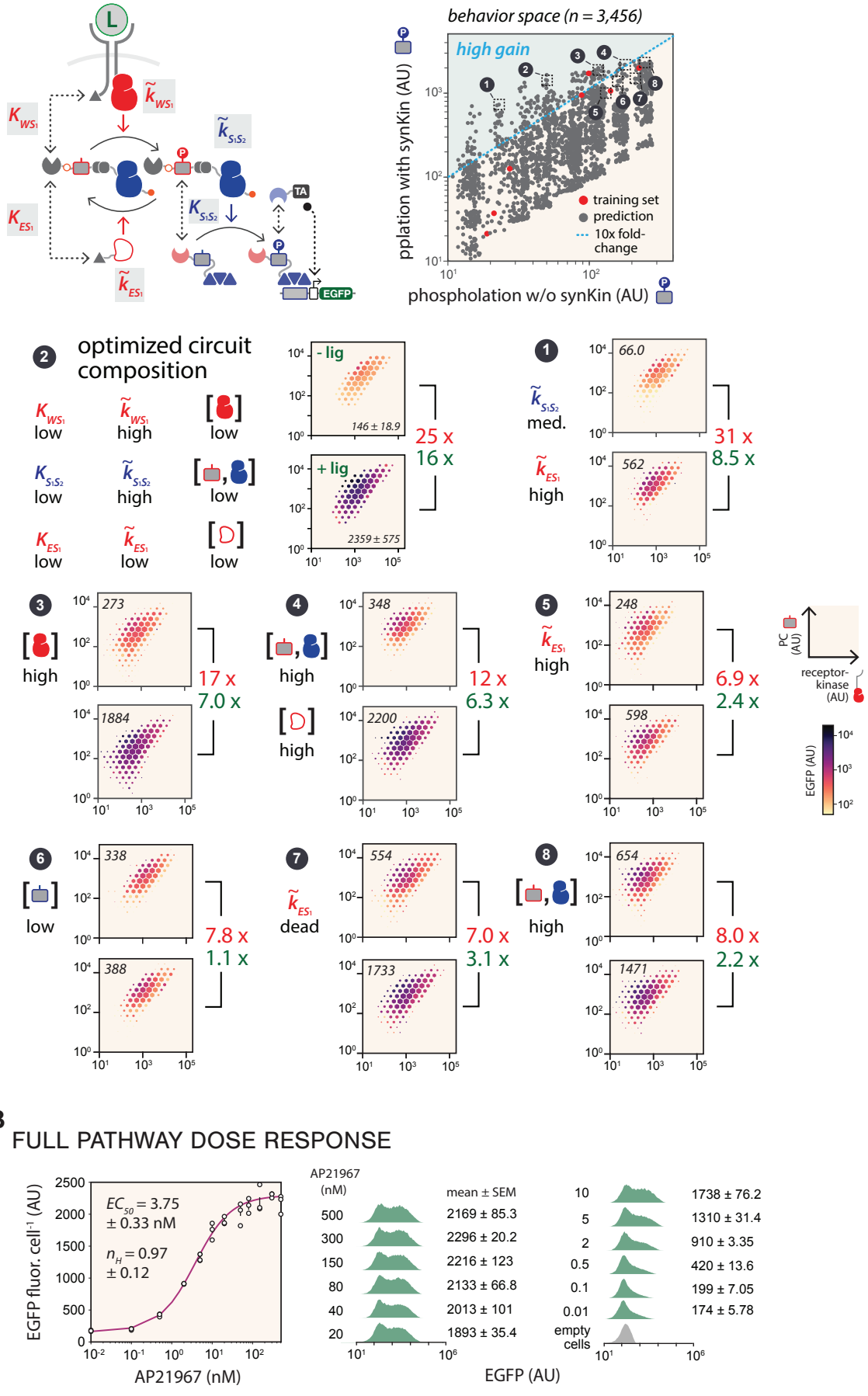

B FULL PATHWAY DOSE RESPONSE

Figure S24. Validating design choices for the sense-and-respond circuit. (a) To test whether the design principle provided by the model prediction from **Figure 2C** can be used to guide sense-and-respond circuit design, all high-gain circuit compositions from **Figure 2C** (#1-4) along with with lower-gain compositions (#5-8) were implemented as part of the sense-and-respond circuit. EGFP expression before and after ligand addition is plotted as HHH plots. The model-predicted fold change for the circuits (red values) and the experimentally-measured EGFP fold-change (green values) are shown to the right of the plots. The composition selected for sense-and-respond circuit engineering (**Fig. 4A**) is plotted on the top left (#2) while non-optimal compositions (#1, 3-8) are plotted below, with specific changes in part composition shown to the left of each set of plots. **(b)** Dose response for composition #2. For each concentration, each circle representing mean EGFP value for one of the three replicates, with error bars representing mean value ± SEM. EC_{50} and n_H were extracted by fitting to equation 150.

A

SYNTHETIC SIGNALING PROTEIN STRUCTURE: TNF-α RECEPTORS

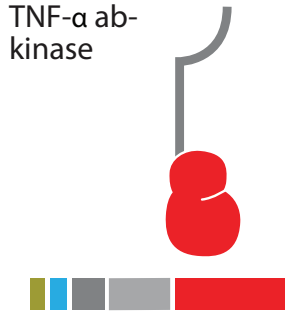

signal peptide	MAWTSLILSLLALCSGASS
FLAG	DYKDDDDK
TNF-α scFv	AEVQLLESGGGLVQPGGSLRLSCAASGFTFSSYAMSWVRQAPGKGLEWV SSISSTGASTTYADSVKGRFTISRDNSKNTLYLQMNSLRAEDTAVYYCAKGG AAFDYWGQGTLVTVSSGGGGSGGGSGGGSTDIQMTQSPSSLSASVGDRV TITCRASQSISSYLNWYQQKPGKAPKLLIYSASYLQSGVPSRFSGSGSGTD FTLTISSLQPEDFATYYCQQANNAPTTFGQGTKVEIKRAA
GS-CD28TM-GS	TRSSGGSGGGSGLVVVAGVLFCYGLLVTVALCVENLSSGGSGGSGG
$ABL_{228-540\ FF}$	DKKLFLKRDNLLIADIELGCGNFGSVRQGVYRMRKKQIDVAIKVLKQGTEKA DTEEMMREAQIMHQLDNPYIVRLIGVCQAEALMLVMEMAGGGPLHKFLVG KREEIPVSNVAELLHQVSMGMKYLEEKNFVHRDLAARNVLLVNRHYAKISDF GLSKALGADDSYYTARSAGKWPLKWYAPECINFRKFSSRSDVWSYGVTMW EALSYGQKPYKKMKGPEVMAFIEQGKRMECPPECPPELYALMSDCWIYKW EDRPDFLTVEQRMRACYYSLASKVE

signal peptide	MAWTSLILSLLALCSGASS
FLAG	DYKDDDDK
TNF-α scFv	AEVQLLESGGGLVQPGGSLRLSCAASGFTFSSYAMSWVRQAPGKGLEWV SSISSTGASTTYADSVKGRFTISRDNSKNTLYLQMNSLRAEDTAVYYCAKGG AAFDYWGQGTLVTVSSGGGGSGGGSGGGSTDIQMTQSPSSLSASVGDRV TITCRASQSISSYLNWYQQKPGKAPKLLIYSASYLQSGVPSRFSGSGSGTD FTLTISSLQPEDFATYYCQQANNAPTTFGQGTKVEIKRAA
GS-CD28TM-GS	TRSSGGSGGGSGLVVVAGVLFCYGLLVTVALCVENLSSGGSGGSGG
LZ-E	GSITIRAAFLEKENTALRTELAELEKEVGRCENIVSKYETRYGPL

B

TNF-α SENSOR DOSE RESPONSE

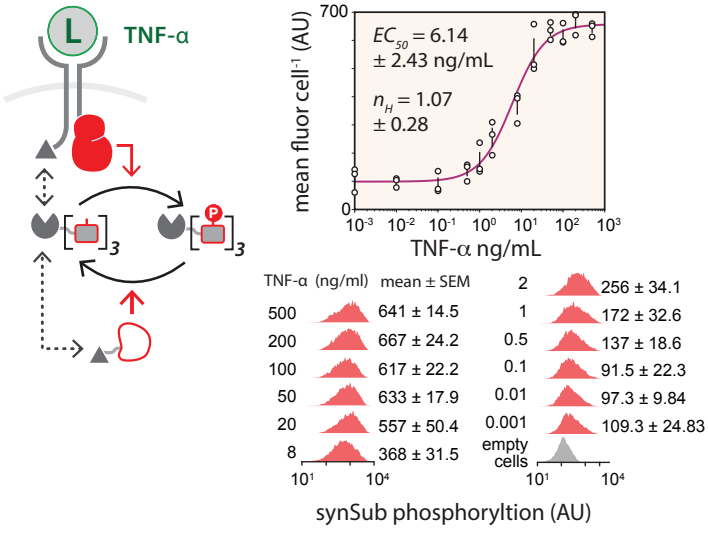

Figure S25. Expand ligand sensing capabilities with a TNF-α sensor module. (a) The FRB*/FKBP domains from the rapalog-sensing receptor pair were swapped for an scFv specific for TNF-α. **(b)** Dose response for circuit depicted in **Figure 4B**. For each concentration, circles mean phosphorylation level for each three replicates, with error bars representing mean values ± SEM. EC_{50} and n_H were extracted by fitting to equation 150.

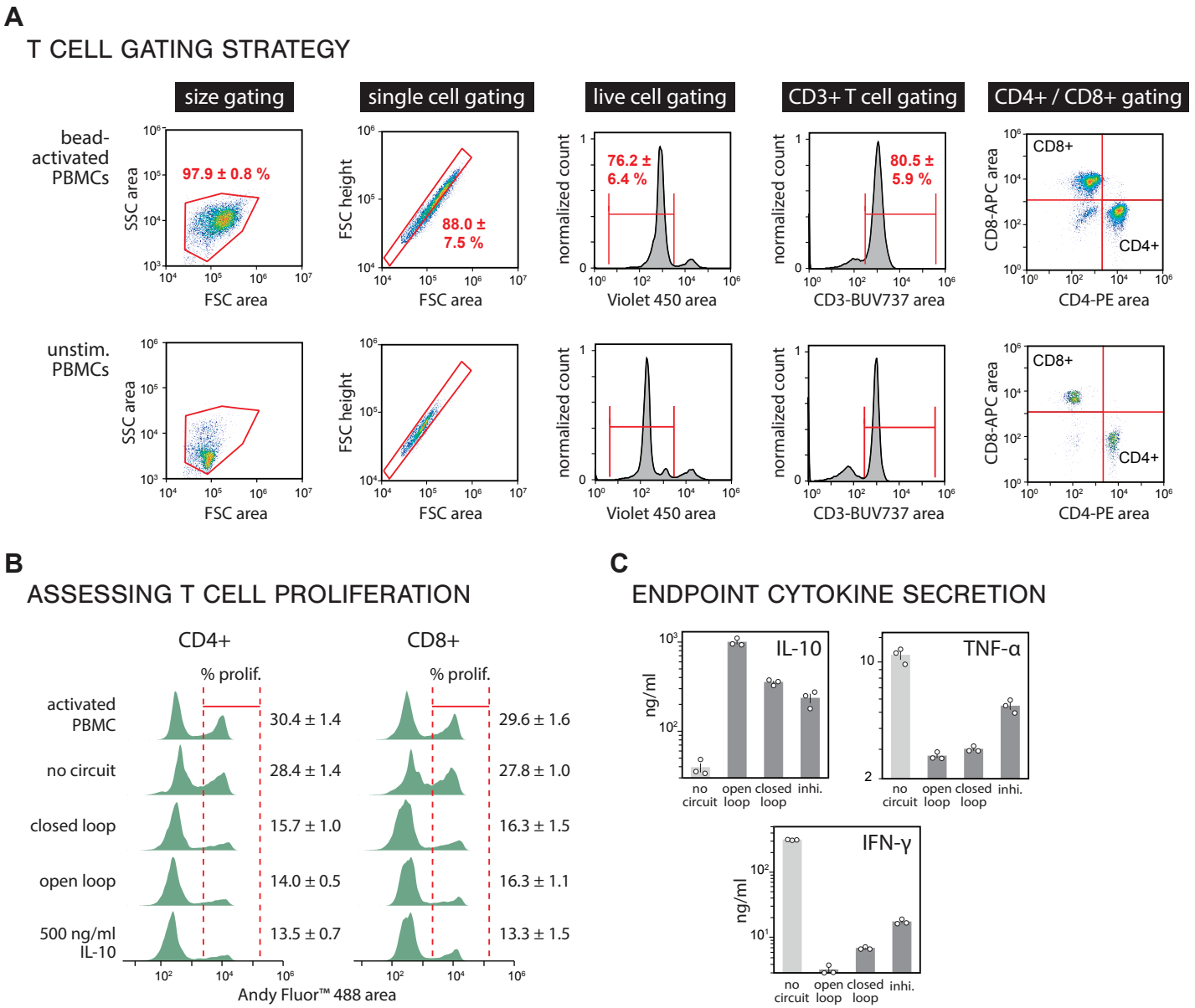

Figure S26. Data processing for PBMC phenotyping. (a) Workflow for processing PBMC flow cytometry data. Similar to HEK293T data processing (**fig. S5**), PBMCs are gated by forward (FSC-A) and side scatter (SSC-A) area for cell population, and single cells are gated by forward scatter height (FSC-H) and area (FSC-A). Live cells are gated using the negative peak of Ghost Dye™ Violet 450 area. T cells are gated using CD3+, then CD4+ area is plotted against CD8+ area to analyze T cell subsets. The top row shows an example of the PBMC sample treated with CD3/CD28 Dynabeads™, while the bottom row shows the profile for untreated PBMCs. Values indicate mean ± SEM for bead-activated samples. **(b)** Quantitating T cell proliferation by EdU assay. At the conclusion of the co-culture time course experiments (60 h) shown in **Figure 4B**, cells were assessed for proliferation. Gated CD4+ and CD8+ subsets are replotted as Andy Fluor™ 488 histograms (see **Materials and Methods** for details). The red gate is used to calculate the percentage of the population that is proliferative. Values indicate the mean ± SEM for n=3 replicates. **(c)** Endpoint cytokine secretion profiles. At the conclusion of the co-culture time course, concentrations for IL-10, TNF-α, and IFN-γ were measured by ELISA for different circuits. Error bars show mean ± SEM for n=3.

MODELING CYTOKINE SECRETION DYNAMICS

NO CIRCUIT

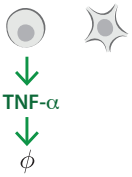

$$\frac{d[TNF\text{-}\alpha]}{dt} = k^{+}_{TNF\text{-}\alpha} - k^{-}_{TNF\text{-}\alpha} \cdot [TNF\text{-}\alpha]$$

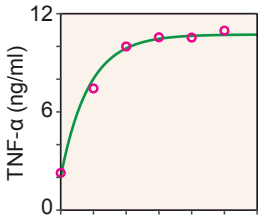

OPEN LOOP

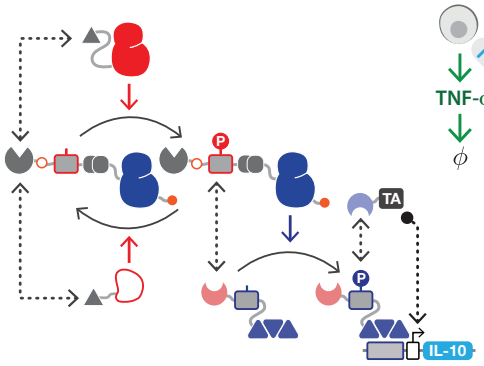

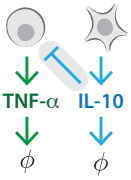

$$\frac{d[Active]}{dt} = k_{\mathrm{k}} + k_{\mathrm{k}}^{\mathrm{bg}} - (k_{\mathrm{p}} + k_{\mathrm{p}}^{\mathrm{bg}}) \cdot [Active]$$

$$\frac{d[IL\text{-}10]}{dt} = k^{+}_{IL\text{-}10} \cdot [Active] - k^{-}_{IL\text{-}10} \cdot [IL\text{-}10]$$

$$\frac{d[TNF\text{-}\alpha]}{dt} = k^{basal}_{TNF\text{-}\alpha} + \frac{k^{+}_{TNF\text{-}\alpha} - k^{basal}_{TNF\text{-}\alpha}}{1 + \frac{[IL\text{-}10]}{K_{IL\text{-}10}}} - k^{-}_{TNF\text{-}\alpha} \cdot [TNF\text{-}\alpha]$$

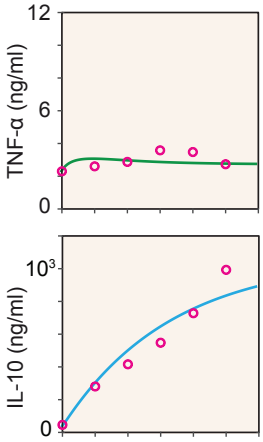

CLOSED LOOP

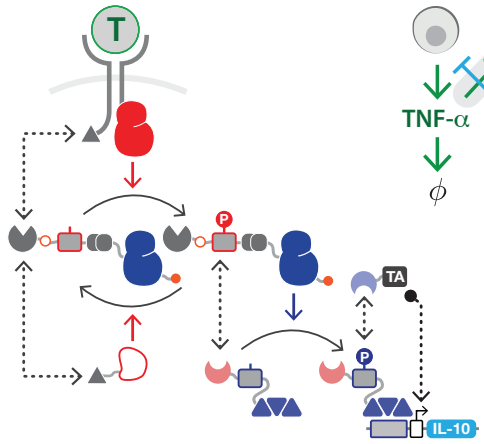

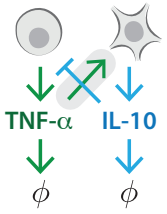

$$\frac{d[Active]}{dt} = k_{\mathrm{k}} \cdot \frac{[TNF\text{-}\alpha]}{[TNF\text{-}\alpha] + K_{TNF\text{-}\alpha}} + k_{\mathrm{k}}^{\mathrm{bg}} - (k_{\mathrm{p}} + k_{\mathrm{p}}^{\mathrm{bg}}) \cdot [Active]$$

$$\frac{d[IL\text{-}10]}{dt} = k^{+}_{IL\text{-}10} \cdot [Active] - k^{-}_{IL\text{-}10} \cdot [IL\text{-}10]$$

$$\frac{d[TNF\text{-}\alpha]}{dt} = k^{basal}_{TNF\text{-}\alpha} + \frac{k^{+}_{TNF\text{-}\alpha} - k^{basal}_{TNF\text{-}\alpha}}{1 + \frac{[IL\text{-}10]}{K_{IL\text{-}10}}} - k^{-}_{TNF\text{-}\alpha} \cdot [TNF\text{-}\alpha]$$

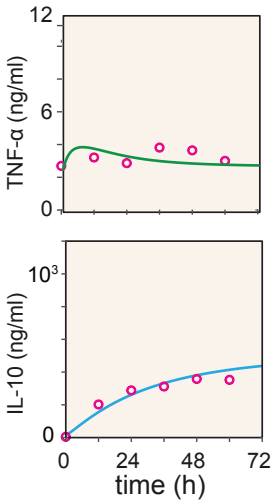

$k^{+}_{TNF\text{-}\alpha}$ = 3 x10^{-4} ng/ml s^{-1}	$k^{+}_{IL\text{-}10}$ = 1.3x10^{-2} ng/ml s^{-1}	$k^{basal}_{TNF\text{-}\alpha}$ = 6.9 x10^{-5} ng/ml·s^{-1}	$K_{TNF\text{-}\alpha}$ = 3.9 ng/ml
$k^{-}_{TNF\text{-}\alpha}$ = 2.7x10^{-5} s^{-1}	$k^{-}_{IL\text{-}10}$ = 6.0x10^{-6} s^{-1}	$K_{IL\text{-}10}$ = 19.2 ng/ml	

Figure S27. Fitting cytokine dynamics in the cytokine control circuit co-culture. (a) Quantitative model describing cytokine secretion dynamics for the transwell culture experiments depicted in **Figure 4B**. ODEs are used to account for changes in receptor activation and cytokine concentration. Left, circuit schematic. Middle, coresponding ODEs. Right, fitting the cytokine secretion data (circles) from **Figure 4B** to the dynamic model (green or blue lines). Bottom, rate constants were obtained from a global fit of the time course data and constrained by TNF-α dose-response curve from **fig. S25B**.

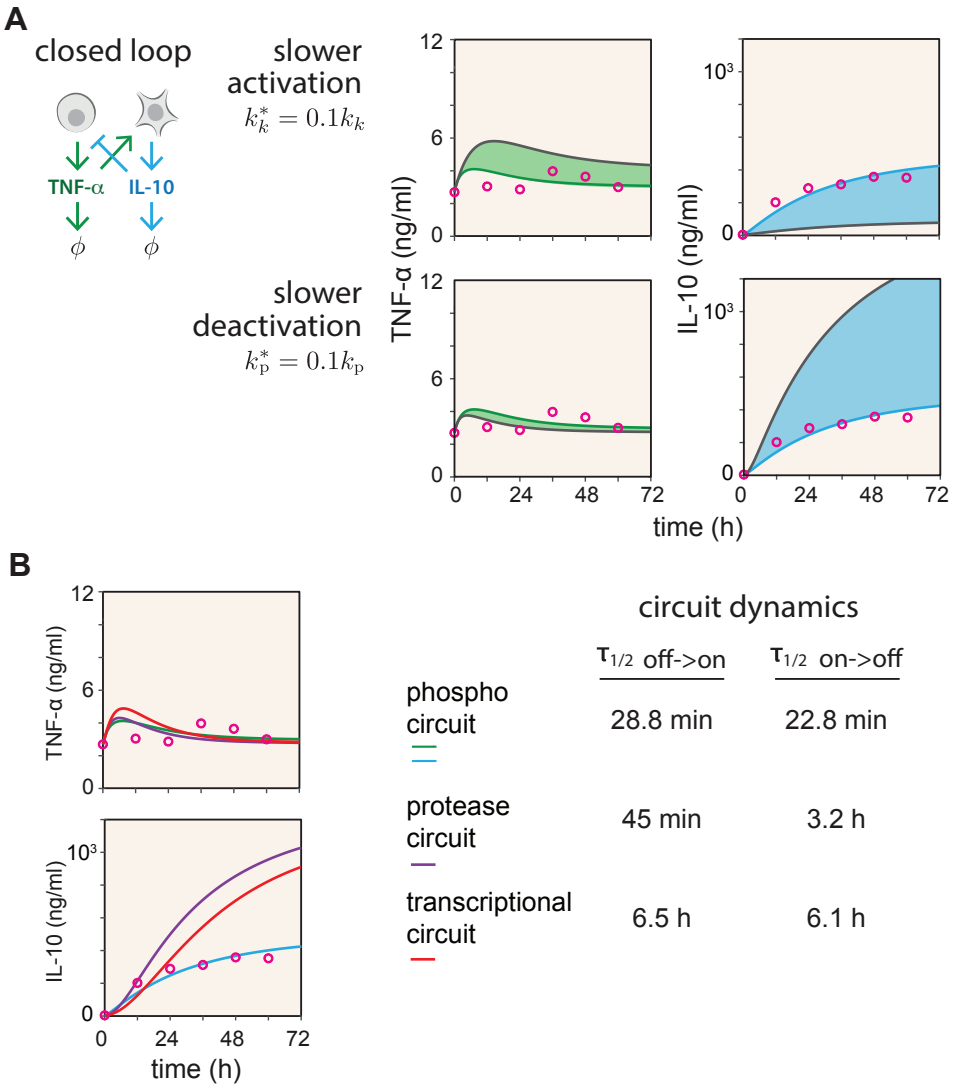

Figure S28. Prediciting cytokine secretion for circuits with slower dynamic profiles. (a) Secretion of TNF-α (green) and IL-10 (blue) for co-culture systems in which sense-and-respond circuits have reduced activation or deactivation rates (*k**). Model-predicted time courses for TNF-α (dark green) and IL-10 (dark blue) are shown for 10-fold lower rates. **(b)** Comparison to simulated systems featuring versions of the circuit depicted in **Figure 4B** that are activated by transcription or proteolysis. Values used in the simulations for proteolysis and transcription are taken from the literature as described in the **Supplementary Text.**

S29

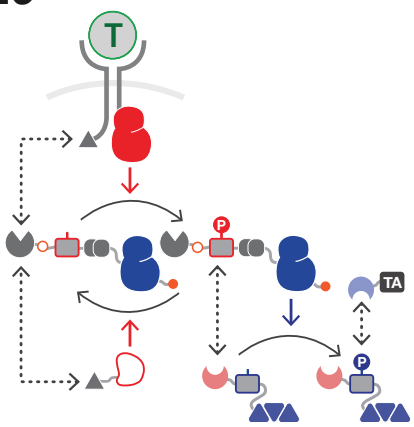

synthetic phosphorylation parts

synthetic components	total # 9-mer peptides	% 9-mer score >0	% 9-mer score >0.328
TNF-α scFv-kinase	615	45.8%	2.9%
TNF-scFv LZ	364	45.2%	1.9%
PC	836	40.6%	1.7%
synPhos	403	48.6%	2.5%
synTF-slp76-SH2	1173	44.6%	1.7%
SH2-VPR	1050	45.2%	0.5%

other signaling parts

CD19 synNotch	801	42.3%	1.1%
CD19 SNIPR	529	40.6%	0.9%
CD19 CAR	570	35.2%	2.4%
TVMVp	230	53.5%	3.9%
TEVp	230	49.6%	4.8%

humanized mAb

Atezolizumab	653	36.7%	2.0%
Pembrolizumab	656	36.6%	0.8%
Ipilimumab	654	39.3%	1.4%

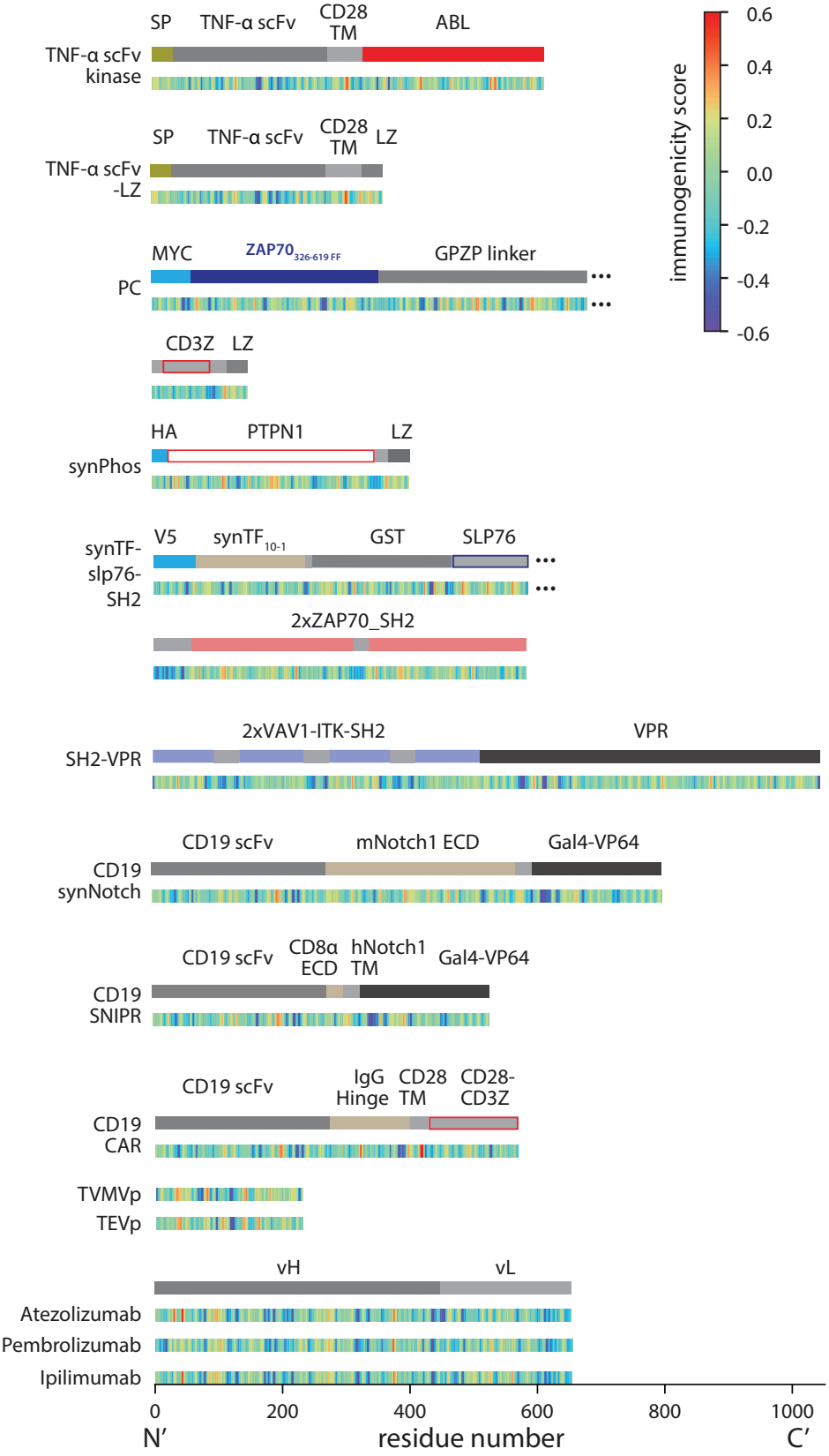

Figure S29. Predicted immunogenicity of cytokine control circuit components compared to other commonly used synthetic signaling parts. T Cell Class I pMHC Immunogenicity tool from the Immune Epitope Database (IEDB) was used to evaluate the immunogenicity scores of all 9-mer peptide sequences within the six engineered proteins in the cytokine control circuit, along with three commonly-used synthetic receptors, two proteases and three FDA-approved fully humanized monoclonal antibodies (mAbs). Subdomains are labelled above the score heatmaps. Protein sizes are indicated by the residue number label on the bottom. A higher immunogenicity score (hotter color) for a peptide indicates that its composition more closely resembles that of immunogenic peptides, and thus indicates a higher probability of eliciting an immune response. A summary of immunogenicity scores of all 9-mer peptide sequences within all synthetic components from this research and other parts is shown in the tables on the left, with the total number of 9-mer peptides, the percentage of 9-mer scores >0, and the percentage of 9-mer scores >0.328 calculated.TVMVp, tobacco vein mottling virus protease. TEVp, tobacco etch virus protease.

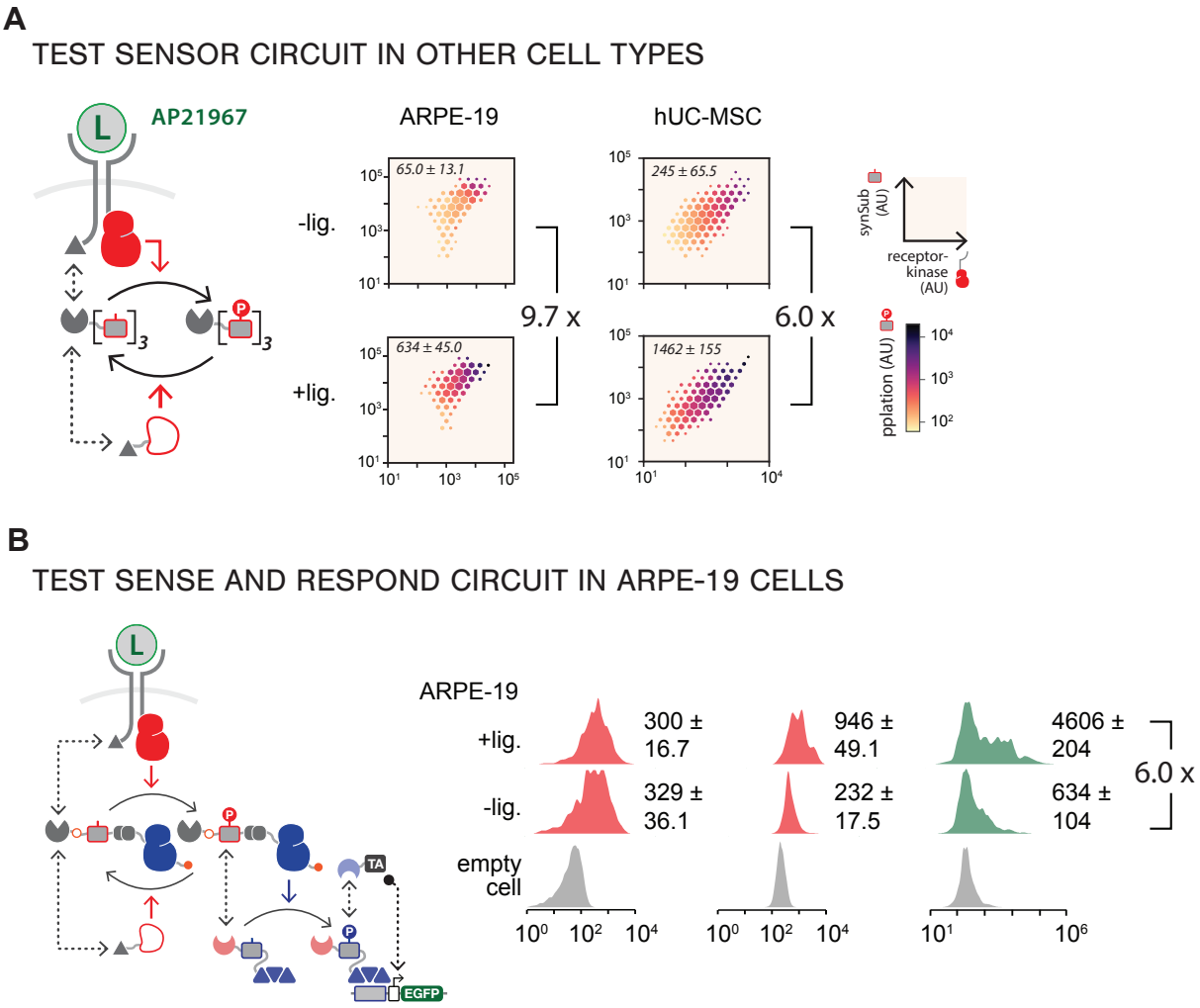

Figure S30. Signaling circuit behavior in therapeutically-relevant cells. (a) Behavior of receptor-coupled sensor circuit in human APRE-19 cells and human UC-MSCs. HHH plots depict flow-cytometry data of the complete sensor circuit from **Figure 3B** in different cell types with 200 nM ligand (+ lig) or a carrier-only control (- lig). Values in each plot indicate mean phosphorylation (AU) ± SEM (n=3). Phosphorylation fold-change values are next to each set of plots. **(b)** Behavior of the sense-and-response signaling circuit in ARPE-19 . PC expression, PC phosphorylation signal and EGFP level were measured. Numbers indicate the geometric mean values (AU) ± SEM (n=3).

Table S1: Plasmid Information

PLASMID#	POSITION 1 (AB)		POSITION 2 (BC)		POSITION 3 (CD)	
	PROMOTER	ORF	PROMOTER	ORF	PROMOTER	ORF
pXY127	*CMV*	3x MYC — GST — 1x $CD3Z_{131-164}$ — LZ-R				
pXY128	*CMV*	3x MYC — GST — 1x $CD3Z_{131-164}$ — LZ-R(E)				
pXY129	*CMV*	3x MYC — GST — 3x $CD3Z_{131-164}$ — LZ-R				
pXY162	*RSV*	3x FLAG — Syk_{FL} — LZ-E				
pXY117	*RSV*	3x FLAG — $Syk_{260-635}$ — LZ-E				
pXY163	*RSV*	3x FLAG — $Syk_{342-635}$ — LZ-E				
pXY164	*RSV*	3x FLAG — $Syk_{359-635}$ — LZ-E				
pXY165	*RSV*	3x FLAG — $Syk_{366-635}$ — LZ-E				
pXY167	*RSV*	3x FLAG — $ZAP70_{FL}$ — LZ-E				
pXY168	*RSV*	3x FLAG — $ZAP70_{255-619}$ — LZ-E				
pXY169	*RSV*	3x FLAG — $ZAP70_{309-619}$ — LZ-E				
pXY170	*RSV*	3x FLAG — $ZAP70_{309-619}$ — LZ-E				
pXY171	*RSV*	3x FLAG — $ZAP70_{326-619}$ — LZ-E				
pXY224	*RSV*	3x FLAG — LYN_{FL} — LZ-E				
pXY225	*RSV*	3x FLAG — $LYN_{227-512}$ — LZ-E				
pXY228	*RSV*	3x FLAG — Lck_{FL} — LZ-E				
pXY229	*RSV*	3x FLAG — $Lck_{225-509}$ — LZ-E				
pXY596	*RSV*	3x FLAG — Syk_{FL} — LZ-R				
pXY597	*RSV*	3x FLAG — $Syk_{260-635}$ — LZ-R				
pXY598	*RSV*	3x FLAG — $Syk_{342-635}$ — LZ-R				
pXY599	*RSV*	3x FLAG — $Syk_{359-635}$ — LZ-R				
pXY600	*RSV*	3x FLAG — $Syk_{366-635}$ — LZ-R				
pXY601	*RSV*	3x FLAG — $ZAP70_{FL}$ — LZ-R				
pXY602	*RSV*	3x FLAG — $ZAP70_{255-619}$ — LZ-R				
pXY603	*RSV*	3x FLAG — $ZAP70_{309-619}$ — LZ-R				
pXY604	*RSV*	3x FLAG — $ZAP70_{309-619}$ — LZ-R				
pXY605	*RSV*	3x FLAG — $ZAP70_{326-619}$ — LZ-R				
pXY606	*RSV*	3x FLAG — LYN_{FL} — LZ-R				
pXY607	*RSV*	3x FLAG — $LYN_{227-512}$ — LZ-R				

pXY608	*RSV*	3x FLAG — Lck_{FL} — LZ-R				
pXY609	*RSV*	3x FLAG — $Lck_{225-509}$ — LZ-R				
pXY341	*RSV*	3x FLAG — $ZAP70_{326-619, FF}$ — LZ-E				
pXY342	*RSV*	3x FLAG — $ZAP70_{309-619, Y492F}$ — LZ-E				
pXY343	*RSV*	3x FLAG — $ZAP70_{309-619, Y492E}$ — LZ-E				
pXY344	*RSV*	3x FLAG — $ZAP70_{309-619, Y493F}$ — LZ-E				
pXY345	*RSV*	3x FLAG — $ZAP70_{309-619, Y493E}$ — LZ-E				
pXY346	*RSV*	3x FLAG — $ZAP70_{309-619, EE}$ — LZ-E				
pXY347	*RSV*	3x FLAG — $ZAP70_{326-619, FF}$ — LZ-R				
pXY348	*RSV*	3x FLAG — $ZAP70_{326-619, FF}$ — LZ-E(S)				
pXY349	*RSV*	3x FLAG — $ZAP70_{326-619, FF}$ — LZ-E(E)				
pXY488	*RSV*	3x FLAG — $ABL_{242-540, Y393E}$ — LZ-E				
pXY489	*RSV*	3x FLAG — $ABL_{242-540, FF}$ — LZ-R				
pXY490	*RSV*	3x FLAG — $ABL_{242-540, Y226F}$ — LZ-E				
pXY491	*RSV*	3x FLAG — $ABL_{242-540, Y226E}$ — LZ-E				
pXY492	*RSV*	3x FLAG — $ABL_{242-540, Y393F}$ — LZ-E				
pXY493	*RSV*	3x FLAG — $ABL_{242-540, FF}$ — LZ-E				
pXY494	*RSV*	3x FLAG — $ABL_{242-540, FF, K271R}$ — LZ-E				
pXY174	*CMV*	3x FLAG — GST — 1x $CD3Z_{131-164, FF}$ — LZ-R				
pXY350	*CMV*	3x HA — $PTPN3_{583-913}$ — LZ-E				
pXY351	*CMV*	3x HA — $PTPN3_{606-913}$ — LZ-E				
pXY352	*CMV*	3x HA — $PTPN3_{628-913}$ — LZ-E				
pXY354	*CMV*	3x HA — $PTPN6_{214-595}$ — LZ-E				
pXY355	*CMV*	3x HA — $PTPN6_{241-595}$ — LZ-E				
pXY356	*CMV*	3x HA — $PTPN6_{214-527}$ — LZ-E				
pXY357	*CMV*	3x HA — $PTPN6_{241-527}$ — LZ-E				
pXY358	*RSV*	K3 — 3x FLAG — $ZAP70_{326-619, FF}$ — LZ-E				
pXY359	*RSV*	K7 — 3x FLAG — $ZAP70_{326-619, FF}$ — LZ-E				
pXY372	*CMV*	3xHA — $PTPN1_{1-268}$ — LZ-E				
pXY375	*RSV*	3x FLAG — $ZAP70_{326-619, FF, R460S}$ — LZ-E				
pXY419	*RSV*	3x FLAG — $ZAP70_{326-619, FF, R460K}$ — LZ-E				
pXY421	*RSV*	3x FLAG — $ZAP70_{326-619, FF, K369R}$ — LZ-E				
pXY423	*CMV*	3x HA — $PTPN1_{1-319}$ — LZ-E				
pXY538	*CMV*	3x HA — $PTPN1_{1-319, D181A}$ — LZ-E				

pXY539	*CMV*	3x HA — $PTPN1_{1-319}$ — EGFP				
pXY541	*CMV*	3x HA — $PTPN1_{1-319, E115A}$ — LZ-E				
pXY556	*CMV*	3x HA — $PTPN1_{1-319}$				
pXY476	*RSV*	3x FLAG — $ABL_{242-540}$ — LZ-E				
pTP229	*p(nc=8, 42-10)miniTK*	mCherry				
pXY203	*CMV*	sv40 NLS — 3x ZF (42-10) — GST — 3x $CD3Z_{64-95}$ — LZ-R				
pXY204	*CMV*	sv40 NLS — 3x ZF (42-10) — GST — 3x $CD3Z_{105-136}$ — LZ-R				
pXY112	*CMV*	sv40 NLS — 3x ZF (42-10) — GST — 3x $CD3Z_{131-164}$ — LZ-R				
pXY23	*CMV*	sv40 NLS — 3x ZF (42-10) — LZ-R				
pXY20	*hEF1a*	ZAP70_SH2 — VPR — sv40 NLS				
pXY235	*hEF1a*	Syk SH2 — VPR — sv40 NLS				
pXY236	*hEF1a*	SHP1 SH2 — VPR — sv40 NLS				
pXY237	*hEF1a*	SHP2 SH2 — VPR — sv40 NLS				
pXY238	*hEF1a*	p85a SH2 — VPR — sv40 NLS				
pXY239	*CMV*	sv40 NLS — 3x ZF (42-10) — GST — 3x$CD3\delta_{141-171}$ — LZ-R				
pXY240	*CMV*	sv40 NLS — 3x ZF (42-10) — GST — 3x$CD3\gamma_{163-182}$ — LZ-R				
pXY241	*CMV*	sv40_NLS — 3x ZF (42-10) — GST — 3x$CD3\varepsilon_{180-207}$ — LZ-R				
pXY252	*CMV*	sv40 NLS — 3x ZF (42-10) — GST — 3x $IgA_{181-211}$ — LZ-R				
pXY253	*CMV*	sv40 NLS — 3x ZF (42-10) — GST — 3x $IgB_{188-221}$ — LZ-R				
pXY254	*CMV*	sv40 NLS — 3x ZF (42-10) — GST — 3x $Fc\varepsilon R1\gamma_{56-86}$ — LZ-R				
pXY256	*CMV*	sv40 NLS — 3x ZF (42-10) — GST — 3x $SLP76_{108-154}$ — LZ-R				
pXY272	*CMV*	sv40 NLS — 3x ZF (42-10) — GST — 3x SHPS1_TAM — LZ-R				
pXY274	*CMV*	sv40 NLS — 3x ZF (42-10) — GST — 3x $PDGFR_{731-757}$ — LZ-R				
pXY288	*CMV*	3x MYC — $ZAP70_{326-619, FF}$ — 3x $CD3Z_{131-164}$ — LZ-R				
pXY327	*CMV*	3x MYC — $ZAP70_{326-619, FF}$ — GPbP — 3x $CD3Z_{131-164}$ — LZ-R				
pXY328	*CMV*	3x MYC — $ZAP70_{326-619, FF}$ — GPZP — 3x $CD3Z_{131-164}$ — LZ-R				

pXY384	*CMV*	3xMYC — $ZAP70_{326\text{-}619,\ FF,\ K369R}$ — GPZP — 1x $CD3Z_{131\text{-}164}$ — LZ-R				
pXY40	*CMV*	sv40 NLS — VPR — LZ-E				
pXY430	*CMV*	3xMYC — GST — 1x $SLP76_{108\text{-}154}$ — LZ-R				
pXY432	*CMV*	3x V5 — GST — 3x$SLP76_{108\text{-}154}$ — 2x ZAP70 tSH2				
pXY436	*CMV*	3x MYC — $ZAP70_{326\text{-}619,\ FF,\ K369R}$ — GPZP — 3x $CD3Z_{131\text{-}164}$ — LZ-R				
pXY449	*hEF1a*	2x $Vav1_{671\text{-}746}$ — VPR — sv40 NLS				
pXY451	*hEF1a*	$Vav1_{671\text{-}746}$ - $ITK_{239\text{-}338}$ — VPR — sv40 NLS				
pXY452	*hEF1a*	2x $Vav1_{671\text{-}746}$ - $ITK_{239\text{-}338}$ — VPR — sv40_NLS				
pXY460	*CMV*	3x MYC — $ZAP70_{326\text{-}619,\ FF}$ — 1x CD3Z_3 — EGFP				
pXY518	*RSV*	3x FLAG — $ZAP70_{326\text{-}619,\ FF}$ — EGFP				
pXY532	*CMV*	3x MYC — $ZAP70_{326\text{-}619,\ FF,\ R460K}$ — GPZP — 3x$CD3Z_{131\text{-}164}$ — LZ-R				
pXY553	*CMV*	3x V5 — GST — 3x $SLP76_{108\text{-}154}$ — 2xp85a tSH2				
pXY554	*CMV*	3x MYC — $ZAP70_{326\text{-}619,\ FF}$ — GPZP — 1x $CD3Z_{131\text{-}164}$ — LZ-R				
pXY555	*CMV*	3x V5 — GST — 1x$SLP76_{108\text{-}154}$ — ZAP70 $tSH2_{2\text{-}259}$				
pXY580	*CMV*	3x V5 — $ZAP70_{326\text{-}619,\ FF}$ — 3x $SLP76_{108\text{-}154}$ — GFP				
pXY581	*CMV*	3x V5 — $ZAP70_{326\text{-}619,\ FF}$ — 3x $SLP76_{108\text{-}154}$ — LZ-R				
pXY599	*RSV*	3xFLAG — $ABL_{228\text{-}540,\ FF,\ R362K}$ — LZ-E				
pXYBB30	*CMV*	IgλSP — FLAG — Frb_{K2095P} — 10x GS — CD28 TM — 10x GS — $ABL_{228\text{-}540}$	*CMV*	IgλSP — V5 — FKBP — 10x GS — CD28_TM — 10x GS — LZ-E		
pXYBB31	*CMV*	IgλSP — FLAG — Frb_{K2095P} — 10x GS — CD28 TM — 10x GS — $ABL_{228\text{-}540}$	*CMV*	IgλSP — V5 — FKBP — 5x GS — CD28 TM — 10x GS — LZ-E		
pXYBB32	*CMV*	IgλSP — FLAG — Frb_{K2095P} — 10x GS — CD28 TM — 10x GS — $ABL_{228\text{-}540}$	*CMV*	IgλSP — V5 — FKBP — 10x GS — CD28_TM — 5x GS — LZ-E		
pXYBB33	*CMV*	IgλSP — FLAG — Frb_{K2095P} — 5x GS — CD28 TM — 10xGS — $ABL_{228\text{-}540}$	*CMV*	IgλSP — V5 — FKBP — 10x GS — CD28 TM — 10x GS — LZ-E		
pXYBB34	*CMV*	IgλSP — FLAG — Frb_{K2095P} — 5x GS — CD28 TM — 10xGS — $ABL_{228\text{-}540}$	*CMV*	IgλSP — V5 — FKBP — 5x GS — CD28_TM — 10x GS — LZ-E		
pXYBB35	*CMV*	IgλSP — FLAG — Frb_{K2095P} — 5x GS — CD28 TM — 10xGS — $ABL_{228\text{-}540}$	*CMV*	IgλSP — V5 — FKBP — 10x GS — CD28 TM — 5x GS — LZ-E		

pXYBB36	*CMV*	IgλSP — FLAG — Frb_{K2095P} — 10x GS — CD28 TM — 5xGS — $ABL_{228-540}$	*CMV*	IgλSP — V5 — FKBP — 10x GS — CD28 TM — 10x GS — LZ-E		
pXYBB37	*CMV*	IgλSP — FLAG — Frb_{K2095P} — 10x GS — CD28 TM — 5xGS — $ABL_{228-540}$	*CMV*	IgλSP — V5 — FKBP — 5x GS — CD28 TM — 10x GS — LZ-E		
pXYBB38	*CMV*	IgλSP — FLAG — Frb_{K2095P} — 10x GS — CD28 TM — 5xGS — $ABL_{228-540}$	*CMV*	IgλSP — V5 — FKBP — 10x GS — CD28 TM — 5x GS — LZ-E		
pXYBB39	*CMV*	IgλSP — FLAG — Frb_{K2095P} — 10x GS — CD28 TM — 5xGS — $ABL_{228-542}$	*CMV*	IgλSP — V5 — FKBP — 10x GS — CD28 T M(M3) — 10x GS — LZ-E		
pXYBB40	*CMV*	IgλSP — FLAG — Frb_{K2095P} — 10x GS — CD28_TM — 5xGS — $ABL_{228-543}$	*CMV*	IgλSP — V5 — FKBP — 10x GS — CD28 M(M4) — 10x GS — LZ-E		
pXYBB41	*CMV*	IgλSP — FLAG — Frb_{K2095P} — 10x GS — CD28 TM(M3) — 5x GS — $ABL_{228-544}$	*CMV*	IgλSP — V5 — FKBP — 10x GS — CD28_TM — 10x GS — LZ-E		
pXYBB42	*CMV*	IgλSP — FLAG — Frb_{K2095P} — 10x GS — CD28 TM(M3) — 5x GS — $ABL_{228-545}$	*CMV*	IgλSP — V5 — FKBP — 10x GS — CD28 TM(M3) — 10x GS — LZ-E		
pXYBB43	*CMV*	IgλSP — FLAG — Frb_{K2095P} — 10x GS — CD 28 TM(M3) — 5x GS — $ABL_{228-546}$	*CMV*	IgλSP — V5 — FKBP — 10x GS — CD28 TM(M4) — 10x GS — LZ-E		
pXYBB44	*CMV*	IgλSP — FLAG — Frb_{K2095P} — 10x GS — CD28_TM(M4) — 5x GS — $ABL_{228-547}$	*CMV*	IgλSP — V5 — FKBP — 10x GS — CD28_TM — 10x GS — LZ-E		
pXYBB45	*CMV*	IgλSP — FLAG — Frb_{K2095P} — 10x GS — CD28 TM(M4) — 5x GS — $ABL_{228-548}$	*CMV*	IgλSP — V5 — FKBP — 10x GS — CD28 TM(M3) — 10x GS — LZ-E		
pXYBB46	*CMV*	IgλSP — FLAG — Frb_{K2095P} — 10x GS — CD28 TM(M4) — 5x GS — $ABL_{228-549}$	*CMV*	IgλSP — V5 — FKBP — 10x GS — CD28 TM(M4) — 10x GS — LZ-E		
pXYBB47	*CMV*	IgλSP — FLAG — Frb_{K2095P} — 10x GS — CD28 TM — 5x GS — $ABL_{228-543}$	*CMV*	IgλSP — V5 — FKBP — 10x GS — CD28_TM(M3) — 10x GS — LZ-R		
pXYBB48	*CMV*	IgλSP — FLAG — Frb_{K2095P} — 10x GS — CD28 TM — 5x GS — $ABL_{228-543,\ K271R}$	*CMV*	IgλSP — V5 — FKBP — 10x GS — CD28 TM(M3) — 10x GS — LZ-E		
pXYBB49	*CMV*	IgλSP — FLAG — $Frb_{L2098T,\ W2101F}$ — 10x GS — CD28 TM — 5x GS — $ABL_{228-543}$	*CMV*	IgλSP — V5 — FKBP — 10x GS — CD28 TM(M3) — 10x GS — LZ-E		
pXY565	*CMV*	GFP — NES — 3x $CD3Z_{131-164}$ — LZ-R	*hEF1a*	2x ZAP70 SH_{22-259} — mCherry — nanopop		
pXY568	*CMV*	GFP — NES — 3x $CD3Z_{131-164}$ — LZ-R	*hEF1a*	mCherry — nanopop		
pXY477	*CMV*	3x MYC — sv40 NLS — $ZAP70_{326-619,\ FF}$ — GPZP — 3x$CD3Z_{131-164}$ — LZ-R				
pXY481	*CMV*	3x MYC — $ZAP70_{326-619,\ FF}$ — GPZP — PKI NES — 3x $CD3Z_{131-164}$ — LZ-R				

pXY569	*CMV*	3x MYC — sv40_NLS — $ZAP70_{326\text{-}619,\ FF}$ — GPZP — PKI_NES — 3x $CD3Z_{131\text{-}164}$ — LZ-R				
pXY572	*CMV*	3x MYC — sv40 NLS — $ZAP70_{326\text{-}619,\ FF,\ R460K}$ — GPZP — PKI NES — 3x $CD3Z_{131\text{-}164}$ — LZ-R				
pXYBB50	*CMV*	IgκSP — 3x FLAG — TNFa scFv — CD28 TM — $ABL_{228\text{-}540}$	*CMV*	IgκSP — V5 — TNFa scFv — CD28 TM(M3) — LZ-E		
pXYE73	*CMV*	sv40_NLS — 6x ZF (ZF 10 -1) — GST — 3x $SLP76_{108\text{-}154}$ — 2x ZAP70 $tSH2_{2\text{-}259}$				
pXYBB51	*CMV*	sv40_NLS — 6x ZF (ZF 10 -1) — GST — 3x $SLP76_{108\text{-}154}$ — 2x ZAP70 $tSH2_{2\text{-}259}$	*hEF1a*	2x $Vav1_{671\text{-}746}$ - $ITK_{239\text{-}338}$ — VPR — sv40 NLS	*p(n_c=8, 10-1) miniCMV*	hIL-10
pXYBB52	*CMV*	sv40_NLS — ZF_10-1 — GST — 3x $SLP76_{108\text{-}154}$ — 2x ZAP70 $tSH2_{2\text{-}259}$	*hEF1a*	2x $Vav1_{671\text{-}746}$ - $ITK_{239\text{-}338}$ — VPR — sv40 NLS	*p(n_c=8, 10-1) ybTATA*	EGFP

Table S2: DNA Sequence for synTF Promoters

Part Class	Part Name	Part Sequence
Enhancer sites	n = 4x ZF (42-10) binding sites	CCGGCCGACGCTGCTCTTGAGACGCTGCTCTTGAGACGCTGCTCTTGAGACGCTGCTCTAG
Enhancer sites	n = 8x ZF (10-1) binding sites	CAAAACGCTTCGGCGTAGCCGATGTCGCGCTCCCGTGTCAGTAAAGGTCGGCGTAGCCGATGTCGCGCAATCGGACTCCCTTCGTACGGCGTAGCCGATGTCGCGCGTATCAGTCGCCTCGGAACGGCGTAGCCGATGTCGCGCATTCGTACAAAACGCCTTCGGCGTAGCCGATGTCGCGCTCCCGTGTCAGTAAAGGTCGGCGTAGCCGATGTCGCGCAATCGGACTCCCTTCGTACGGCGTAGCCGATGTCGCGCGTATCAGTCGCCTCGGAACGGCGTAGCCGATGTCGCGCATTCGTACAAA
Core promoter	miniCMV	GTAGGCGTGTACGGTGGGAGGTCTATATAAGCAGAGCTCGTTTAGTGAACCGTCAGATC
Core promoter	miniTK	TTCGCATATTAAGGTGACGCGTGTGGCCTCGAACACCGAGCGACCCTGCAGCGACCCGCTTAA
Core promoter	YB-TATA	TCTAGAGGGTATATAATGGGGGCCA

Table S3: Plasmid and transfection reagent usage

FIGURE #	CONDITION	PLASMID # AND USAGE (ng)		REAGENT
1B	synSub only	pXY127 250		PEI
	nonpplatable	pXY174, pXY341 250, 250		
	kinase-dead	pXY127, pXY421 250, 1000		
	recruited synKin	pXY127, pXY341 250, 250		
	unrecruited	pXY127, pXY347 250, 250		
1C	LZ affinity	pXY127 250	pXY348 250	PEI
			pXY349 250	
	synKin activity		pXY375 250	
			pXY419 250	
	synKin expression		pXY358 250	
			pXY359 250	
1D	recruited synPhos	pXY127, pXY341 250, 250	pXY423 1000	PEI
	phosphatase-dead		pXY538 1000	
	unrecruited		pXY556 1000	
1F	bottom left	pXY127, pXY538, pXY358 250, 1000, 250		PEI
	bottom middle	pXY127, pXY540, pXY359 250, 1000, 250		
	right top	pXY127, pXY423, pXY341 250, 200, 250		
	right bottom	pXY127, pXY541, pXY348 250, 1000, 250		
S5B	top	pXY341 250		PEI
		pXY127 250		
		pXY423 250		

		pXY432 250		
	bottom	pXY341 250		
		pXY127 250		
		pXY423 250		
S5C top	synSub only	pXY127 250		PEI
	nonpplatable	pXY174, pXY341 250, 250		
	kinase-dead	pXY127, pXY421 250, 1000		
	recruited synKin	pXY127, pXY341 250, 250		
	unrecruited	pXY127, pXY347 250, 250		
S5C bottom	synSub only	pXY127 100		jetPRIME
	nonpplatable	pXY174, pXY341 100, 100		
	kinase-dead	pXY127, pXY421 100, 200		
	recruited synKin	pXY127, pXY341 100, 100		
	unrecruited	pXY127, pXY347 100, 100		
S6B	synSub only	pXY127 250		PEI
S6C	Syk np synSub	pXY162 250	pXY174 250	PEI
		pXY117 250		
		pXY163 250		
		pXY164 250		
		pXY165 250		
	Syk nb synKin	pXY596 250	pXY127 250	

		pXY597 250	
		pXY598 250	
		pXY599 250	
		pXY600 250	
	Syk synKin + synSub	pXY162 250	pXY127 250
		pXY117 250	
		pXY163 250	
		pXY164 250	
		pXY165 250	
	ZAP70 np synSub	pXY167 250	pXY174 250
		pXY168 250	
		pXY169 250	
		pXY170 250	
		pXY171 250	
	ZAP70 nb synKin	pXY601 250	pXY127 250
		pXY602 250	
		pXY603 250	
		pXY604 250	
		pXY605 250	
	ZAP70 synKin + synSub	pXY167 250	pXY127 250
		pXY168 250	
		pXY169 250	
		pXY170 250	
		pXY171 250	
	Lyn np synSub	pXY224 250	pXY174 250

		pXY225 250		
	Lyn nb synKin	pXY606 250	pXY127 250	
		pXY607 250		
	Lyn synKin + synSub	pXY224 250	pXY127 250	
		pXY225 250		
	Lck np synSub	pXY228 250	pXY174 250	
		pXY229 250		
	Lck nb synKin	pXY608 250	pXY127 250	
		pXY609 250		
	Lck synKin + synSub	pXY228 250	pXY127 250	
		pXY229 250		
S6D	ZAP70	pXY170 250	pXY127 250	PEI
		pXY341 250		
		pXY342 250		
		pXY343 250		
		pXY344 250		
		pXY345 250		
		pXY346 250		
	ABL	pXY476 250	pXY127 250	
		pXY493 250		
		pXY490 250		
		pXY491 250		
		pXY492 250		
		pXY488 250		
		pXY489 250		

S7A	ZAP70 + CD3Z	pXY341 250	pXY127 250	PEI
		pXY347 250		
		/		
		pXY421 1000		
	ZAP70 + SLP76	pXY341 250, 250	pXY430 250	
		pXY347 250, 250		
		/		
		pXY421 250, 1000		
	ABL + CD3Z	pXY493 250	pXY127 250	
		pXY489 250		
		/		
		pXY494 250		
	ABL + SLP76	pXY493 250	pXY430 250	
		pXY489 250		
		/		
		pXY494 250		
S7B	synKin only	pXY341 250		PEI
	synSub only	pXY127 250		
	nonpplatable	pXY174, pXY341 250, 250		
	recruited synKin	pXY127, pXY341 250, 250		
	unrecruited synKin	pXY127, pXY347 250, 250		
	kinase dead	pXY127, pXY421 250, 1000		
S7C	synSub only	pXY127 250		PEI
	unrecruited synKin	pXY127, pXY347 250, 250		

	recruited synKin	pXY127, pXY341 250, 250		
S7D	synSub only	pXY127 250		PEI
	nonpplatable	pXY174, pXY341 250, 250		
	kinase-dead	pXY127, pXY421 250, 1000		
	recruited synKin	pXY127, pXY341 250, 250		
	unrecruited	pXY127, pXY347 250, 250		
S9B	PTPN1	pXY127, pXY341 250, 250	pXY372 1000	PEI
			pXY423 1000	
	PTPN3		pXY350 1000	
			pXY351 1000	
			pXY352 1000	
	PTPN6		pXY354 1000	
			pXY355 1000	
			pXY356 1000	
			pXY357 1000	
S10	FLAG-to-EGFP	pXY518 500		PEI
	pCD3z-to-MYC / MYC-to-EGFP	pXY460 500		
	HA-to-EGFP	pXY539 500		
	V5-to-EGFP	pXY580 500		
	SLP76-to-V5	pXY581 500		
2B	no synKin	pXY328, pXY432 250, 500	pXY423 100	PEI
	kinase-dead PC	pXY493, pXY436, pXY432 250, 250, 500		
	nb SH2	pXY493, pXY328, pXY553 250, 250, 500		

	multivalent	pXY493, pXY328, pXY432 250, 250, 500		
	monovalent	pXY493, pXY554, pXY555 250, 250, 500		
2C	config #1	pXY493, pXY532, pXY432, pXY423 250, 100, 500, 250		PEI
	config #2	pXY493, pXY328, pXY432, pXY541 250, 100, 500, 100		
	config #3	pXY493, pXY328, pXY432, pXY541 500, 100, 500, 100		
	config #4	pXY493, pXY328, pXY432, pXY541 250, 500, 500, 250		
S15A, B	reporter only	pTP229 250	/	PEI
	synTF only		pXY23 250	
	synTF + non-cognate LZ		pXY23, pXY41 250, 250	
	synTF + cognate LZ		pXY23, pXY40 250, 250	
S15C,D	TCR-ITAMs, BCR-ITAMs, FcR ITAM with ZAP70_tSH2	pXY493, pXY20, pTP229 250, 250, 250	pXY203 250	PEI
			pXY204 250	
			pXY112 250	
			pXY239 250	
			pXY240 250	
			pXY241 250	
			pXY252 250	
			pXY253 250	
			pXY254 250	
	TCR-ITAMs, BCR-ITAMs, FcR ITAM with Syk_tSH2	pXY493, pXY235, pTP229 250, 250, 250	pXY203 250	
			pXY204 250	
			pXY112 250	
			pXY239 250	
			pXY240 250	
			pXY241 250	
			pXY252 250	

			pXY253 250	
			pXY254 250	
	TCR-ITAMs, BCR-ITAMs, FcR ITAM with SHP1_tSH2	pXY493, pXY236, pTP229 250, 250, 250	pXY203 250	
			pXY204 250	
			pXY112 250	
			pXY239 250	
			pXY240 250	
			pXY241 250	
			pXY252 250	
			pXY253 250	
			pXY254 250	
	TCR-ITAMs, BCR-ITAMs, FcR ITAM with SHP2_tSH2	pXY493, pXY237, pTP229 250, 250, 250	pXY203 250	
			pXY204 250	
			pXY112 250	
			pXY239 250	
			pXY240 250	
			pXY241 250	
			pXY252 250	
			pXY253 250	
			pXY254 250	
	TCR-ITAMs, BCR-ITAMs, FcR ITAM with p85a_tSH2	pXY493, pXY238, pTP229 250, 250, 250	pXY203 250	
			pXY204 250	
			pXY112 250	
			pXY239 250	
			pXY240 250	

			pXY241 250	
			pXY252 250	
			pXY253 250	
			pXY254 250	
	PDGFR	pXY20 250	pXY493, pXY274, pTP229 250, 250, 250	
		pXY237 250		
		pXY238 250		
	SHPS-1	pXY20 250	pXY493, pXY272, pTP229 250, 250, 250	
		pXY237 250		
S16B	2x(Vav1-ITK)_SH2	pXY452 250	pXY341, pXY256, pTP229 250, 250, 250	PEI
	Vav1-ITK_SH2	pXY451 250		
	2xVav1_SH2	pXY449 250		
	ZAP70_tSH2	pXY20 250		
S17B	w. synKin	pXY288 250	pXY493, pXY432 250, 500	PEI
		pXY328 250		
		pXY327 250		
		pXY436 250		
	no synKin	pXY288 250	pXY432 500	
		pXY328 250		
		pXY327 250		
		pXY436 250		
3B	non-binding	pXYBB49, pXY423 400, 100	pXY129 500	PEI
	un-recruited	pXYBB47, pXY423 400, 100		
	kinase-dead	pXYBB48, pXY423 400, 100		
	phosphatase-dead	pXYBB39, pXY538 400, 100		

	complete phosphorylation cycle	pXYBB39, pXY423 400, 100		
3C		pXYBB39, pXY565, pXY423 200, 200, 25		jetPRIME
S20C	optimizing linker length	pXYBB30 400	pXY129 500	PEI
		pXYBB31 400		
		pXYBB32 400		
		pXYBB33 400		
		pXYBB34 400		
		pXYBB35 400		
		pXYBB36 400		
		pXYBB37 400		
		pXYBB38 400		
S20D	optimizing TM motif	pXYBB36 400		
		pXYBB39 400		
		pXYBB40 400		
		pXYBB41 400		
		pXYBB42 400		
		pXYBB43 400		
		pXYBB44 400		
		pXYBB45 400		
		pXYBB46 400		
S21C	complete circuit	pXYBB39, pXY565, pXY423 200, 200, 25		jetPRIME
	nb receptor	pXYBB49, pXY565, pXY423 200, 200, 25		

	nb SH2	pXYBB39, pXY568, pXY423 200, 200, 25		
S21D		pXYBB39, pXY565, pXY423 200, 200, 25		jetPRIME
S22A		pXYBB39, pXY565, pXY538 200, 200, 25		jetPRIME
4A	no NLS/NES	pXY328 200	pXYBB39, pXYBB52, pXY541 200, 500, 25	jetPRIME
	NLS/NES	pXY569 200		
S23B	no NLS/NES	pXY328 200	pXYBB39, pXYE73, pXY541 200, 500, 25	jetPRIME
	NLS	pXY477 200		
	NES	pXY481 200		
	NLS/NES	pXY569 200		
S24A	config #1	pXYBB39, pXY572, pXYBB52, pXY423 200, 200, 500, 25		jetPRIME
	config #2	pXYBB39, pXY569, pXYBB52, pXY541 200, 200, 500, 25		
	config #3	pXYBB39, pXY569, pXYBB52, pXY541 500, 200, 500, 25		
	config #4	pXYBB39, pXY569, pXYBB52, pXY541 200, 500, 500, 50		
	config #5	pXYBB39, pXY569, pXYBB52, pXY423 200, 200, 500, 25		
	config #6	pXYBB39, pXY569, pXYBB52, pXY541 200, 200, 200, 25		
	config #7	pXYBB39, pXY569, pXYBB52, pXY538 200, 200, 500, 25		
	config #8	pXYBB39, pXY569, pXYBB52, pXY541 200, 500, 500, 25		
S24B	pXYBB39, pXY569, pXYBB52, pXY541 200, 200, 500, 25			jetPRIME
4B, S25B	pXYBB50, pXY129, pXY541 200, 500, 100			PEI

4C, S26B, C	open loop	pXY493 200	pXY569, pXYBB51, pXY541 200, 500, 25	jetPRIME
	closed loop	pXYBB50 200		
S30A	ARPE-19	pXYBB39, pXY129, pY423 200, 200, 50		jetPRIME
	hUC-MSC	pXYBB39, pXY129, pY423 800, 500, 100		Nucleofection
S30B	ARPE-19	pXYBB39, pXY569, pXYBB50, pY423 100, 100, 200, 50		Neon

Table S4: Phospho-staining antibody and fluorescence protein usage

	APC α-FLAG	AF 750 α-MYC	PE α-CD247 (pY142)	AF 594 α-HA	AF 680 α-V5	AF 488 α-SLP76 (pY128)	GFP	BFP
Figs. 1B, C, D, E, F/ S5B (4-color panel), S5C/S6/S7A (CD3Z panel), S7C/S9B	✓	✓	✓	✓				✓
Figs. S7A (SLP76 panel)	✓	✓		✓		✓		✓
Figs. S10 all panels except SLP76-to-V5	✓	✓	✓	✓	✓		✓	✓
Fig.S10 SLP76-to-V5					✓	✓		✓
Figs. 2B, C/ S5B (6-color panel) /S17B	✓	✓	✓	✓	✓	✓		✓
Figs. 3B/S20/4B/S25B/S30A	✓	✓	✓	✓				✓
Fig. S23B	✓	✓	✓	✓	✓	✓		✓
Fig. 4A/S24/S30B	✓	✓	✓	✓			✓	✓

Table S5: Model fitting

NAME OF FUNCTION	INPUT DATA TYPE	FUNCTION DESCRIPTION	ASSOCIATED FIGURES
noise_models.py	unmixed flow data	converts species expression and phosphorylation level into GFP units and then into MOCUs	1E, F/2C/S10
thermo_models.py	species expression in MOCUs	calculates phosphorylation levels based on species expression and fitted parameters	S11/S12/S18
model_fitting.py	phosphorylation and species expression in MOCUs	procedure for maximum-likelihood fitting of phosphorylation measurements to the thermodynamic models to obtain biophysical parameters	S11/S12/S18
fig_plot.py	species expression and phosphorylation level in AUs	generates HHH plots	1B, C, D, F/2B, C/3B/4A, B/S5C/S7A/S21D/S24A/S30A
fit_pushpull_models.ipynb	unmixed flow data	generates fitting for single phosphorylation cycle	1E/S11/S12
fit_twolayers.ipynb	unmixed flow data	generates fitting for two-step phosphorylation cycle	2C/S11/S18
plot_fit_params.ipynb	fitted biophysical parameters with error bars, fitted and predicted phosphorylation levels from single and two-step circuit model	plots fitted parameters and error bar, calculates D_{KS} comparing experimentally measured and model-predicted distributions	S12/S13/S18/S19
plot_activation_curves.ipynb	fitted biophysical parameters, compoenent expression levels, fitted and predicted phosphorylation levels from single cycle circuit model	plot Goldbeter-Koshland curves from noise model-inferred expression levels and phosphorylation levels, calculate EC_{50} and n_H values	S14
dose_curve.m	unmixed flow data	plot dose response curves for sensor circuits and sens-and-respond circuit, calculate EC_{50} and n_H values	3B/S24B/S25B
Dynamic_model.m	normalized condensate ratio, ELISA data for IL-10 and TNF-α	fits parameters for phospho-sensor activation/deactivation and generates plots; fits/plots parameters for cytokine production/interaction	S22/S27/S28

Table S6: Image analysis

NAME OF FUNCTION	INPUT DATA TYPE	FUNCTION DESCRIPTION	ASSOCIATED FIGURES
condensate_analysis.m	single cell mask generated in illastik, raw images as tiff. file	determines the intensity threshold for co-localized condensates and calculates the condensate ratio within each single-cell mask	3C/S22
intensity_along_line.m	raw images as tiff. file	quantifies analysis for GFP and mCherry condensate co-localization along a line at different timepoints	3C

Supplementary Movies

Movies S1. Time-lapse fluorescence microscopy showing activation of two representative single cells harboring the phospho-sensor circuit and condensate reporter. The time-lapse (80 min total, each frame is 10min) was initiated at t=-10 min and ligand AP21967 was added to the culture at t=0 min to a final concentration of 200 nM. Movies are presented in an EGFP- and mCherry-merged format, in false colors (green and red, respectively). A timestamp is displayed on the top left of each frame throughout the time-lapse. Scale bar, 5 μm.

Movies S2. Time-lapse fluorescence microscopy showing deactivation of two representative single cells harboring the phospho-sensor circuit and condensate reporter. The time-lapse (60 min total, each frame is 5 min) was initiated at t=-5 min and ABL inhibitor imatinib mesylate was added to the culture at t=0 min a final concentration of 10 μM. Movies are presented in a GFP- and mCherry-merged format, in false colors (green and red, respectively). A timestamp is displayed on the top left of each frame throughout the time-lapse. Scale bar, 5 μm.

References and Notes

1. T. Pawson, J. D. Scott, Protein phosphorylation in signaling—50 years and counting. *Trends Biochem. Sci.* **30**, 286–290 (2005).

2. W. A. Lim, Designing customized cell signalling circuits. *Nat. Rev. Mol. Cell Biol.* **11**, 393–403 (2010).

3. R. Kojima, D. Aubel, M. Fussenegger, Building sophisticated sensors of extracellular cues that enable mammalian cells to work as "doctors" in the body. *Cell. Mol. Life Sci.* **77**, 3567–3581 (2020).

4. C. J. Bashor, I. B. Hilton, H. Bandukwala, D. M. Smith, O. Veiseh, Engineering the next generation of cell-based therapeutics. *Nat. Rev. Drug Discov.* **21**, 655–675 (2022).

5. D. E. Cameron, C. J. Bashor, J. J. Collins, A brief history of synthetic biology. *Nat. Rev. Microbiol.* **12**, 381–390 (2014).

6. C. J. Bashor, J. J. Collins, Understanding biological regulation through synthetic biology. *Annu. Rev. Biophys.* **47**, 399–423 (2018).

7. A. S. Khalil, T. K. Lu, C. J. Bashor, C. L. Ramirez, N. C. Pyenson, J. K. Joung, J. J. Collins, A synthetic biology framework for programming eukaryotic transcription functions. *Cell* **150**, 647–658 (2012).

8. C. A. Voigt, Genetic parts to program bacteria. *Curr. Opin. Biotechnol.* **17**, 548–557 (2006).

9. A. A. Nielsen, B. S. Der, J. Shin, P. Vaidyanathan, V. Paralanov, E. A. Strychalski, D. Ross, D. Densmore, C. A. Voigt, Genetic circuit design automation. *Science* **352**, aac7341 (2016).

10. C. J. Bashor, N. Patel, S. Choubey, A. Beyzavi, J. Kondev, J. J. Collins, A. S. Khalil, Complex signal processing in synthetic gene circuits using cooperative regulatory assemblies. *Science* **364**, 593–597 (2019).

11. J. M. Skerker, B. S. Perchuk, A. Siryaporn, E. A. Lubin, O. Ashenberg, M. Goulian, M. T. Laub, Rewiring the specificity of two-component signal transduction systems. *Cell* **133**, 1043–1054 (2008).

12. W. R. Whitaker, S. A. Davis, A. P. Arkin, J. E. Dueber, Engineering robust control of two-component system phosphotransfer using modular scaffolds. *Proc. Natl. Acad. Sci. U.S.A.* **109**, 18090–18095 (2012).

13. S. R. Schmidl, F. Ekness, K. Sofjan, K. N.-M. Daeffler, K. R. Brink, B. P. Landry, K. P. Gerhardt, N. Dyulgyarov, R. U. Sheth, J. J. Tabor, Rewiring bacterial two-component systems by modular DNA-binding domain swapping. *Nat. Chem. Biol.* **15**, 690–698 (2019).

14. A. Mazé, Y. Benenson, Artificial signaling in mammalian cells enabled by prokaryotic two-component system. *Nat. Chem. Biol.* **16**, 179–187 (2020).

15. L. Scheller, M. Schmollack, A. Bertschi, M. Mansouri, P. Saxena, M. Fussenegger, Phosphoregulated orthogonal signal transduction in mammalian cells. *Nat. Commun.* **11**, 3085 (2020).

16. R. D. Jones, Y. Qian, K. Ilia, B. Wang, M. T. Laub, D. Del Vecchio, R. Weiss, Robust and tunable signal processing in mammalian cells via engineered covalent modification cycles. *Nat. Commun.* **13**, 1720 (2022).

17. D. Mishra, P. M. Rivera, A. Lin, D. Del Vecchio, R. Weiss, A load driver device for engineering modularity in biological networks. *Nat. Biotechnol.* **32**, 1268–1275 (2014).

18. D. Mishra, T. Bepler, B. Teague, B. Berger, J. Broach, R. Weiss, An engineered protein-phosphorylation toggle network with implications for endogenous network discovery. *Science* **373**, eaav0780 (2021).

19. R. M. Gordley, R. E. Williams, C. J. Bashor, J. E. Toettcher, S. Yan, W. A. Lim, Engineering dynamical control of cell fate switching using synthetic phospho-regulons. *Proc. Natl. Acad. Sci. U.S.A.* **113**, 13528–13533 (2016).

20. H. K. Chung, X. Zou, B. T. Bajar, V. R. Brand, Y. Huo, J. F. Alcudia, J. E. Ferrell Jr., M. Z. Lin, A compact synthetic pathway rewires cancer signaling to therapeutic effector release. *Science* **364**, eaat6982 (2019).

21. L. Schukur, B. Geering, G. Charpin-El Hamri, M. Fussenegger, Implantable synthetic cytokine converter cells with AND-gate logic treat experimental psoriasis. *Sci. Transl. Med.* **7**, 318ra201 (2015).

22. K. Krawczyk, L. Scheller, H. Kim, M. Fussenegger, Rewiring of endogenous signaling pathways to genomic targets for therapeutic cell reprogramming. *Nat. Commun.* **11**, 608 (2020).

23. A. Goldbeter, D. E. Koshland Jr., An amplified sensitivity arising from covalent modification in biological systems. *Proc. Natl. Acad. Sci. U.S.A.* **78**, 6840–6844 (1981).

24. D. Bray, Protein molecules as computational elements in living cells. *Nature* **376**, 307–312 (1995).

25. T. Pawson, P. Nash, Protein-protein interactions define specificity in signal transduction. *Genes Dev.* **14**, 1027–1047 (2000).

26. R. P. Bhattacharyya, A. Reményi, B. J. Yeh, W. A. Lim, Domains, motifs, and scaffolds: The role of modular interactions in the evolution and wiring of cell signaling circuits. *Annu. Rev. Biochem.* **75**, 655–680 (2006).

27. Z. Chen, M. B. Elowitz, Programmable protein circuit design. *Cell* **184**, 2284–2301 (2021).

28. S. H. Park, A. Zarrinpar, W. A. Lim, Rewiring MAP kinase pathways using alternative scaffold assembly mechanisms. *Science* **299**, 1061–1064 (2003).

29. C. J. Bashor, N. C. Helman, S. Yan, W. A. Lim, Using engineered scaffold interactions to reshape MAP kinase pathway signaling dynamics. *Science* **319**, 1539–1543 (2008).

30. A. H. Courtney, W. L. Lo, A. Weiss, TCR signaling: Mechanisms of initiation and propagation. *Trends Biochem. Sci.* **43**, 108–123 (2018).

31. A. Acharya, S. B. Ruvinov, J. Gal, J. R. Moll, C. Vinson, A heterodimerizing leucine zipper coiled coil system for examining the specificity of a position interactions: Amino acids I, V, L, N, A, and K. *Biochemistry* **41**, 14122–14131 (2002).

32. D. M. Underhill, H. S. Goodridge, The many faces of ITAMs. *Trends Immunol.* **28**, 66–73 (2007).

33. Y. Cui, G. Sun, Structural versatility that serves the function of the HRD motif in the catalytic loop of protein tyrosine kinase, Src. *Protein Sci.* **28**, 533–542 (2019).

34. J. P. Ferreira, K. W. Overton, C. L. Wang, Tuning gene expression with synthetic upstream open reading frames. *Proc. Natl. Acad. Sci. U.S.A.* **110**, 11284–11289 (2013).

35. L. Tautz, D. A. Critton, S. Grotegut, Protein tyrosine phosphatases: Structure, function, and implication in human disease. *Methods Mol. Biol.* **1053**, 179–221 (2013).

36. J. A. Ubersax, J. E. Ferrell Jr., Mechanisms of specificity in protein phosphorylation. *Nat. Rev. Mol. Cell Biol.* **8**, 530–541 (2007).

37. T. Pawson, Specificity in signal transduction: From phosphotyrosine-SH2 domain interactions to complex cellular systems. *Cell* **116**, 191–203 (2004).

38. E. A. Ottinger, M. C. Botfield, S. E. Shoelson, Tandem SH2 domains confer high specificity in tyrosine kinase signaling. *J. Biol. Chem.* **273**, 729–735 (1998).

39. P. B. Detwiler, S. Ramanathan, A. Sengupta, B. I. Shraiman, Engineering aspects of enzymatic signal transduction: Photoreceptors in the retina. *Biophys. J.* **79**, 2801–2817 (2000).

40. B. Z. Stanton, E. J. Chory, G. R. Crabtree, Chemically induced proximity in biology and medicine. *Science* **359**, eaao5902 (2018).

41. G. Ebersbach, A. Briegel, G. J. Jensen, C. Jacobs-Wagner, A self-associating protein critical for chromosome attachment, division, and polar organization in caulobacter. *Cell* **134**, 956–968 (2008).

42. S. Boeynaems, S. Alberti, N. L. Fawzi, T. Mittag, M. Polymenidou, F. Rousseau, J. Schymkowitz, J. Shorter, B. Wolozin, L. Van Den Bosch, P. Tompa, M. Fuxreiter, Protein phase separation: A new phase in cell biology. *Trends Cell Biol.* **28**, 420–435 (2018).

43. H. Kiu, S. E. Nicholson, Biology and significance of the JAK/STAT signalling pathways. *Growth Factors* **30**, 88–106 (2012).

44. B. Labibi, M. Bashkurov, J. L. Wrana, L. Attisano, Modeling the control of TGF-β/Smad nuclear accumulation by the Hippo pathway effectors, Taz/Yap. *iScience* **23**, 101416 (2020).

45. A. Saxena, S. Khosraviani, S. Noel, D. Mohan, T. Donner, A. R. A. Hamad, Interleukin-10 paradox: A potent immunoregulatory cytokine that has been difficult to harness for immunotherapy. *Cytokine* **74**, 27–34 (2015).

46. N. B. Woodall, Z. Weinberg, J. Park, F. Busch, R. S. Johnson, M. J. Feldbauer, M. Murphy, M. Ahlrichs, I. Yousif, M. J. MacCoss, V. H. Wysocki, H. El-Samad, D. Baker, De novo design of tyrosine and serine kinase-driven protein switches. *Nat. Struct. Mol. Biol.* **28**, 762–770 (2021).

47. J. E. Ferrell Jr., S. H. Ha, Ultrasensitivity part III: Cascades, bistable switches, and oscillators. *Trends Biochem. Sci.* **39**, 612–618 (2014).

48. Z. Chen, J. M. Linton, S. Xia, X. Fan, D. Yu, J. Wang, R. Zhu, M. B. Elowitz, A synthetic protein-level neural network in mammalian cells. *Science* **386**, 1243–1250 (2024).

49. J. Manhas, H. I. Edelstein, J. N. Leonard, L. Morsut, The evolution of synthetic receptor systems. *Nat. Chem. Biol.* **18**, 244–255 (2022).

50. X. J. Gao, L. S. Chong, M. S. Kim, M. B. Elowitz, Programmable protein circuits in living cells. *Science* **361**, 1252–1258 (2018).

51. E. Weber, C. Engler, R. Gruetzner, S. Werner, S. Marillonnet, A modular cloning system for standardized assembly of multigene constructs. *PLOS ONE* **6**, e16765 (2011).

52. J. Norrander, T. Kempe, J. Messing, Construction of improved M13 vectors using oligodeoxynucleotide-directed mutagenesis. *Gene* **26**, 101–106 (1983).

53. M. Boshart, F. Weber, G. Jahn, K. Dorsch-Häsler, B. Fleckenstein, W. Schaffner, A very strong enhancer is located upstream of an immediate early gene of human cytomegalovirus. *Cell* **41**, 521–530 (1985).

54. V. Busskamp, N. E. Lewis, P. Guye, A. H. M. Ng, S. L. Shipman, S. M. Byrne, N. E. Sanjana, J. Murn, Y. Li, S. Li, M. Stadler, R. Weiss, G. M. Church, Rapid neurogenesis through transcriptional activation in human stem cells. *Mol. Syst. Biol.* **10**, 760 (2014).

55. T. Dull, R. Zufferey, M. Kelly, R. J. Mandel, M. Nguyen, D. Trono, L. Naldini, A third-generation lentivirus vector with a conditional packaging system. *J. Virol.* **72**, 8463–8471 (1998).

56. F. A. Ran, L. Cong, W. X. Yan, D. A. Scott, J. S. Gootenberg, A. J. Kriz, B. Zetsche, O. Shalem, X. Wu, K. S. Makarova, E. V. Koonin, P. A. Sharp, F. Zhang, In vivo genome editing using *Staphylococcus aureus* Cas9. *Nature* **520**, 186–191 (2015).

57. P. A. Longo, J. M. Kavran, M. S. Kim, D. J. Leahy, Transient mammalian cell transfection with polyethylenimine (PEI). *Methods Enzymol.* **529**, 227–240 (2013).

58. J. H. Bayle, J. S. Grimley, K. Stankunas, J. E. Gestwicki, T. J. Wandless, G. R. Crabtree, Rapamycin analogs with differential binding specificity permit orthogonal control of protein activity. *Chem. Biol.* **13**, 99–107 (2006).

59. P. O. Krutzik, G. P. Nolan, Intracellular phospho-protein staining techniques for flow cytometry: Monitoring single cell signaling events. *Cytometry A* **55**, 61–70 (2003).

60. S. Berg, D. Kutra, T. Kroeger, C. N. Straehle, B. X. Kausler, C. Haubold, M. Schiegg, J. Ales, T. Beier, M. Rudy, K. Eren, J. I. Cervantes, B. Xu, F. Beuttenmueller, A. Wolny, C. Zhang, U. Koethe, F. A. Hamprecht, A. Kreshuk, ilastik: Interactive machine learning for (bio)image analysis. *Nat. Methods* **16**, 1226–1232 (2019).

61. Q. Zhang, H. Huang, L. Zhang, R. Wu, C.-I. Chung, S.-Q. Zhang, J. Torra, A. Schepis, S. R. Coughlin, T. B. Kornberg, X. Shu, Visualizing dynamics of cell signaling in vivo with a phase separation-based kinase reporter. *Mol. Cell* **69**, 334–346.e4 (2018).

62. J. J. Calis, M. Maybeno, J. A. Greenbaum, D. Weiskopf, A. D. De Silva, A. Sette, C. Keşmir, B. Peters, Properties of MHC class I presented peptides that enhance immunogenicity. *PLOS Comput. Biol.* **9**, e1003266 (2013).

63. J. D. Jordan, E. M. Landau, R. Iyengar, Signaling networks: The origins of cellular multitasking. *Cell* **103**, 193–200 (2000).

64. H. Lavoie, J. Gagnon, M. Therrien, ERK signalling: A master regulator of cell behaviour, life and fate. *Nat. Rev. Mol. Cell Biol.* **21**, 607–632 (2020).

65. B. T. MacDonald, K. Tamai, X. He, Wnt/beta-catenin signaling: Components, mechanisms, and diseases. *Dev. Cell* **17**, 9–26 (2009).

66. E. Batlle, J. Massagué, Transforming growth factor-β signaling in immunity and cancer. *Immunity* **50**, 924–940 (2019).

67. R. Sever, J. S. Brugge, Signal transduction in cancer. *Cold Spring Harb. Perspect. Med.* **5**, a006098 (2015).

68. M. A. Lemmon, J. Schlessinger, Cell signaling by receptor tyrosine kinases. *Cell* **141**, 1117–1134 (2010).

69. J. C. Renauld, Class II cytokine receptors and their ligands: Key antiviral and inflammatory modulators. *Nat. Rev. Immunol.* **3**, 667–676 (2003).

70. G. A. Koretzky, F. Abtahian, M. A. Silverman, SLP76 and SLP65: Complex regulation of signalling in lymphocytes and beyond. *Nat. Rev. Immunol.* **6**, 67–78 (2006).

71. C. Braicu, M. Buse, C. Busuioc, R. Drula, D. Gulei, L. Raduly, A. Rusu, A. Irimie, A. G. Atanasov, O. Slaby, C. Ionescu, I. Berindan-Neagoe, A comprehensive review on MAPK: A promising therapeutic target in cancer. *Cancers* **11**, 1618 (2019).

72. T. Tamura, H. Yanai, D. Savitsky, T. Taniguchi, The IRF family transcription factors in immunity and oncogenesis. *Annu. Rev. Immunol.* **26**, 535–584 (2008).

73. A. Rao, C. Luo, P. G. Hogan, Transcription factors of the NFAT family: Regulation and function. *Annu. Rev. Immunol.* **15**, 707–747 (1997).

74. B. Novak, O. Kapuy, M. R. Domingo-Sananes, J. J. Tyson, Regulated protein kinases and phosphatases in cell cycle decisions. *Curr. Opin. Cell Biol.* **22**, 801–808 (2010).

75. T. Pawson, P. Nash, Assembly of cell regulatory systems through protein interaction domains. *Science* **300**, 445–452 (2003).

76. T. Pawson, Protein modules and signalling networks. *Nature* **373**, 573–580 (1995).

77. W. M. Kavanaugh, C. W. Turck, L. T. Williams, PTB domain binding to signaling proteins through a sequence motif containing phosphotyrosine. *Science* **268**, 1177–1179 (1995).

78. J. Schlessinger, M. A. Lemmon, SH2 and PTB domains in tyrosine kinase signaling. *Sci. STKE* **2003**, RE12 (2003).

79. C. G. Broustas, N. Grammatikakis, M. Eto, P. Dent, D. L. Brautigan, U. Kasid, Phosphorylation of the myosin-binding subunit of myosin phosphatase by Raf-1 and inhibition of phosphatase activity. *J. Biol. Chem.* **277**, 3053–3059 (2002).

80. H. S. Goodfellow, M. P. Frushicheva, Q. Ji, D. A. Cheng, T. A. Kadlecek, A. J. Cantor, J. Kuriyan, A. K. Chakraborty, A. Salomon, A. Weiss, The catalytic activity of the kinase ZAP-70 mediates basal signaling and negative feedback of the T cell receptor pathway. *Sci. Signal.* **8**, ra49 (2015).

81. P. M. Clare, R. A. Poorman, L. C. Kelley, K. D. Watenpaugh, C. A. Bannow, K. L. Leach, The cyclin-dependent kinases cdk2 and cdk5 act by a random, anticooperative kinetic mechanism. *J. Biol. Chem.* **276**, 48292–48299 (2001).

82. H. Bae, T. Viennet, E. Park, N. Chu, A. Salguero, M. J. Eck, H. Arthanari, P. A. Cole, PH domain-mediated autoinhibition and oncogenic activation of Akt. *eLife* **11**, e80148 (2022).

83. M. J. Moore, J. A. Adams, S. S. Taylor, Structural basis for peptide binding in protein kinase A. Role of glutamic acid 203 and tyrosine 204 in the peptide-positioning loop. *J. Biol. Chem.* **278**, 10613–10618 (2003).

84. P. S. Brignola, K. Lackey, S. H. Kadwell, C. Hoffman, E. Horne, H. L. Carter, J. D. Stuart, K. Blackburn, M. B. Moyer, K. J. Alligood, W. B. Knight, E. R. Wood, Comparison of the biochemical and kinetic properties of the type 1 receptor tyrosine kinase intracellular domains. Demonstration of differential sensitivity to kinase inhibitors. *J. Biol. Chem.* **277**, 1576–1585 (2002).

85. Y. X. Fan, L. Wong, T. B. Deb, G. R. Johnson, Ligand regulates epidermal growth factor receptor kinase specificity: Activation increases preference for GAB1 and SHC versus autophosphorylation sites. *J. Biol. Chem.* **279**, 38143–38150 (2004).

86. J. Bubeck Wardenburg, C. Fu, J. K. Jackman, H. Flotow, S. E. Wilkinson, D. H. Williams, R. Johnson, G. Kong, A. C. Chan, P. R. Findell, Phosphorylation of SLP-76 by the ZAP-70 protein-tyrosine kinase is required for T-cell receptor function. *J. Biol. Chem.* **271**, 19641–19644 (1996).

87. S. Mukherjee, J. Zhu, J. Zikherman, R. Parameswaran, T. A. Kadlecek, Q. Wang, B. Au-Yeung, H. Ploegh, J. Kuriyan, J. Das, A. Weiss, Monovalent and multivalent ligation of the B cell receptor exhibit differential dependence upon Syk and Src family kinases. *Sci. Signal.* **6**, ra1 (2013).

88. A. Li, R. Voleti, M. Lee, D. Gagoski, N. H. Shah, High-throughput profiling of sequence recognition by tyrosine kinases and SH2 domains using bacterial peptide display. *eLife* **12**, e82345 (2023).

89. P. Filippakopoulos, M. Kofler, O. Hantschel, G. D. Gish, F. Grebien, E. Salah, P. Neudecker, L. E. Kay, B. E. Turk, G. Superti-Furga, T. Pawson, S. Knapp, Structural coupling of SH2-kinase domains links Fes and Abl substrate recognition and kinase activation. *Cell* **134**, 793–803 (2008).

90. T. Pawson, J. D. Scott, Signaling through scaffold, anchoring, and adaptor proteins. *Science* **278**, 2075–2080 (1997).

91. X. Su, J. A. Ditlev, E. Hui, W. Xing, S. Banjade, J. Okrut, D. S. King, J. Taunton, M. K. Rosen, R. D. Vale, Phase separation of signaling molecules promotes T cell receptor signal transduction. *Science* **352**, 595–599 (2016).

92. K. M. Shokat, Tyrosine kinases: Modular signaling enzymes with tunable specificities. *Chem. Biol.* **2**, 509–514 (1995).

93. P. E. Love, S. M. Hayes, ITAM-mediated signaling by the T-cell antigen receptor. *Cold Spring Harb. Perspect. Biol.* **2**, a002485 (2010).

94. B. B. Au-Yeung, N. H. Shah, L. Shen, A. Weiss, ZAP-70 in Signaling, Biology, and Disease. *Annu. Rev. Immunol.* **36**, 127–156 (2018).

95. H. Wang, T. A. Kadlecek, B. B. Au-Yeung, H. E. S. Goodfellow, L. Y. Hsu, T. S. Freedman, A. Weiss, ZAP-70: An essential kinase in T-cell signaling. *Cold Spring Harb. Perspect. Biol.* **2**, a002279 (2010).

96. A. Mócsai, J. Ruland, V. L. Tybulewicz, The SYK tyrosine kinase: A crucial player in diverse biological functions. *Nat. Rev. Immunol.* **10**, 387–402 (2010).

97. J. Colicelli, ABL tyrosine kinases: Evolution of function, regulation, and specificity. *Sci. Signal.* **3**, re6 (2010).

98. C. L. Abram, C. A. Lowell, The expanding role for ITAM-based signaling pathways in immune cells. *Sci. STKE* **2007**, re2 (2007).

99. N. Isakov, R. L. Wange, W. H. Burgess, J. D. Watts, R. Aebersold, L. E. Samelson, ZAP-70 binding specificity to T cell receptor tyrosine-based activation motifs: The tandem SH2 domains of ZAP-70 bind distinct tyrosine-based activation motifs with varying affinity. *J. Exp. Med.* **181**, 375–380 (1995).

100. R. L. Wange, R. Guitián, N. Isakov, J. D. Watts, R. Aebersold, L. E. Samelson, Activating and inhibitory mutations in adjacent tyrosines in the kinase domain of ZAP-70. *J. Biol. Chem.* **270**, 18730–18733 (1995).

101. M. Szabo, T. Czompoly, K. Kvell, G. Talaber, D. Bartis, P. Nemeth, T. Berki, F. Boldizsar, Fine-tuning of proximal TCR signaling by ZAP-70 tyrosine residues in Jurkat cells. *Int. Immunol.* **24**, 79–87 (2012).

102. K. Q. Tanis, D. Veach, H. S. Duewel, W. G. Bornmann, A. J. Koleske, Two distinct phosphorylation pathways have additive effects on Abl family kinase activation. *Mol. Cell. Biol.* **23**, 3884–3896 (2003).

103. S. Deindl, T. A. Kadlecek, T. Brdicka, X. Cao, A. Weiss, J. Kuriyan, Structural basis for the inhibition of tyrosine kinase activity of ZAP-70. *Cell* **129**, 735–746 (2007).

104. A. S. Corbin, E. Buchdunger, F. Pascal, B. J. Druker, Analysis of the structural basis of specificity of inhibition of the Abl kinase by STI571. *J. Biol. Chem.* **277**, 32214–32219 (2002).

105. N. H. Shah, Q. Wang, Q. Yan, D. Karandur, T. A. Kadlecek, I. R. Fallahee, W. P. Russ, R. Ranganathan, A. Weiss, J. Kuriyan, An electrostatic selection mechanism controls sequential kinase signaling downstream of the T cell receptor. *eLife* **5**, e20105 (2016).

106. N. H. Shah, M. Löbel, A. Weiss, J. Kuriyan, Fine-tuning of substrate preferences of the Src-family kinase Lck revealed through a high-throughput specificity screen. *eLife* **7**, e35190 (2018).

107. N. K. Tonks, Protein tyrosine phosphatases: From genes, to function, to disease. *Nat. Rev. Mol. Cell Biol.* **7**, 833–846 (2006).

108. A. Bourdeau, N. Dubé, M. L. Tremblay, Cytoplasmic protein tyrosine phosphatases, regulation and function: The roles of PTP1B and TC-PTP. *Curr. Opin. Cell Biol.* **17**, 203–209 (2005).

109. T. Matozaki, T. Uchida, Y. Fujioka, M. Kasuga, Src kinase tyrosine phosphorylates PTP1C, a protein tyrosine phosphatase containing Src homology-2 domains that down-regulates cell proliferation. *Biochem. Biophys. Res. Commun.* **204**, 874–881 (1994).

110. R. S. Banh, C. Iorio, R. Marcotte, Y. Xu, D. Cojocari, A. A. Rahman, J. Pawling, W. Zhang, A. Sinha, C. M. Rose, M. Isasa, S. Zhang, R. Wu, C. Virtanen, T. Hitomi, T. Habu, S. S. Sidhu, A. Koizumi, S. E. Wilkins, T. Kislinger, S. P. Gygi, C. J. Schofield, J. W. Dennis, B. G. Wouters, B. G. Neel, PTP1B controls non-mitochondrial oxygen consumption by regulating RNF213 to promote tumour survival during hypoxia. *Nat. Cell Biol.* **18**, 803–813 (2016).

111. A. Chavez, J. Scheiman, S. Vora, B. W. Pruitt, M. Tuttle, E. P R Iyer, S. Lin, S. Kiani, C. D. Guzman, D. J. Wiegand, D. Ter-Ovanesyan, J. L. Braff, N. Davidsohn, B. E. Housden, N. Perrimon, R. Weiss, J. Aach, J. J. Collins, G. M. Church, Highly efficient Cas9-mediated transcriptional programming. *Nat. Methods* **12**, 326–328 (2015).

112. N. R. Sylvain, K. Nguyen, S. C. Bunnell, Vav1-mediated scaffolding interactions stabilize SLP-76 microclusters and contribute to antigen-dependent T cell responses. *Sci. Signal.* **4**, ra14 (2011).

113. J. S. Klein, S. Jiang, R. P. Galimidi, J. R. Keeffe, P. J. Bjorkman, Design and characterization of structured protein linkers with differing flexibilities. *Protein Eng. Des. Sel.* **27**, 325–330 (2014).

114. J. Y. Bu, A. S. Shaw, A. C. Chan, Analysis of the interaction of ZAP-70 and syk protein-tyrosine kinases with the T-cell antigen receptor by plasmon resonance. *Proc. Natl. Acad. Sci. U.S.A.* **92**, 5106–5110 (1995).

115. C. Y. Wu, K. T. Roybal, E. M. Puchner, J. Onuffer, W. A. Lim, Remote control of therapeutic T cells through a small molecule-gated chimeric receptor. *Science* **350**, aab4077 (2015).

116. J. Choi, J. Chen, S. L. Schreiber, J. Clardy, Structure of the FKBP12-rapamycin complex interacting with the binding domain of human FRAP. *Science* **273**, 239–242 (1996).

117. G. E. Wu, N. Govindji, N. Hozumi, H. Murialdo, Nucleotide sequence of a chromosomal rearranged lambda 2 immunoglobulin gene of mouse. *Nucleic Acids Res.* **10**, 3831–3843 (1982).

118. K. A. Schwarz, N. M. Daringer, T. B. Dolberg, J. N. Leonard, Rewiring human cellular input-output using modular extracellular sensors. *Nat. Chem. Biol.* **13**, 202–209 (2017).

119. T. Strittmatter, Y. Wang, A. Bertschi, L. Scheller, P. C. Freitag, P. G. Ray, P. Stuecheli, J. V. Schaefer, T. Reinberg, D. Tsakiris, A. Plückthun, H. Ye, M. Fussenegger, Programmable DARPin-based receptors for the detection of thrombotic markers. *Nat. Chem. Biol.* **18**, 1125–1134 (2022).

120. H. I. Edelstein, P. S. Donahue, J. J. Muldoon, A. K. Kang, T. B. Dolberg, L. M. Battaglia, E. R. Allchin, M. Hong, J. N. Leonard, Elucidation and refinement of synthetic receptor mechanisms. *Synth. Biol. (Oxf.)* **5**, ysaa017 (2020).

121. Y. D. Muller, D. P. Nguyen, L. M. R. Ferreira, P. Ho, C. Raffin, R. V. B. Valencia, Z. Congrave-Wilson, T. L. Roth, J. Eyquem, F. Van Gool, A. Marson, L. Perez, J. A. Wells,

J. A. Bluestone, Q. Tang, The CD28-transmembrane domain mediates chimeric antigen receptor heterodimerization with CD28. *Front. Immunol.* **12**, 639818 (2021).

122. S. Cabantous, H. B. Nguyen, J.-D. Pedelacq, F. Koraïchi, A. Chaudhary, K. Ganguly, M. A. Lockard, G. Favre, T. C. Terwilliger, G. S. Waldo, A new protein-protein interaction sensor based on tripartite split-GFP association. *Sci. Rep.* **3**, 2854 (2013).

123. Y. Kawai, M. Sato, Y. Umezawa, Single color fluorescent indicators of protein phosphorylation for multicolor imaging of intracellular signal flow dynamics. *Anal. Chem.* **76**, 6144–6149 (2004).

124. L. Oldach, J. Zhang, Genetically encoded fluorescent biosensors for live-cell visualization of protein phosphorylation. *Chem. Biol.* **21**, 186–197 (2014).

125. E. Kardash, J. Bandemer, E. Raz, Imaging protein activity in live embryos using fluorescence resonance energy transfer biosensors. *Nat. Protoc.* **6**, 1835–1846 (2011).

126. S. Regot, J. J. Hughey, B. T. Bajar, S. Carrasco, M. W. Covert, High-sensitivity measurements of multiple kinase activities in live single cells. *Cell* **157**, 1724–1734 (2014).

127. C. Linghu, S. L. Johnson, P. A. Valdes, O. A. Shemesh, W. M. Park, D. Park, K. D. Piatkevich, A. T. Wassie, Y. Liu, B. An, S. A. Barnes, O. T. Celiker, C.-C. Yao, C. J. Yu, R. Wang, K. P. Adamala, M. F. Bear, A. E. Keating, E. S. Boyden, Spatial multiplexing of fluorescent reporters for imaging signaling network dynamics. *Cell* **183**, 1682–1698.e24 (2020).

128. K. Lasker, S. Boeynaems, V. Lam, D. Scholl, E. Stainton, A. Briner, M. Jacquemyn, D. Daelemans, A. Deniz, E. Villa, A. S. Holehouse, A. D. Gitler, L. Shapiro, The material properties of a bacterial-derived biomolecular condensate tune biological function in natural and synthetic systems. *Nat. Commun.* **13**, 5643 (2022).

129. H. Shankaran, D. L. Ippolito, W. B. Chrisler, H. Resat, N. Bollinger, L. K. Opresko, H. S. Wiley, Rapid and sustained nuclear-cytoplasmic ERK oscillations induced by epidermal growth factor. *Mol. Syst. Biol.* **5**, 332 (2009).

130. P. Kafri, S. E. Hasenson, I. Kanter, J. Sheinberger, N. Kinor, S. Yunger, Y. Shav-Tal, Quantifying β-catenin subcellular dynamics and cyclin D1 mRNA transcription during Wnt signaling in single living cells. *eLife* **5**, e16748 (2016).

131. W. Zhang, Y. Jiang, Q. Wang, X. Ma, Z. Xiao, W. Zuo, X. Fang, Y.-G. Chen, Single-molecule imaging reveals transforming growth factor-beta-induced type II receptor dimerization. *Proc. Natl. Acad. Sci. U.S.A.* **106**, 15679–15683 (2009).

132. H. Clevers, R. Nusse, Wnt/β-catenin signaling and disease. *Cell* **149**, 1192–1205 (2012).

133. R. Wang, M. G. Brattain, The maximal size of protein to diffuse through the nuclear pore is larger than 60kDa. *FEBS Lett.* **581**, 3164–3170 (2007).

134. J. Abdolalizadeh, M. Nouri, J. M. Zolbanin, A. Barzegari, B. Baradaran, J. Barar, G. Coukos, Y. Omidi, Targeting cytokines: Production and characterization of anti-TNF-α scFvs by phage display technology. *Curr. Pharm. Des.* **19**, 2839–2847 (2013).

135. P. Tang, Hung M-C, J. Klostergaard, Human pro-tumor necrosis factor is a homotrimer. *Biochemistry* **35**, 8216–8225 (1996).

136. K. W. Moore, R. de Waal Malefyt, R. L. Coffman, A. O'Garra, Interleukin-10 and the interleukin-10 receptor. *Annu. Rev. Immunol.* **19**, 683–765 (2001).

137. A. Joss, M. Akdis, A. Faith, K. Blaser, C. A. Akdis, IL-10 directly acts on T cells by specifically altering the CD28 co-stimulation pathway. *Eur. J. Immunol.* **30**, 1683–1690 (2000).

138. C. A. Akdis, K. Blaser, Mechanisms of interleukin-10-mediated immune suppression. *Immunology* **103**, 131–136 (2001).

139. D. M. Mosser, X. Zhang, Interleukin-10: New perspectives on an old cytokine. *Immunol. Rev.* **226**, 205–218 (2008).

140. A. Cardoso, A. Gil Castro, A. C. Martins, G. M. Carriche, V. Murigneux, I. Castro, A. Cumano, P. Vieira, M. Saraiva, The dynamics of interleukin-10-afforded protection during dextran sulfate sodium-induced colitis. *Front. Immunol.* **9**, 400 (2018).

141. L. Steidler, W. Hans, L. Schotte, S. Neirynck, F. Obermeier, W. Falk, W. Fiers, E. Remaut, Treatment of murine colitis by *Lactococcus lactis* secreting interleukin-10. *Science* **289**, 1352–1355 (2000).

142. W. Ouyang, A. O'Garra, IL-10 family cytokines IL-10 and IL-22: From basic science to clinical translation. *Immunity* **50**, 871–891 (2019).

143. S. Schreiber, R. N. Fedorak, O. H. Nielsen, G. Wild, C. N. Williams, S. Nikolaus, M. Jacyna, B. A. Lashner, A. Gangl, P. Rutgeerts, K. Isaacs, S. J. H. van Deventer, J. C. Koningsberger, M. Cohard, A. LeBeaut, S. B. Hanauer, Crohn's Disease IL-10 Cooperative Study Group, Safety and efficacy of recombinant human interleukin 10 in chronic active Crohn's disease. *Gastroenterology* **119**, 1461–1472 (2000).

144. J. F. Colombel, P. Rutgeerts, H. Malchow, M. Jacyna, O. H. Nielsen, J. Rask-Madsen, S. Van Deventer, A. Ferguson, P. Desreumaux, A. Forbes, K. Geboes, L. Melani, M. Cohard, Interleukin 10 (Tenovil) in the prevention of postoperative recurrence of Crohn's disease. *Gut* **49**, 42–46 (2001).

145. M. Saraiva, P. Vieira, A. O'Garra, Biology and therapeutic potential of interleukin-10. *J. Exp. Med.* **217**, e20190418 (2020).

146. N. Basgoz, I. Qadri, D. Navarro, A. Sears, E. Lennette, J. Youngblom, L. Pereira, The amino terminus of human cytomegalovirus glycoprotein B contains epitopes that vary among strains. *J. Gen. Virol.* **73**, 983–988 (1992).

147. F. Facciotti, P. Larghi, R. Bosotti, C. Vasco, N. Gagliani, C. Cordiglieri, S. Mazzara, V. Ranzani, E. Rottoli, S. Curti, A. Penatti, B. Karnani, Y. Kobayashi, M. Crosti, M. Bombaci, J. P. van Hamburg, G. Rossetti, R. Gualtierotti, M. Gerosa, S. Gatti, S. Torretta, L. Pignataro, S. W. Tas, S. Abrignani, M. Pagani, F. Grassi, P. L. Meroni, R. A. Flavell, J. Geginat, Evidence for a pathogenic role of extrafollicular, IL-10-producing $CCR6^{+}$B helper T cells in systemic lupus erythematosus. *Proc. Natl. Acad. Sci. U.S.A.* **117**, 7305–7316 (2020).

148. D. G. Brooks, M. J. Trifilo, K. H. Edelmann, L. Teyton, D. B. McGavern, M. B. A. Oldstone, Interleukin-10 determines viral clearance or persistence in vivo. *Nat. Med.* **12**, 1301–1309 (2006).

149. R. Zhu, J. M. Del Rio-Salgado, J. Garcia-Ojalvo, M. B. Elowitz, Synthetic multistability in mammalian cells. *Science* **375**, eabg9765 (2022).

150. S. K. Dhanda, S. Mahajan, S. Paul, Z. Yan, H. Kim, M. C. Jespersen, V. Jurtz, M. Andreatta, J. A. Greenbaum, P. Marcatili, A. Sette, M. Nielsen, B. Peters, IEDB-AR: Immune epitope database-analysis resource in 2019. *Nucleic Acids Res.* **47** (W1), W502–W506 (2019).

151. K. T. Roybal, L. J. Rupp, L. Morsut, W. J. Walker, K. A. McNally, J. S. Park, W. A. Lim, Precision tumor recognition by T cells with combinatorial antigen-sensing circuits. *Cell* **164**, 770–779 (2016).

152. I. Zhu, R. Liu, J. M. Garcia, A. Hyrenius-Wittsten, D. I. Piraner, J. Alavi, D. V. Israni, B. Liu, A. S. Khalil, K. T. Roybal, Modular design of synthetic receptors for programmed gene regulation in cell therapies. *Cell* **185**, 1431–1443.e16 (2022).

153. T. Fink, R. Jerala, Designed protease-based signaling networks. *Curr. Opin. Chem. Biol.* **68**, 102146 (2022).

154. C. H. June, M. Sadelain, Chimeric antigen receptor therapy. *N. Engl. J. Med.* **379**, 64–73 (2018).

155. S. Paul, M. F. Konig, D. M. Pardoll, C. Bettegowda, N. Papadopoulos, K. M. Wright, S. B. Gabelli, M. Ho, A. van Elsas, S. Zhou, Cancer therapy with antibodies. *Nat. Rev. Cancer* **24**, 399–426 (2024).

156. G. Chamberlain, J. Fox, B. Ashton, J. Middleton, Concise review: mesenchymal stem cells: their phenotype, differentiation capacity, immunological features, and potential for homing. *Stem Cells* **25**, 2739–2749 (2007).

157. K. C. Dunn, A. E. Aotaki-Keen, F. R. Putkey, L. M. Hjelmeland, ARPE-19, a human retinal pigment epithelial cell line with differentiated properties. *Exp. Eye Res.* **62**, 155–169 (1996).